Lawrence Berkeley National Laboratory

Recent Work

Title

Photodissociation of Ketene: CH{sub 2}CO {arrow} CH{sub 2}(a{sup 1}A{sub 1}) + CO(v=1) Rates and Dynamics

Permalink

https://escholarship.org/uc/item/0rq4v6sx

Author

Wade, Elisabeth A.

Publication Date

1996-12-04

eScholarship.org Powered by the California Digital Library
University of California

LBNL-39767
UC-401

ERNEST ORLANDO LAWRENCE
BERKELEY NATIONAL LABORATORY

Photodissociation of Ketene: $CH_2CO \rightarrow CH_2(\tilde{a}\ ^1A_1) + CO(v=1)$ Rates and Dynamics

Elisabeth Ayn Wade
Chemical Sciences Division

December 1996
Ph.D. Thesis

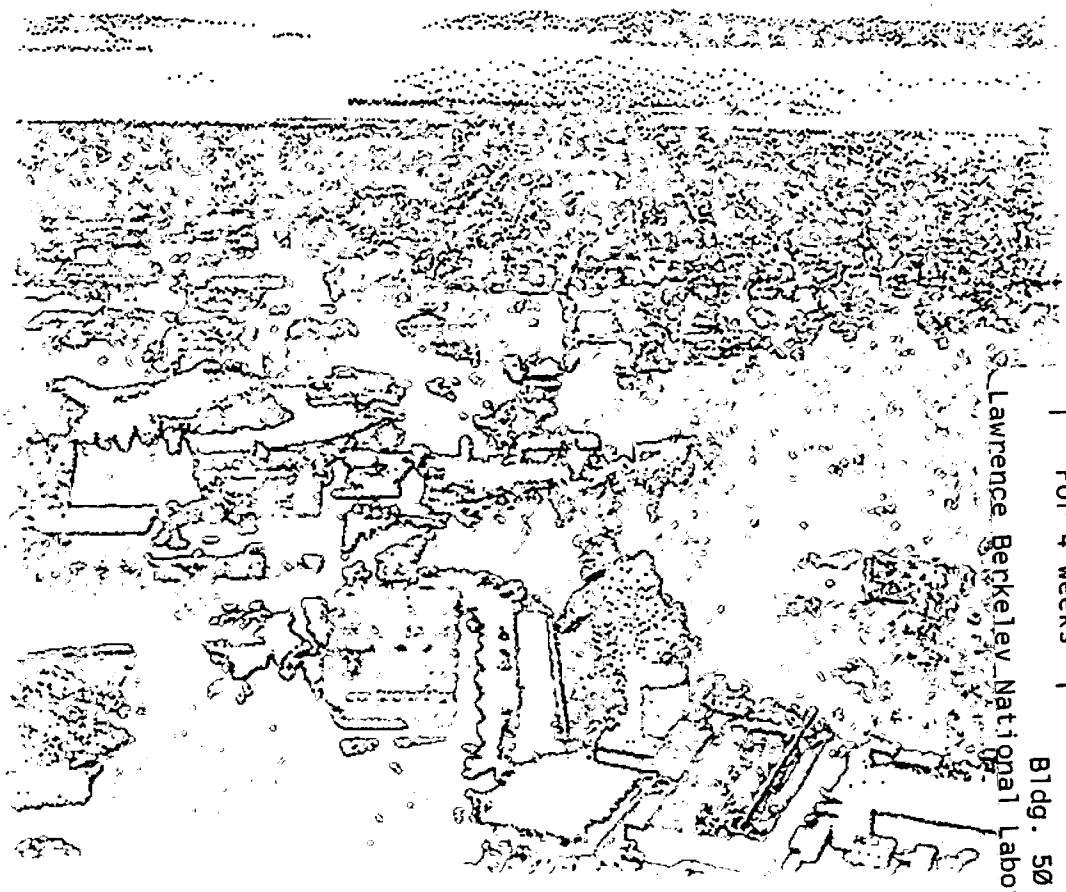

LOAN COPY
Circulates
For 4 weeks

Lawrence Berkeley National Laboratory
Bldg. 50 Library
Copy 2

LBNL-39767

DISCLAIMER

This document was prepared as an account of work sponsored by the United States Government. While this document is believed to contain correct information, neither the United States Government nor any agency thereof, nor the Regents of the University of California, nor any of their employees, makes any warranty, express or implied, or assumes any legal responsibility for the accuracy, completeness, or usefulness of any information, apparatus, product, or process disclosed, or represents that its use would not infringe privately owned rights. Reference herein to any specific commercial product, process, or service by its trade name, trademark, manufacturer, or otherwise, does not necessarily constitute or imply its endorsement, recommendation, or favoring by the United States Government or any agency thereof, or the Regents of the University of California. The views and opinions of authors expressed herein do not necessarily state or reflect those of the United States Government or any agency thereof or the Regents of the University of California.

LBNL-39767
UC-401

Photodissociation of Ketene: $CH_2CO \rightarrow CH_2(\tilde{a}\,^1A_1) + CO(v=1)$ Rates and Dynamics

Elisabeth Ayn Wade

Department of Chemistry
University of California, Berkeley

and

Chemical Sciences Division
Ernest Orlando Lawrence Berkeley National Laboratory
University of California
Berkeley, California 94720

December 1996

This work was supported by the Director, Office of Energy Research, Office of Basic Energy Sciences, Chemical Sciences Division, of the U.S. Department of Energy under Contract No. DE-AC03-76SF00098.

Photodissociation of Ketene:
$CH_2CO \rightarrow CH_2(\tilde{a}\ ^1A_1) + CO(v=1)$
Rates and Dynamics

by

Elisabeth Ayn Wade

B.S. (Harvey Mudd College) 1992

A dissertation submitted in partial satisfaction of the

requirements for the degree of

Doctor of Philosophy

in

Chemistry

in the

GRADUATE DIVISION

of the

UNIVERSITY of CALIFORNIA, BERKELEY

Committee in charge:

Professor C. Bradley Moore, Chair
Professor Daniel Neumark
Professor Ronald Dibble

1996

Abstract

Photodissociation of Ketene: $CH_2CO \rightarrow CH_2(\tilde{a}\ ^1A_1) + CO(v=1)$
Rates and Dynamics

by

Elisabeth Ayn Wade

Doctor of Philosophy in Chemistry

University of California, Berkeley

Professor C. Bradley Moore, Chair

The rotational energy release in the dissociation of ketene (CH_2CO) along its singlet potential energy surface is observed and compared with several statistical and dynamical theories. Rotational distributions for the product, $CO(\tilde{X}\ ^1\Sigma^+)(v=1)$, are measured from the threshold for production of $CH_2(\tilde{a}\ ^1A_1)$ (0,0,0) + $CO(\tilde{X}\ ^1\Sigma^+)(v=1)$ to 1720 cm^{-1} above. Near threshold ($E \leq$ 200 cm^{-1} over threshold), phase space theory (PST) matches the observed distributions. At 357 and 490 cm^{-1}, PST constrained by the measured state distributions of the methylene fragment, provides a good fit to these CO(v=1) rotational distributions. For $E > 490$ cm^{-1}, the constrained PST matches the average rotational energy observed but predicts distributions which are broader than observed. This contrasts to the rotational distributions of the $^1CH_2$ fragment which become shifted to lower rotational states than PST as energy increases from 200 cm^{-1} above threshold. Dynamical models, the impulsive model and Franck-Condon mapping, do not account for the product rotational state distributions. The CO(v=1) rotational distributions for $E >$ 200 cm^{-1} contain no measurable product from triplet channel fragmentation.

Therefore, they can be compared with the previously determined CO(v=0) rotational distributions in order to partition the CO(v=0) yield between singlet and triplet channels and recalculate the singlet yield. This new yield is found to be at the upper limits of the range previously reported.

Rate constants and quantum yields have been determined for the photodissociation of ketene to produce $CH_2(\tilde{a}\ ^1A_1)$ (0,0,0) + $CO(\tilde{X}\ ^1\Sigma^+)$(v=1). At 57, 110, 200, 357, and 490 cm^{-1} above this product threshold, vibrational branching ratios for the singlet products were measured and compared to phase space theory (PST), separate statistical ensembles (SSE), and variational RRKM (var. RRKM). Above 100 cm^{-1} above that threshold, the experimental values are consistent with SSE and var. RRKM. $CO(v=1,J_{CO})$ photofragment excitation (PHOFEX) spectra were observed up to 357 cm^{-1} over the threshold for production of CO(v=1) and used to calculate the total yield of the state probed. Up to 350 cm^{-1} over threshold, this yield is statistical, consistent with the observed $^1CH_2$ rotational distributions. The singlet channel vibrational branching ratios and PHOFEX spectra are combined with the previously determined singlet yield and total rate constant to determine the singlet rate constant for CO(v=1) production as a function of energy. Rate constants are given accurately by PST from threshold up to 35±5 cm^{-1} above. From 35 cm^{-1}, the transition state begins to tighten as energy increases; the rate increases more slowly than the PST rate, as predicted by var. RRKM. For energies up to 2500 cm^{-1}, it appears that both the outer, PST transition state and an inner transition state at a C-C distance of 2.2-3.1 Å affect the rate. Above 2500 cm^{-1}, the measured rate is consistent with var. RRKM with a single transition state at 2.2-3.1 Å. From

the measured rate constants, an experimental vibrational density of states is calculated to be 1.82±0.12 times the Whitten-Rabinovich density of states. This indicates that the degeneracy of the coupled triplet channels, g_t, is 1.6±0.1. The vibrational branching ratios and product yields for the vibrationally excited triplet products were also estimated, and found to be nearly constant over this energy region. These values were about 17% of the predicted value, assuming that the triplet fragmentation dynamics are vibrationally adiabatic.

Table of Contents

Chapter 1. Introduction 1
References 14
Chapter 2. Experimental 17
References 27
Chapter 3. The Dynamics of Rotational Energy Release for Dissociation of Singlet Ketene and the Singlet/Triplet Branching Ratio . . . 28
I. Introduction 28
II. Results 31
III. Modeling Rotational Distributions 41
IV. Singlet Yield 58
V. References 67
Chapter 4. The Tightening Transition State 69
I. Introduction 69
II. Results 73
IIA. Vibrational Branching Ratios 73
IIB. PHOFEX Spectra 77
III. Discussion 85
IIIA. Vibrational Branching Ratios 85
IIIB. PHOFEX Spectra 87
IIIC. Singlet Rate Constants 89
IIID. Triplet Vibrational Brancing Ratio and Rate Constant 108
IV. Conclusions 109
V. References 111
Appendix A. Rotational Distributions 114
Appendix B. Rate Constant to 300 cm^{-1} 118
Appendix C. Constrained PST Program 123

List of Tables

Table I. Comparison of Experiment and Constrained PST 51

Table II. Singlet Yield 61

Table III. Vibrational Branching Ratios for Singlet Product Channel. . 74

Table IV. Vibrational Branching Ratios for Triplet Product Channel . 75

Table V. Test for Dependence of PHOFEX on Triplet Quantum Yield and Dependence of Optical Cross Section on hν 81

Table VI. Rate Constants 100

List of Figures

Figure 1. Schematic diagram of a PES with adiabatic channels. . . . 12
Figure 2. The low-lying potential energy surfaces of ketene 13
Figure 3. Schematic of experimental apparatus 25
Figure 4. Schematic of Mg heat pipe oven 26
Figure 5. Rotational Distributions 32
Figure 6. Testing Constrained PST 52
Figure 7. Comparison of Experiment, PST, and Constrained PST . . 53
Figure 8. Boltzmann plots at 1460 cm^{-1} 56
Figure 9. Comparison of Experiment and Franck-Condon mapping . . 57
Figure 10. CO(v=0) and CO(v=1) rotational distributions at 425 cm^{-1} . 62
Figure 11. CO(v=0) and CO(v=1) rotational distributions at 1107 cm^{-1} . 63
Figure 12. CO(v=0) and CO(v=1) rotational distributions at 1435 cm^{-1} . 64
Figure 13. Triplet rate constant 65
Figure 14. Singlet Yield 66
Figure 15. Singlet Vibrational Branching Ratios 76
Figure 16. PHOFEX Spectra 82
Figure 17. Singlet Rate Constants 102
Figure 18. Singlet Rate Constants at Low Energy 104
Figure 19. Density of States 106
Figure 20. Number of Open Channels (W) 107

Acknowledgements

As always, any complex endeavor (and this endeavor was sometimes much more than complex) has more than one contributor. First, I must thank my husband, Doug, without whose support, financial and emotional, I never would have succeeded. He especially deserves thanks for helping me with my programming, as I am not a cheerful person after several hours of unsuccessful debugging, and for putting up with me when it seemed to me that I would never finish.

My advisor, Brad Moore, was invaluable as a source of advice about doing science and being a scientist. His guidance and support were always greatly appreciated. I was very fortunate in my graduate career in that my research got off to a rapid start; much of the credit for that goes to Sang Kyu Kim, who came up with the idea that led to this project, and to Horst Clauberg and Kenny Ni, two postdocs who were always available and willing to help. Michael Ashikhmin and Axel Mellinger were both helpful in the later stages of this project. Jason Crane, Harry Beal, Melonie Hall, Stacie Cowan, and Catharine Carlin offered me occassional assistance and less-occassional, but much appreciated, research breaks.. I would also like to thank the rest of the Moore Group, especially Rich Blair, Peter Radkowski, Ilia Kalinovski, Bruce McNamara, Ashfaq Bengali, Rich Schultz, Jeff Petty, and Ramon Alvarez, for their fellowship and support.

Finally, I would like to thank my parents, Harold and Charlotte Davis, and my sister, Cathlin, for listening during the last four years, whether or not they understood what I was saying, and my grandmother, Mary Kathleen Davis, who was the first chemist in the family, and whose more traditional lab led my father to remark: "This doesn't look like Chemistry. There's no glassware, just big orange boxes!"

Chapter 1. Introduction

Unimolecular reactions are one of the three classes of elementary chemical reactions. As such, they are of great theoretical and practical significance. Understanding the dynamics of unimolecular decomposition has been a long-standing goal of physical chemistry. With the development of molecular beams and lasers, on the experimental side, and *ab initio* methods, on the theoretical side, it has become possible to distinguish experimentally among theories describing unimolecular decomposition and to use these theories predictively.[1-5]

The decomposition of a chemically bound molecule in the absence of collisions is controlled by its potential energy surface (PES). The equilibrium geometries of the reactant and products and the region between reactants and products are important.[1-5] It is convenient to define a reaction coordinate, usually as the distance along the minimum energy pathway between the products and the reactants, and to define a transition state perpendicular to the reaction coordinate at some point along that pathway. Any theory based on this definition is grouped under transition state theory (TST).[1] In most theories, this perpendicular surface becomes the dividing line between reactants and products; the rate of the reaction is then defined by the rate of crossing this dividing line with, perhaps, a correction for trajectories which recross.[3]

When there is a barrier along the reaction coordinate, the repulsive force along the reaction coordinate on the product side of the barrier pushes products apart ensuring that reactant molecules passing over the barrier continue on to products. The transition state is therefore defined at the top of the barrier. In the limit that energy flows randomly among the vibrational

degrees of freedom of the reactant and that the energy flow is rapid compared to the rate at which the molecule passes through the transition state, the rate is calculated statistically. The statistical rate constant for a reactant molecule with total energy E and total angular momentum J is given by

$$k(E,J) = \frac{W(E,J)}{h\rho(E,J)} \qquad (1\text{-}1)$$

where k(E,J) is the dissociation rate, W(E,J) is the sum of states or open reaction channels at the transition state, h is Planck's constant, and ρ(E,J) is the density of states of the reactant. Rice-Ramsperger-Kassel-Marcus (RRKM) theory is the version of statistical TST that has been most successful in modeling reactions with a barrier.[1-4]

In many systems, including $NO_2 \rightarrow NO + O$, $NCNO \rightarrow NC + NO$, $HOOH \rightarrow 2OH$, and ketene ($CH_2CO \rightarrow {}^1CH_2 + CO$), the system of interest in this work, there is no barrier to fragment recombination. In the absence of a barrier along the reaction coordinate, assigning a transition state becomes more complex. Several models have been proposed in this case. These include phase space theory (PST),[6] statistical adiabatic channel model (SACM),[7,8] and variational RRKM (var. RRKM).[9-11] Separate statistical ensembles (SSE),[12] is another theory commonly used with PST to predict product state distributions. SSE differs from these theories in that it is not a form of TST.

In a barrierless reaction, the energy maximum between reactants and products occurs at infinite separation of products. This is sometimes called a "loose" transition state. W(E,J) at infinite separation is simply the number of energetically accessible rovibrational product states. When this limit holds, PST can be used to calculate the rate. In PST, no knowledge of the PES,

other than the product state energies and reactant density of states, which are typically available from spectroscopic parameters, is required. As a result, there are no adjustable parameters in PST calculations.

Experimental rate constants, measured directly for NO_2[13] and NCNO,[14,15] and indirectly for NO_2[16] and CH_2CO[17] provide strong evidence for the validity of PST in the first few tens of cm^{-1} above the dissociation threshold. However, in all three systems, as the energy increases, the measured rates are found to increase less rapidly than predicted by PST. Dissociation rates have also been measured for HOOH, but these measured rates are found to vary non-monotonically with excitation energy, unlike the other three systems, and the decays cannot be well fit by a single exponential.[18,19] It is not clear if this non-monotonic behavior is best explained by statistical state-to-state fluctuations[20] or by nonstatistical behavior.[19]

Since PST assumes that every energetically accessible channel is equally likely to be formed, PST can be used to calculate product state distributions, as well as rates. In this case, the probability of forming a given product state, J_p, is

$$P(E,J,J_p) = \frac{W(E,J,J_p)}{\sum_{J'_p} W(E,J,J'_p)} \qquad (1\text{-}2)$$

Product state distributions have been measured for NCNO,[12,21] CH_2CO,[17,22–27] NO_2,[16,28-32] and HOOH.[19,33-36] Within 200 cm^{-1} of threshold, the product rotational state distributions for NCNO, CH_2CO, and NO_2 are accurately predicted by PST. HOOH is dissociated using overtone spectroscopy and so the dissociation energy cannot be chosen over as wide a

region as in the other cases.[36] For all these systems, product state distributions, however, show more diverse behaviors than do the rate constants.

For NCNO, the product rotational distributions follow PST, as long as there is not enough energy available for vibrational excitation of products.[12] The vibrational branching ratios are larger than predicted by PST, but when SSE is used to predict the vibrational branching ratios, the rotations are found to be well described by PST, even at energies up to 2500 cm^{-1} over the dissociation threshold.[12] Even the correlated product state distributions of NCNO are described well by PST.[21]

The observed behavior for CH_2CO is somewhat more complex. The rotational state distributions of singlet methylene ($^1CH_2$) produced by photodissociation of CH_2CO are described by PST for $E \leq 200$ cm^{-1} over threshold for photodissociation.[17] At higher energies, PST predicts rotational distributions that are significantly hotter than the experimental distributions.[25] Because CH_2CO has two channels to dissociation,[3] one producing $^1CH_2$ and one producing $^3CH_2$, the CO rotational distributions for the singlet channel are complicated by the presence of CO associated with $^3CH_2$. Near threshold, however, where the distributions are clearly bimodal, the CO produced via the singlet channel is well described by PST.[17] At higher energies, the CO rotational distributions for the singlet and triplet product channels are not clearly resolved. As with NCNO, the vibrational yields for $^1CH_2$ and for CO are higher than predicted by PST.[17,26]

For NO_2, the averaged fits to the rotational distributions are in good

agreement with the predictions of PST up to 3000 cm^{-1} over the dissociation threshold.[30,31] However, when the rotational distributions are considered in more detail, fluctuations about the PST predictions are observed. These fluctuations are interpreted as evidence of overlapping resonances of the wavefunction at the transition state. These overlapping resonances are observable because NO_2 is a triatomic, so that the internal state distributions of the NO need not be averaged over the rovibrational state distributions of another fragment.[32] The vibrational populations of NO were found to increase non-monotonically, which provides further evidence of these fluctuations.[31]

For HOOH, the experimental results are more difficult to interpret than for the three systems above. HOOH is photodissociated using vibrational overtones rather than the strong electronic transitions used to photolyze the other species, and so have been performed using bulk samples. As a result, the initial state of the reactant cannot be easily specified. The product rotational-state distributions depend strongly on the vibrational state which is excited. Photolysis at $6\nu_{OH}$ yields an OH rovibrational distribution in good agreement with PST, while photolysis at $5\nu_{OH}$ or a combination band near $6\nu_{OH}$ yields a distribution colder than PST.[36] In other words, the PST distribution peaks at higher rotational energy than the experimental distributions.

PST's overestimation of the rate constants for NCNO, CH_2CO, and NO_2 at high energies suggests that, for these systems, the transition state is "tighter" than PST would predict. For CH_2CO, for example, *ab initio* calculations suggest that the transition state lies at a C-C bond distance of

about 3.0 Å,[37,39] except for within the first 100 cm^{-1} above threshold. At that distance, the C-C bond is already partially formed, and the anisotropy for rotating the CO fragment in ketene is calculated to be ~1000 cm^{-1}.[37,39] Two models, SACM and var. RRKM, are based on the idea of the transition state moving in along the reaction coordinate as the total energy increases. While the transistion state at threshold occurs at infinite separation of products, as energy increases, the distance between fragments at the transition state decreases. SACM and var. RRKM differ in the way that they locate the transition state, but give identical results for k(E,J) if it is assumed that there are no curve crossings.

Var. RRKM theory defines the transition state by the "minimum entropy" criterion, at the position along the reaction coordinate, $R^{\ddagger}(E)$, where $W(R^{\ddagger}(E))$ is minimum. To calculate k(E,J), then $W(E,J)=W(R^{\ddagger}(E))$. This causes the transition state to move in along the reaction coordinate as energy increases. Moving in along the reaction coordinate, the separated fragments go from being independent free rotors, to hindered rotors, to bending or torsional vibrations, and the energy spacing between states increases. Thus, $R^{\ddagger}(E)$ decreases with increasing energy. This is shown schematically in Figure 1. As a result, as energy increases, the transition state moves in along the reaction coordinate and the rate constant is decreased relative to PST.[9] Determining $W(R^{\ddagger})$ requires a model for the PES. In most cases, high-quality *ab initio* potentials are not available and model potentials are used. A var. RRKM calculation based on a model potential for CH_2CO has been compared with the experimental rate constants and was found to reproduce them quite well.[10] However, a later calculation based on an *ab initio* potential overestimated the rate constant.[37] A recent var. RRKM calculation based on

a complete *ab inito* anharmonic vibrational analysis of ketene[38] predicts the rate with greater accuracy.[39]

RRKM is not traditionally used to calculate product state distributions. However, in 1985, Marcus suggested that for loose, PST transition states, each product vibrational state is well-defined before the system reaches the transition state.[9,10] Dissociation therefore occurs on several different vibrationally adiabatic potential energy surfaces, each of which has its own variationally determined transition state. The vibrational distribution is then given by the ratio of the rate for each vibrationally adiabatic channel. Marcus's method has been used to calculate var. RRKM vibrational distributions for ketene.[10] These vibrational distributions have been found to agree extremely well with experimental vibrational distributions for $^1CH_2$ at several energies[26] and for CO at a single energy, 2500 cm^{-1} above the singlet channel threshold.[17]

SACM further extends the adiabatic assumptions of var. RRKM. It is based on a correlation diagram connecting each reactant quantum state to a product channel.[7,8] While energy flow between these channels is rapid at the reactant, at some point along the reactant coordinate, the dynamics become adiabatic. The model assumes that the channels become adiabatic before the energy maximum for all energetically accessible channels. Like var. RRKM, SACM requires knowledge of the shape of the PES.

Functionally, SACM is similar to PST, but a channel is only considered open if its energy maximum lies below the total available energy. Fewer channels are accessible, so the SACM rate rises more slowly than PST. However, SACM also raises the appearance threshold for each rovibrational product channel if the dynamics follow each curve strictly from its maximum

to separated fragments. For the dissociation of CH_2CO, each rovibrational state is observed precisely at its thermochemical threshold, while the dissociation rate can only be matched by raising product appearance thresholds above the measured thresholds.[23] The fundamental physical idea that each product state is adiabatically correlated to a different transition state is clearly incorrect since the same barriers cannot fit both the rate and the observed appearance thresholds. However, simply as a method of calculating rates, SACM has been used successfully to predict dissociation rates for NO_2.[40]

Another theory that is often applied to reactions that have no barrier is the Separate Statistical Ensembles (SSE) model. SSE was developed by Wittig and co-workers to explain PST-like rotational distributions and higher-than-PST vibrational excitation in NCNO.[12] Unlike the other theories discussed here, SSE is not a rate theory, and is not based on TST. In SSE, the vibrational population, P(v), is assumed to be proportional to the density of states of an ensemble of D oscillators, $\rho_D(E,v)$. $\rho_D(E,v)$ is proportional to $(E-E_v)^{(D/2-1)}$, where $E-E_v$ is the available energy in excess of that needed to form the product in vibrational state v. TST is based upon W(E,J), the number of quantum states at the transition state, rather than the density of quantum states.[3]

SSE predicts that P(v) is a smoothly varying function of energy, and therefore cannot predict the near-threshold steps in the photofragment excitation (PHOFEX) spectra for vibrationally excited $^1CH_2$.[24,26] However, SSE does give predictions for P(v) that are in excellent agreement with the experimental yields of vibrationally excited products for CH_2CO[17,26] and

NCNO.[12] For CH_2CO, SSE also agrees well with the vibrational yield calculated by var. RRKM,[17,26] although SSE contains no adjustable parameters or information about the PES.

This work focuses on the photodissociation of CH_2CO along its singlet surface to produce $^1CH_2$ and vibrationally excited CO (CO(v=1)). The low lying electronic states of ketene are shown in Figure 2. Ketene is excited in the UV using a transition whose oscillator strength is derived from electronic excitation to the first excited singlet state, S_1. The ketene molecule then undergoes internal conversion to the ground state, S_0, or intersystem crossing to the triplet surface, T_1, and subsequently dissociates along either S_0 or T_1 into methylene and $CO(\tilde{X}^1\Sigma^+)$ fragments.[3] Ketene dissociates along S_0 (the singlet channel) into $CH_2(\tilde{a}^1A_1)$ ($^1CH_2$) and CO fragments with a threshold energy of 30,116 cm^{-1}.[23] Dissociation along the singlet channel provides a good test case for unimolecular reaction without a barrier and is the dissociation channel described above. Dissociation along T_1 (the triplet channel) into $CH_2(\tilde{X}^3B_1)$ ($^3CH_2$) and CO occurs on a surface with a small barrier about 1330 cm^{-1} above the triplet products and 1820 cm^{-1} below the singlet products, Figure 2.[41,42]

Kim et al. have determined the rotational distributions for CO produced from the dissociation of ketene, but found that the CO observed was associated with ketene dissociating on both the singlet and the triplet surfaces.[17] At energies close to the singlet threshold, the distributions were bimodal, and the "singlet" CO could be easily distinguished from the "triplet" CO. At higher energies, the two distributions overlapped so completely that

they were unresolvable.[17]

A major goal of the work of Kim et al. was to calculate the singlet/triplet branching ratio, since the only experimental rate constants measured above the singlet threshold were total rate constants, measured by Zewail and co-workers.[43] At energies less than 200 cm^{-1} above the singlet threshold, it was clear that the part of the CO distribution associated with the singlet dissociation surface was well-described by PST. Additionally, for the highest energy, 2500 cm^{-1} above the singlet channel threshold, a rotational distribution was measured for the vibrationally excited CO fragment. This energy is 357 cm^{-1} over the threshold for production of CO(v=1) from the singlet channel, since the vibrational frequency of CO is 2153.2 cm^{-1}. At a similar energy over its production threshold, the fraction of CO(v=0) produced along the singlet channel (the singlet quantum yield) was 0.60, while in the CO(v=1) distribution, no product that could be ascribed to the triplet channel was observed.[17] This CO(v=1) distribution was also well-described by PST. It was assumed, then, that the singlet distributions would follow PST; the triplet distributions were approximated by a single Gaussian.[17,42]

When Garcia-Moreno et al. measured the rotational distributions for the $^1CH_2$ fragment, there was, of course, no contribution from the triplet, since the triplet channel produced another electronic state of methylene, $^3CH_2$.[25,26] At energies below 200 cm^{-1}, the experimental distributions and the PST predictions were identical. As the energy increased, the experimental distributions deviated increasingly strongly from PST.[25] This same rotational behavior was observed when rotational distributions for

vibrationally excited species of $^1CH_2$ were determined.[26] It is highly unlikely that the CO distributions could be completely described by PST for all energies above threshold, when the $^1CH_2$ distributions are not. It has also been suggested that, since the rotational constant for CO is much smaller than that for $^1CH_2$, that the CO rotations may be statistical to higher energies than those for $^1CH_2$.[44] However, this statistical behavior would not be identical to PST, since pure PST assumes that BOTH fragment rotations are statistical. Instead, the CO rotations would be expected to follow a constrained form of PST, in which the internal energy of the CO fragment is allowed to vary statistically while the internal energy of the $^1CH_2$ fragment is constrained to the experimental distribution for the appropriate photolysis energy.

In this work, the rotational state distributions of CO(v=1) have been determined for photolysis energies ranging from 0 to 1720 cm^{-1} above the singlet dissociation threshold associated with CO(v=1). Since the singlet yield is much greater for CO(v=1) than for CO(v=0), the "triplet" CO should not complicate these rotational distributions.[17] These experimental CO(v=1) distributions were used to examine various statistical model predictions of rotational distributions for the singlet channel, and to reanalyze the singlet/triplet branching ratio. Additionally, for photolysis energies up to 500 cm^{-1} above that threshold, vibrational branching ratios and CO(v=1) PHOFEX spectra were determined. In conjunction with the total rate constant for ketene dissociation,[43] these two sets of measurements were used to calculate an experimental rate constant for the photodissociation near threshold.

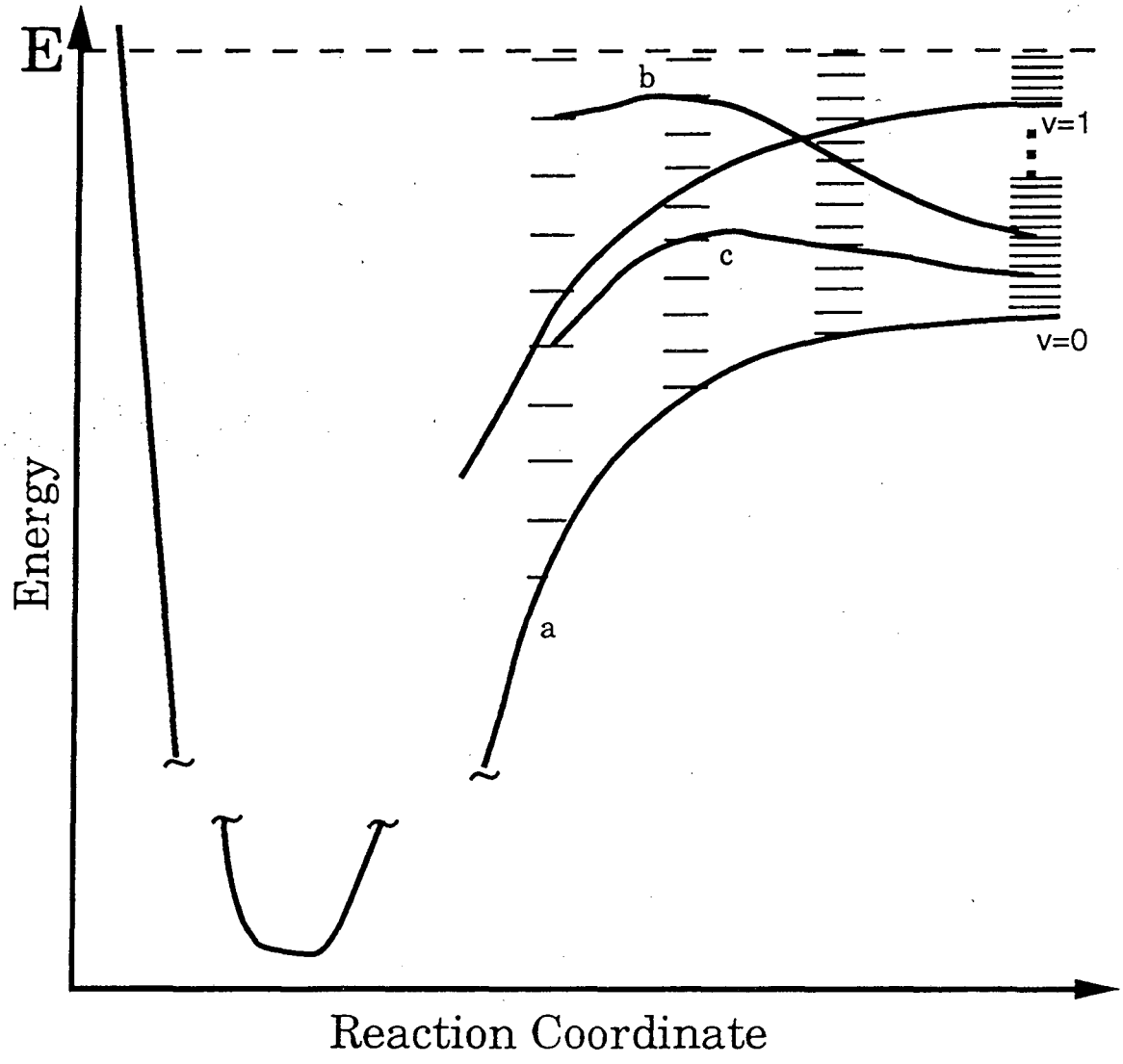

Figure 1. Schematic diagram of a PES with vibrational levels and adiabatic channels shown. The product vibrations become adiabatic at point a, so effective potentials and corresponding transition states, b and c, are defined for each product vibrational state. As total energy increases, the position of these transition states moves in along the reaction coordinate. The increase in level spacings as the chemical bond tightens causes W(E,J) to be smaller than for the loose transition state at the free-rotor asymptote considered in PST. A vibrationally excited channel is also shown.

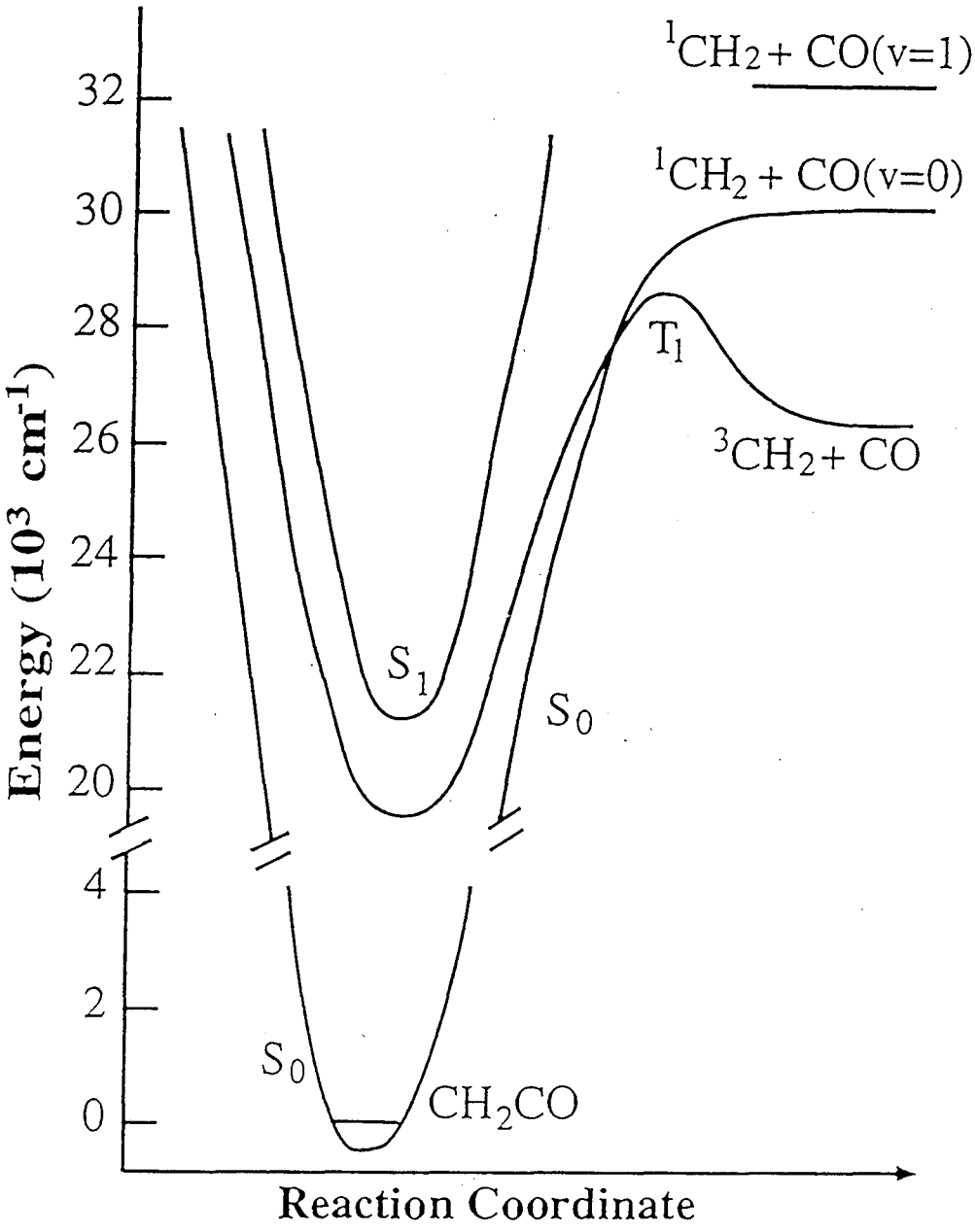

Figure 2. The three lowest lying potential energy surfaces of ketene along the reaction coordinate. The ketene molecule is excited by a UV laser pulse to the first excited singlet state, S_1, undergoes internal conversion to S_0 and intersystem crossing to T_1, and dissociates into $CH_2(\tilde{a}^1A_1)$ + CO (singlet channel) or $CH_2(\tilde{X}^3B_1)$ + CO(triplet channel) fragments. The threshold for the vibrationally excited $CH_2(\tilde{a}^1A_1)$ + CO(v=1) channel is also shown.

References

1. R.G. Gilbert and S.C. Smith, *Theory of Unimolecular and Recombination Reactions* (Blackwell Scientific, Oxford, 1990), and references cited therein.
2. H. Reisler and C. Wittig, *Annu. Rev. Phys. Chem.* **37**, 307 (1986).
3. W. H. Green, C.B. Moore, and W.F. Polik, *Annu. Rev. Phys. Chem.* **43**, 591 (1992).
4. T. Baer and W.L. Hase, *Unimolecular Reaction Dynamics* (Oxford University Press, Oxford, 1996).
5. C.B. Moore, and I.W.M. Smith, *J. Phys. Chem.* **100**, (1996) in press.
6. P. Pechukas and J.C. Light, *J. Chem. Phys.* **42**, 3281 (1965); P. Pechukas, C. Rankin, and J.C. Light, *J. Chem. Phys.* **44**, 794 (1966).
7. M. Quack and J. Troe, *Ber. Bunsenges. Phys. Chem.* **78**, 240 (1974);**79**, 170 (1975);**79**, 469 (1975).
8. J. Troe, *J. Chem. Phys.* **75**, 226 (1981);**79**, 6017 (1983).
9. R.A. Marcus, *J. Chem. Phys.* **85** 5035 (1986); *Chem. Phys. Lett.* **144**, 208 (1988); D.M. Wardlaw and R.A. Marcus, *Adv. Chem. Phys.* **70**, 231 (1988).
10. S.J. Klippenstein and R.A. Marcus, *J. Chem. Phys.* **91**, 2280 (1989).
11. S.J. Klippenstein and R.A. Marcus, *J. Chem. Phys.* **93**, 2418 (1990).
12. C. Wittig, I. Nadler, H. Reisler, J. Catanzarite, and G. Radhakrishnan, *J. Chem. Phys.* **83**, 5581 (1985).
13. G.A. Brucker, S.I. Ionov, Y. Chen, and C. Wittig, *Chem. Phys. Lett.* **194**, 301 (1992).
14. S.J. Klippenstein, L.R. Khundkar, A.H. Zewail, and R.A. Marcus, *J. Chem. Phys.* **89**, 4761 (1988).
15. J. Troe, *Ber. Bunsenges. Phys. Chem.* **92**, 242 (1988).
16. J. Miyawaki, K. Yamanouchi, and S. Tsuchiya, *Chem. Phys. Lett.* **180**,

287 (1991).

17. S.K. Kim, Y.S. Choi, C.D. Pibel, Q.-K. Zheng, and C.B. Moore, *J. Chem. Phys.* **94**, 1954 (1991).
18. L.J. Butler, T.M. Tichnich, M.D. Likar, and F.F. Crim, *J. Chem. Phys.* **85**, 2331 (1986).
19. N.F. Scherer and A.H. Zewail, *J. Chem. Phys.* **87**, 97 (1987).
20. W.F. Polik, D.R. Guyer, W.H. Miller, and C.B. Moore, *J.Chem. Phys.* **92**, 3471 (1990).
21. C.X.W. Qian, A. Ogai, H. Reisler, and C. Wittig, *J. Chem. Phys.* **90**, 209 (1989).
22. W.H. Green, I. Chia-Chen, and C.B. Moore, *Ber. Bunsenges. Phys. Chem.* **92**, 389 (1988).
23. I. Chia-Chen, W.H. Green, and C.B. Moore, *J. Chem. Phys.* **89**, 314 (1988).
24. W.H. Green, A.H. Mahoney, Q.-K. Zheng, and C.B. Moore, *J. Chem. Phys.* **94** 1961 (1991).
25. I. Garcia-Moreno, E.R. Lovejoy, and C.B. Moore, *J. Chem. Phys.* **100**, 8890 (1994).
26. I. Garcia-Moreno, E.R. Lovejoy, and C.B. Moore, *J. Chem. Phys.* **100**, 8902 (1994).
27. E.A. Wade, H. Clauberg, S.K. Kim, A. Mellinger, and C.B. Moore, *J. Phys. Chem.*, submitted; E.A. Wade, A. Mellinger, and C.B. Moore, *J. Chem. Phys.*, submitted.
28. H. Zacharias, M. Geilhaupt, K. Meier, and K.H. Welge, *J. Chem. Phys.* **74**, 218 (1981).
29. J. Miyawaki, T. Tsuchizawa, K. Yamanouchi, and S. Tsuchiya, *Chem. Phys. Lett.* 95, 5700 (1991).

30. D.C. Robie, M. Hunter, J.L. Bates, and H. Reisler, *Chem. Phys. Lett.* **193**, 413 (1992).

31. M. Hunter, S.A. Reid, D.C. Robie, and H. Reisler, *J. Chem. Phys.* **99**, 1093 (1993).

32. S.A. Reid and H. Reisler, *J. Phys. Chem.* **100**, 474 (1996).

33. T.M Ticich, M.D. Likar, H-R. Dubal, L.J. Butler, and F.F. Crim, *J. Chem. Phys.* **87** 5820 (1987).

34. K.-H. Gericke, H.G. Gläser, C. Maul, and F.J. Comes, *J. Chem. Phys.* **92**, 411 (1990).

35. X. Luo and T.R. Rizzo, *J. Chem. Phys.* **93**, 8620 (1990); **96**, 5129 (1992).

36. T.M. Tichich, T.R. Rizzo, H.-R. Dubal, and F.F. Crim, *J. Chem. Phys.* 84, 1508 (1986).

37. J. Yu and S.J. Klippenstein, *J. Phys. Chem.* **95**, 9882 (1991).

38. A.L.L. East, W.D. Allen, and S.J. Klippenstein, *J. Chem. Phys.* **102**, 8506 (1995).

39. S.J. Klippenstein, A.L.L. East, and W.D. Allen, *J. Chem. Phys.* **105**, 118 (1996); **101**, 9198 (1994).

40. H. Gaedtke and J. Troe, *Ber. Bunsenges. Phys. Chem.* **79**, 184 (1975); H. Gaedtke, H. Hippler, and J. Troe, *Chem. Phys. Lett.* **16**, 177 (1972).

41. I.-C. Chen and C.B. Moore, *J. Phys. Chem.* **94**, 263 (1990).

42. I.-C. Chen and C.B. Moore, *J. Phys. Chem.* **94**, 269 (1990).

43. E.D. Potter, M. Gruebele, L.R. Khundkar, and A.H. Zewail, *Chem. Phys. Lett.* **164**, 463 (1989).

44. S.C. Smith, *Chem. Phys. Lett.* **243**, 359 (1995); personal communication.

Chapter 2. Experimental

Ketene is prepared by passing acetic anhydride through a red-hot quartz tube heated by running current through a NiCr wire. Ketene is then trapped at 77 K and distilled twice from 179 K (*n*-hexane slush) to 77 K (liquid nitrogen). Prior to use, the ketene is transferred to a bubbler maintained at 179 K (*n*-hexane slush), where ketene's vapor pressure is 50 torr. 1.5 atmospheres of He carrier gas are bubbled through the ketene sample and then flowed into the pulsed nozzle. The ketene is cooled in a supersonic jet, and the rotational temperature of ketene in the jet is 4.1 ± 0.7 K.[1] Two different pulsed valves were used, a Newport BV100 and a General Valve. The driving voltage for the General Valve was determined by observing the VUV spectrum of 100 ppm CO in He, and increasing the voltage until the rotational spectrum produced by the General Valve was identical in number of lines observed and peak height ratios of those lines to that produced by the Newport BV100. The higher the voltage used to drive the General Valve, the more quickly the valve opens, the shorter the rise time of the gas pulse, and the colder the resultant spectrum. The beam temperature given was measured using the General Valve, but is very close to the estimated temperature using the Newport BV100.

The cold ketene is excited with UV pulses with wavelengths from 294 to 310 nm; this corresponds to energies 0 to 1720 cm^{-1} over the threshold for production of CO(v=1) along the singlet surface. The CO fragments were detected by monitoring the vacuum ultraviolet (VUV) fluorescence following excitation of the $\tilde{X}\,^1\Sigma^+$ (v" = 0, J") to $\tilde{A}\,^1\Pi$ (v' = 3, J') and $\tilde{X}\,^1\Sigma^+$ (v" = 1, J") to $\tilde{A}\,^1\Pi$ (v' = 5, J') transitions. Several different laser systems were used in these experiments, since different photolysis energy regions presented different

problems. A general schematic of the experiment is given in Figure 3.

At photolysis wavelengths below 300 nm, delay times of up to 200 ns between the photolysis and the probe lasers are required, as the solar blind PMT is sensitive to the photolysis pulse. The second harmonic of a Nd:YAG (Spectra-Physics DCR-4) is used to pump the photolysis laser (Lambda-Physik FL2002 dye laser (Rhodamine 610 or Rhodamine 590)). This dye laser output is doubled in a KDP crystal to provide the photolysis pulse, 7 ns and 5-13 mJ. The third harmonic of a second Nd:YAG (Quantel YG-682) is used to pump the probe dye laser (Spectra-Physics PDL-3 (Coumarin 440)) whose output is tripled in Xe to provide VUV.[2] The PDL-3 produces a pulse of 7 ns and 15-25 mJ, with a beam size of 2mm x 6 mm immediately after the dye laser. The output of the PDL-3 is not at all round, and is also highly divergent. To control this divergence, the beam size of the dye laser output is reduced from 4mm x 12 mm to 2 mm x 6 mm with a two-to-one telescope. The reduced beam is then focused by a 7.5 cm f.l. quartz lens into a 10 cm long tripling cell filled with Xe at 40-60 torr. The conversion efficiency of the frequency tripling process is estimated to be 10^{-6}. The resultant divergent VUV beam is collimated, or slightly focused, with an 8 cm f.l. CaF_2 lens, which is 13 cm from the quartz focusing lens and about 25 cm from the center of the molecular beam. It is not possible to determine precisely whether the VUV beam is slightly focused or slightly divergent, but the spacing between the two lenses was adjusted for maximum CO LIF signal. Also, it should be noted that the 8 cm f.l. CaF_2 lens is calibrated for UV/Vis light, and actually acts as a 5 cm f.l. lens at the VUV wavelengths of interest.

At wavelengths above 300 nm, the solar blind PMT is no longer sensitive to the photolysis pulse, and one Nd:YAG (Spectra-Physics DCR-4) is used to pump both photolysis and probe dye lasers. The second and third

harmonics are separated, and the 532 nm is used to pump the photolysis laser (Lambda-Physik FL2002 (Rhodamine 640, Sulfarhodamine 640, or Kiton Red 620)), while the 355 nm is used to pump the probe laser (Spectra-Physics PDL-3 (Coumarin 440)). Using the same Nd:YAG laser as a pump for both dye lasers greatly reduces timing jitter, but restricts the delay between pump and probe to 50 ns.

At wavelengths above 308 nm, less than 200 cm^{-1} above the threshold for production of singlet channel CO(v=1), the amount of CO produced is small, and so the resultant LIF signal-to-noise ratio is poor. To increase the amount of VUV produced, and thereby to improve the signal-to-noise by a factor of ~20, a concentric heat pipe using Mg vapor as the non-linear medium and Kr as the phase matching gas was used in place of the Xe tripling cell.[3] A schematic of the heat pipe, based on a system built by Vidal and co-workers,[4] is shown in Figure 4. The system is based on two concentric pipes. The inner pipe contains Mg and Kr, while the outer pipe contains Na and He. When the system is heated, the sodium is at its boiling point. As the Na boils, it drives the He out of the tube. Since the Na pressure is identical to the He pressure, setting the He pressure sets the precise temperature of the Na which in turn sets the temperature of the Mg vapor. The optimum temperature is 740°C, which is equivalent to a He pressure of 175 torr.[4] In order to avoid large pressure fluctuations, there is a large excess volume, which is about 1.5 times larger than the total Na/He system, attatched to the Na tube. This excess volume serves as an overflow for the He if the pressure were to rise rapidly. With the temperature inside the Mg pipe set by the Na pipe, the only remaining variable to control is the Kr, which is necessary for phase matching. The basic Kr pressure is set when the Mg pipe is filled, to

245 torr, but fine adjustments are necessary. These adjustments are made possible by a bellows attatched to the Mg pipe. By adjusting the bellows properly, it is possible to increase the VUV output by an order of magnitude compared to that obtained when the pressure is not tuned properly.[4] This adjustment is very sensitive, which is why the bellows is necessary; a change in pressure of a few torr is all that is necessary.

Since the Mg heat pipe involves very hot metals, there are several precautions that should be taken. The excess volume on the Na line in part serves to stabilize the He/Na pressure, but it also allows the system to survive rapid rises in pressure that could cause leaks. The system should never be heated without the cooling water turned on, as this will damage the windows. The system must also be carefully checked for leaks, as even very small leaks will cause the Mg and Na to form oxides which will reduce the lifetime of the system. Large leaks could lead to a fire hazard, and for this reason a extinguisher rated for metal fires should be kept on hand at all times.

The Mg oven requires two pump lasers with similar beam profiles. In these experiments, the second and third harmonics of a Nd:YAG (Spectra-Physics DCR-4) are separated. The 532 nm is used to pump the photolysis laser, a dye laser (Spectra-Physics PDL-3 (Rhodamine 640)) whose output is passed through a KDP doubling crystal and focused into the chamber via a 1 m lens. The third harmonic pumps one of the probe lasers, another dye laser (Lambda-Physik FL2002 (Coumarin 440)) which is held fixed at the wavelength of the two-photon Mg transition, 431.005 nm, which corresponds to a resonance at 46403.15 cm^{-1}. The other probe laser, used to tune the VUV output, is a third dye laser (Lambda-Physik ScanMate 2E) pumped by the 355 nm output of a Nd:YAG (Quantel YG-682). The two probe lasers are

collimated using two separate 2-to-1 reducing telescopes, after which the beam diameters are ~3mm, and are then brought onto each other using a glan prism, which requires that the two beams are polarized perpendicularly to each other. The combined beams are then passed through a $(1/4)\lambda$ plate, coated for 440 nm, to produce circularly polarized light. Without the $(1/4)\lambda$ plate, the fixed frequency probe laser will be tripled in the Mg vapor, $3\omega_1$. When the two probe lasers are circularly polarized in opposite directions, however, mixing only occurs for $2\omega_1+\omega_2$, due to conservation of angular momentum. It is important to note that the optimum Kr pressure for phase matching is a function of ω_2, and is different for four-wave mixing than for tripling unless ω_2 is very close to ω_1.[5]

After passing through the $(1/4)\lambda$ plate, the beams are focused with a 2 m lens, then sent into the Mg heat pipe oven, which is closed off from the atmosphere with a fused silica window. The lens position should be adjusted so that the focal point of the beams is in the center of the heat pipe oven. Additionally, the divergence parameter of each beam is adjusted with the independent telescopes so that the focal points of both beams overlap in the center of the Mg heat pipe oven. The output window, mounted between the heat pipe oven and the beam chamber, is CaF_2. The windows are mounted so that the window center is not along the beam axis, so that the windows can be rotated without opening the oven, so that small burns caused by the laser beam do not make changing windows necessary. As the generated VUV beam is quite well collimated, with an approximate beam diameter of 2 mm in the interaction region, there is no need for any additional collimating optics.

The Mg oven is also used for all of the PHOFEX experiments, where signal-to-noise is critical. In those experiments, the KDP doubling crystal is used as a part of an Inrad Autotracker II, a device which allows the UV to be scanned continuously.

Regardless of the VUV generation system used, Xe or Mg/Kr, the remainder of the apparatus is the same. The wavelength of the photolysis laser is calibrated in the red to ± 0.6 cm^{-1} by Ne transistions using a Tl/Ne optogalvanic lamp (Hamamatsu). A small portion of the UV beam is detected with a photodiode and used to normalize for UV intensity fluctuations. The laser induced fluorescence (LIF) of CO is detected by a VUV PMT (EMR 542G-09-18, MgF_2) mounted perpendicular to the laser beams and the supersonic jet about 5 cm from the intersection. A 2.5 mm thick cultured quartz window (Acton, CQ-1D 50% transmission at 150 nm) is placed before the VUV PMT to filter out any scattered light. The CO LIF spectra show a linewidth of approximately 0.7 and 1.1 cm^{-1} when the VUV is generated by Xe tripling or four-wave mixing in Mg, respectively. A portion of the VUV beam, which is not significantly attenuated by the CO in the beam, is reflected off of a 45° window, detected with another VUV PMT (EMR 541G-08-17, MgF_2), and used to normalize for VUV intensity fluctuations. The photolysis and probe laser pulses enter the vacuum chamber through opposing baffled sidearms and pass collinearly 1.5 cm from the pulsed valve. The photolysis beam is polarized vertically and the probe beam is polarized horizontally when VUV is generated by Xe tripling. When VUV is generated using the Mg heat pipe oven, the resultant VUV is circularly polarized.

The amplified CO LIF signal, the two laser normalization signals, and the Tl/Ne optogalvanic signal are sent into gated integrators (SRS 250), digitized by an A/D interface board, and processed with a microcomputer

(Fountain XT), which also controls the laser scanning and normalizes the signal. The pulsed valve and Nd:YAG laser are triggered with a delay generator (Stanford Research Systems DG535).

In order to determine rotational distributions, the photolysis laser was set to a particular energy, from 57 to 1720 cm^{-1} over the threshold for singlet production of CO(v=1), and the probe laser was scanned to collect the spectrum of the CO(v=1) fragment. The relative populations of CO rotational states are calculated from the LIF intensities, using the formula given by Greene and Zare.[6]

$$I(J'',J') \propto C(J'')\, S(J'',J')\, A_0^{(0)}\, B(J'',J') \qquad (2\text{-}1)$$

Here $A_0^{(0)}$ is the monopole moment, which is equal to unity for photofragmentation, S(J'',J') is the Hönl-London factor, and B(J'',J') is the excitation-detection configuration factor given by Greene and Zare[6] for the coaxial geometry. The populations from P, Q, and R branches are averaged for the same J'' state of CO, and each data point is averaged over four spectra.

Vibrational branching ratios (P(CO(v=1))/P(CO(v=0))) were measured at several energies up to 500 cm^{-1} over the threshold for production of CO(v=1) by scanning the probe laser to collect spectra in the CO(v=0) and CO(v=1) regions and fixing the photolysis laser on the desired energy. To minimize the effects of beam pointing instability, only a small portion of each CO(v=0) and CO(v=1) spectrum was collected. This portion of the spectrum contained at least 5 rotational lines, except at the lowest energies where there are fewer resolvable lines in the CO(v=1) spectra and all possible rotational lines were used.

When VUV was produced by tripling in Xe, the CO(v=0) and CO(v=1)

data were recorded alternately, so that it was less likely that the overlap between the pump and probe lasers changed significantly between collection of CO(v=0) and CO(v=1) data. When VUV was produced by four-wave mixing in Mg vapor, it was necessary to scan the tuning probe laser over a very wide region in order to collect CO(v=0) and CO(v=1) data. As a result, the Kr pressure had to be adjusted to the proper phase matching conditions, and the beam overlap had to be optimized between collection of CO(v=0) and CO(v=1) data. In this case, at least three spectra were taken for CO(v=1), then a similar number of spectra were taken for CO(v=0), and finally two spectra were again taken in CO(v=1). The signal of the first and second set of CO(v=1) spectra were compared in order to check for alignment effects, and if significant alignment effects were observed, the data was not used.

As the relative population of a given rotational state, P(v,J″), has already been determined from the rotational distributions, the total population of the vibration band is given by

$$S(v) = S(v,J'')/P(v,J'') \qquad (2\text{-}2)$$

where S(v,J″) is the signal intensity of a particular rovibrational line. The vibrational signal intensity, S(v), for each possible J″ state in one series of scans were averaged together. Once the total population has been determined, the vibrational branching ratio is calculated as in Kim et al.[2]

Finally, the photolysis laser was scanned while the probe laser was set to a single rovibrational transition in order to collect photofragment excitation (PHOFEX) spectra. PHOFEX spectra were collected for the Q3 and Q7 lines for the first 300 cm^{-1} over threshold for production of CO(v=1) from the singlet surface. The VUV probe was produced by four-wave mixing in Mg vapor, and only those PHOFEX spectra that are reproducible to better than 10%, as judged by eye, are considered reliable.

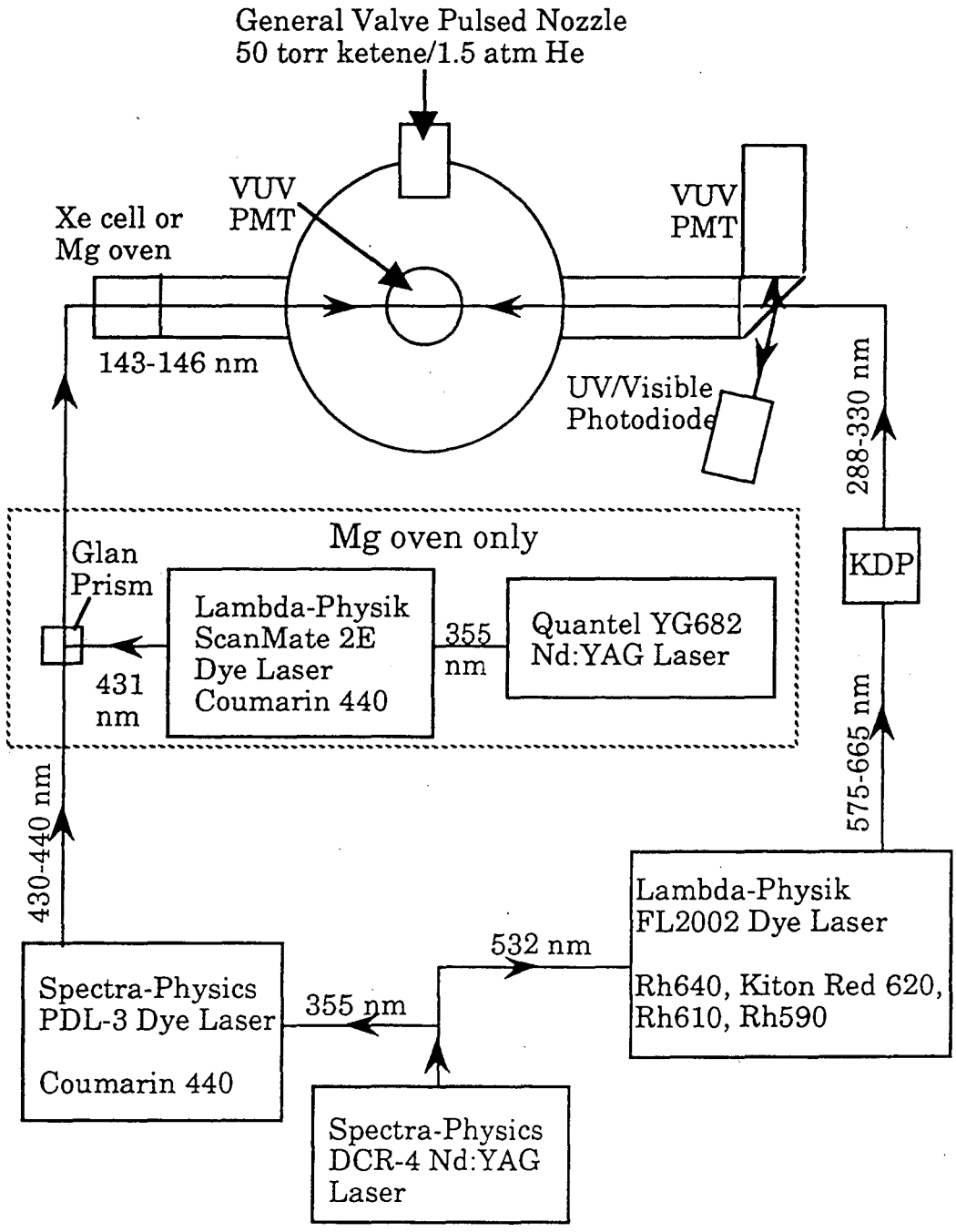

Figure 3. Schematic of experimental apparatus.

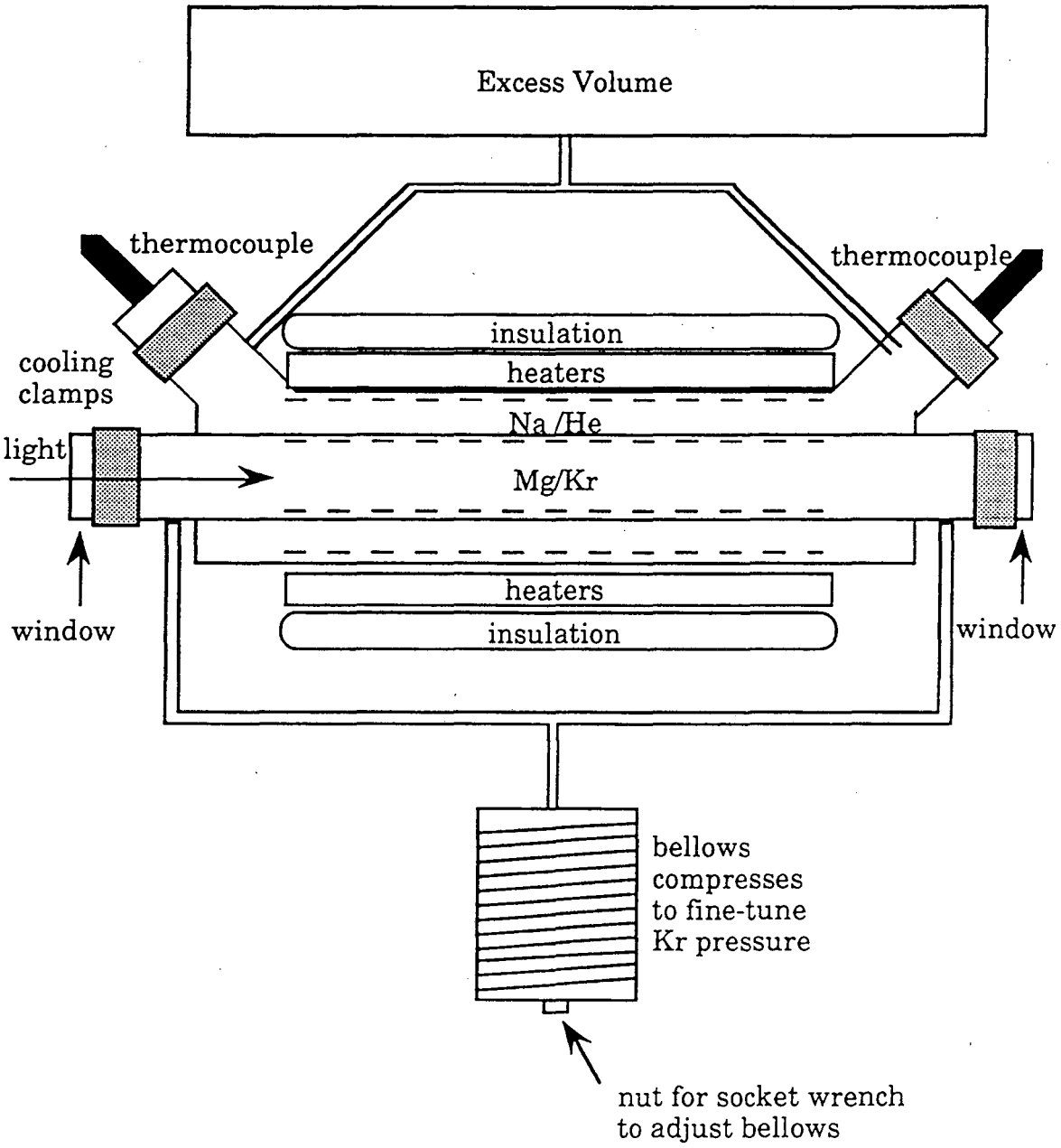

Figure 4. Schematic of Mg heat pipe oven. Inner pipe holds ~100 gm Mg, while outer pipe holds ~500 gm Na. The dashed lines near the pipe indicate the mesh used to allow the molten metals to wick from the cooler ends to the hotter center. The mesh is spot welded onto a steel spring, to better control its shape. The system is more fully described in the text.

References

1. C.-K. Ni, E.A. Wade, M.V. Ashikhmin, and C.B. Moore, *J. Mol. Spectr.*, **177**, 285-293 (1996).
2. S.K. Kim, Y.S. Choi, C.D. Pibel, Q.-K. Zheng, and C.B. Moore, *J. Chem. Phys.* **94**, 1954 (1991).
3. E.A. Wade, H. Clauberg, S.K. Kim, A. Mellinger, and C.B. Moore, *J. Phys. Chem.*, submitted; E.A. Wade, A. Mellinger, and C.B. Moore, *J. Chem. Phys.*, submitted.
4. B. Steffes, X. Li, A. Mellinger, and C.R. Vidal, *Appl. Phys. B*, **62**, 87 (1996).
5. A. Mellinger, personal communication.
6. C.H. Greene and R.N. Zare, *J. Chem. Phys.* **78**, 6741 (1983).

Chapter 3. The Dynamics of Rotational Energy Release for Dissociation of Singlet Ketene and the Singlet/Triplet Branching Ratio

I. Introduction

Statistical rate theories such as Rice-Ramsperger-Kassel-Marcus (RRKM) are providing a qualitatively and quantitatively satisfactory model for the dynamics of unimolecular reactions which pass through a saddle point and therefore a well-defined transition state.[1-4] When there is no barrier for recombination, however, the definition of the transition state and the dynamics of energy flow for a dissociation reaction are much more complex. Several models, including phase space theory (PST),[5] the statistical adiabatic channel model (SACM),[6-8] separate statistical ensembles (SSE),[9] and variational RRKM (var. RRKM),[10-12] have proven to be quantitatively useful for the prediction of rate constants and vibrational excitation of products.[1-4] Models for the dynamics of rotational energy release have very limited predictive value and are often qualitatively unsatisfactory. The first detailed rotational distribution data was for NO from NCNO fragmentation.[13] These data matched the purely statistical distributions of PST from threshold to at least 1800 cm^{-1} above threshold. CO rotational distributions from ketene fragmentation were subsequently fit to a PST distribution for the singlet [$CH_2(\tilde{a}\ ^1A_1)$ + CO] part of the fragmentation yield plus a dynamically controlled Gaussian distribution for the triplet [$CH_2(\tilde{X}\ ^3B_1)$ + CO] part.[14] These results for NCNO and CH_2CO gave a comfortable qualitative and quantitative picture of strong rotation-translation coupling after passage through the transition state and statistical release of energy to product

rotations.

Rotational distributions for the photodissociation of HOOH and NO_2 complicated this picture. For NO_2, the NO rotational distributions near the statistical threshold are generally consistent with PST, but also exhibit the statistical fluctuations about PST expected when single molecular eigenstates are resolved.[15] However, well above threshold, NO rotational distributions exhibit an oscillatory behavior which is modeled by Franck-Condon overlap of the bending wavefunctions of a tightened transition state with the free rotor wavefunctions of NO.[15] For HOOH→2OH, the rotational distributions produced by exciting overtones of the OH stretch are significantly colder than PST but could be fit by SACM.[16] When a combination band that included the torsional motion as well as the OH stretch was excited, however, the rotational distribution was not statistical, possibly because the initial torsional motion caused additional angular momentum constraints.[16]

Ketene experiments are complicated by its simultaneous fragmentation to both singlet and triplet CH_2.[3] The lowest electronic states of ketene are illustrated in Figure 2. Upon excitation to the S_1 state, the molecule undergoes rapid internal conversion and/or intersystem crossing to the lower electronic states.[3] Measurements on $^1CH_2$ from ketene dissociation give statistical (PST) distributions for rotational excitation from threshold to 200 cm^{-1} above. However, at higher energies the rotational distributions become progressively colder than statistical, reaching a factor of 5 colder at 2900 cm^{-1} above threshold. The $^1CH_2(J_{KaKc})$ rotational distributions[17,18] suggest that CO rotational distributions should be reexamined for departures from statistical behavior at energies well above threshold. An approach is suggested by the

finding of Kim *et al.* that for CO(v=1) produced at 357 cm^{-1} over its threshold there is no contribution from the triplet channel.[14] Recently, Wodtke and co-workers have also measured correlated-product-state distributions for CO(v=1, J_{CO}=4,6 and 8) at 308 nm, 208 cm^{-1} above the CO(v=1) production threshold.[19] While some triplet channel contribution was observed, the relative signal due to the triplet channel was much smaller than would be expected for CO(v=0) at the same energy over its threshold. Thus CO(v=1,J_{CO}) distributions are measured as a function of excitation energy in this work in order to determine the dynamics of energy release to CO for dissociation on the singlet surface.

The singlet reaction channel dominates from a few hundred cm^{-1} above its reaction threshold.[14,20] Hayden *et al.* found that the singlet yield at 308 nm, 2351 cm^{-1} above the singlet channel threshold, is at least 0.9.[20] Kim *et al.* calculated the singlet yield assuming that the singlet channel CO rotational distributions are given accurately by PST. Accurate determinations near threshold were possible, but only an estimate of 0.75±0.2 could be derived at 2521 cm^{-1}.[14] Recent measurements of correlated-product-state distributions for CO at 308 nm by Wodtke and co-workers show that the yield is at upper limit of this range.

II. Results

CO(v=1) rotational state distributions are measured at 57, 110, 200, 357, 490, 1107, 1460, and 1720 cm^{-1} over the threshold for production of CO(v=1) (2200, 2253, 2343, 2500, 2633, 3250, 3603, and 3863 cm^{-1}, respectively, over the threshold for production of $^1CH_2(0,0,0)$ and CO(v=0)). These distributions are shown in Figure 5, along with their best fits which will be described more completely in Sect. IV. At 57, 110, and 200 cm^{-1} over the CO(v=1) production threshold, there is a bimodal distribution. The sharp peak at low J is due to the singlet channel, and the broad distribution at higher J is due to the triplet. The fractional yield of CO(v=1) for the singlet channel, assuming that the yield for the singlet and triplet channels totals unity, is measured as 0.4±0.1, 0.5±0.1, and 0.80±0.05 for 57, 110, and 200 cm^{-1}, respectively. At higher energies, there is no measurable triplet channel contribution observed, and the distributions can be assigned purely to the singlet channel.

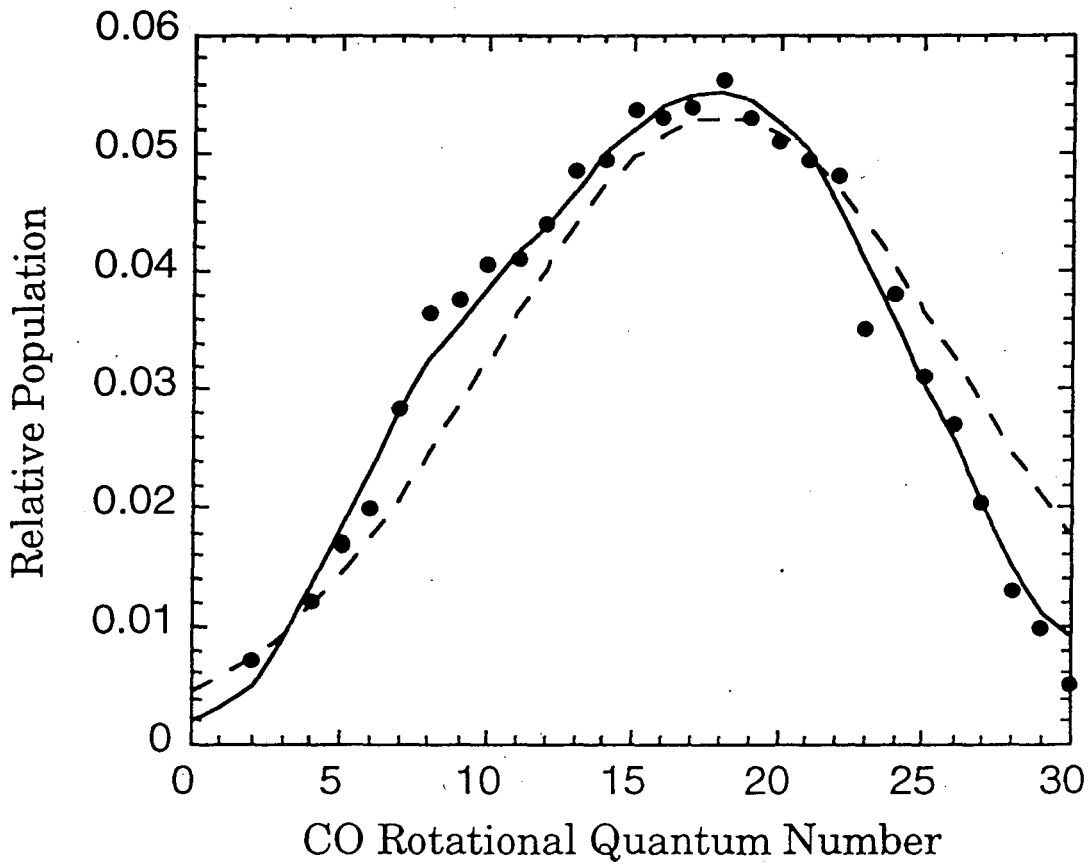

Figure 5. This distribution is the CO(v=0) rotational distribution at 10 cm^{-1} below the singlet channel threshold, taken from Ref. 14, and the solid line is its best fit using two Gaussians. The dashed line is the Gaussian centered at J=18 with a width of 11.4 used to fit the CO(v=0) distributions to calculate the singlet yield. The remaining distributions (Figure 5b-5i) are rotational distributions of CO(v=1) from ketene dissociation at energy E above the singlet threshold for production of CO(v=1) and their best fits as described in Sect. IV.

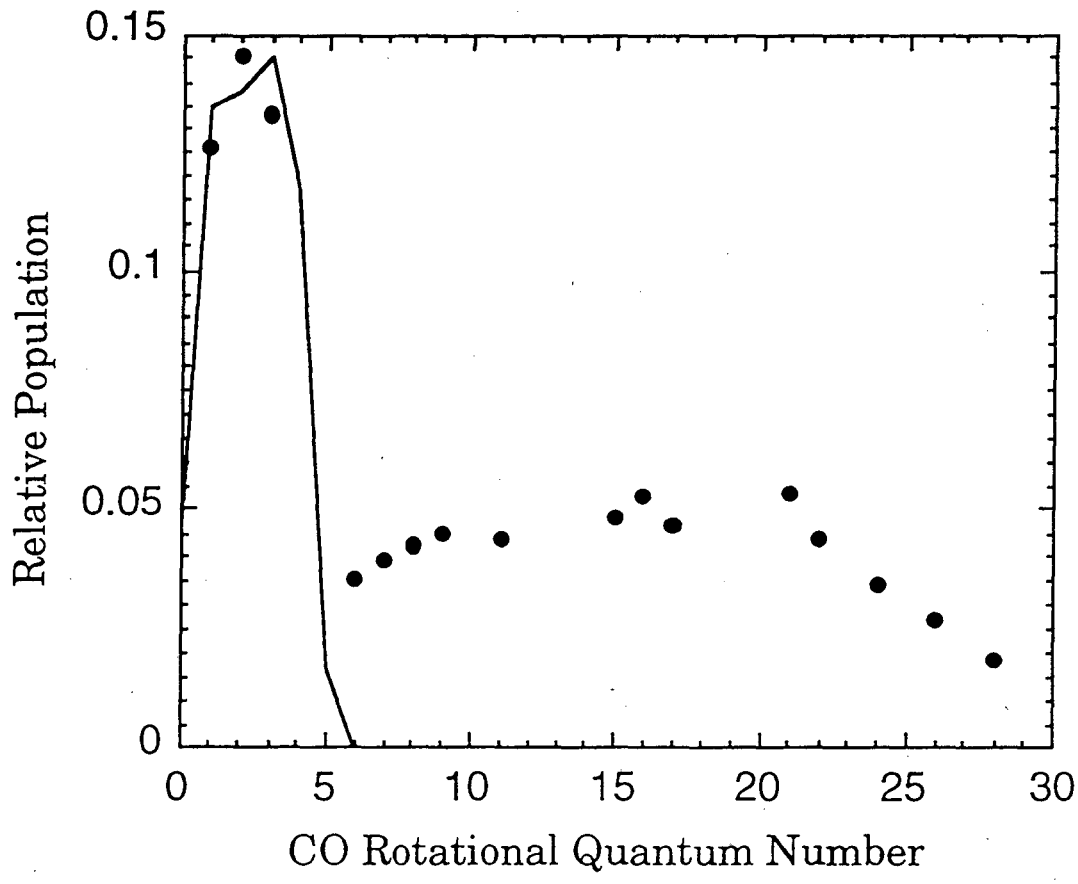

Figure 5b. Rotational Distribution at 57 cm^{-1}. PST scaled by 0.60.

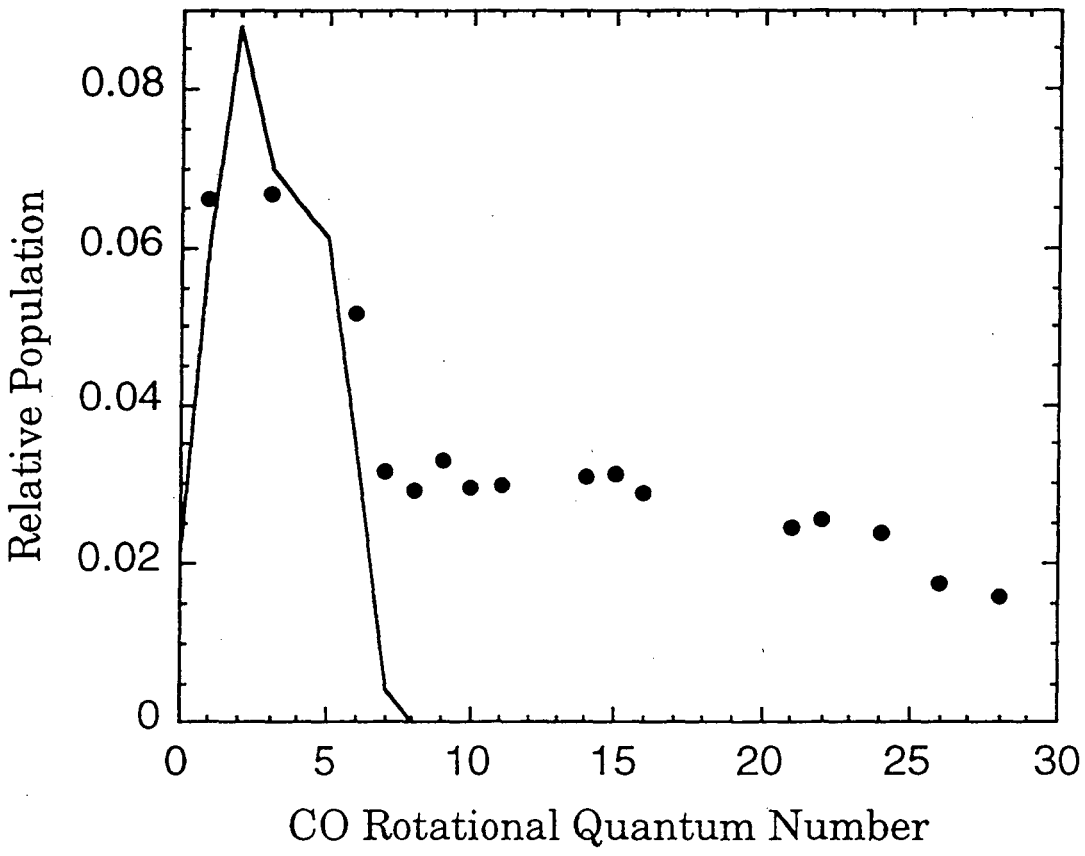

Figure 5c. Rotational Distribution at 110 cm^{-1}. PST scaled by 0.50

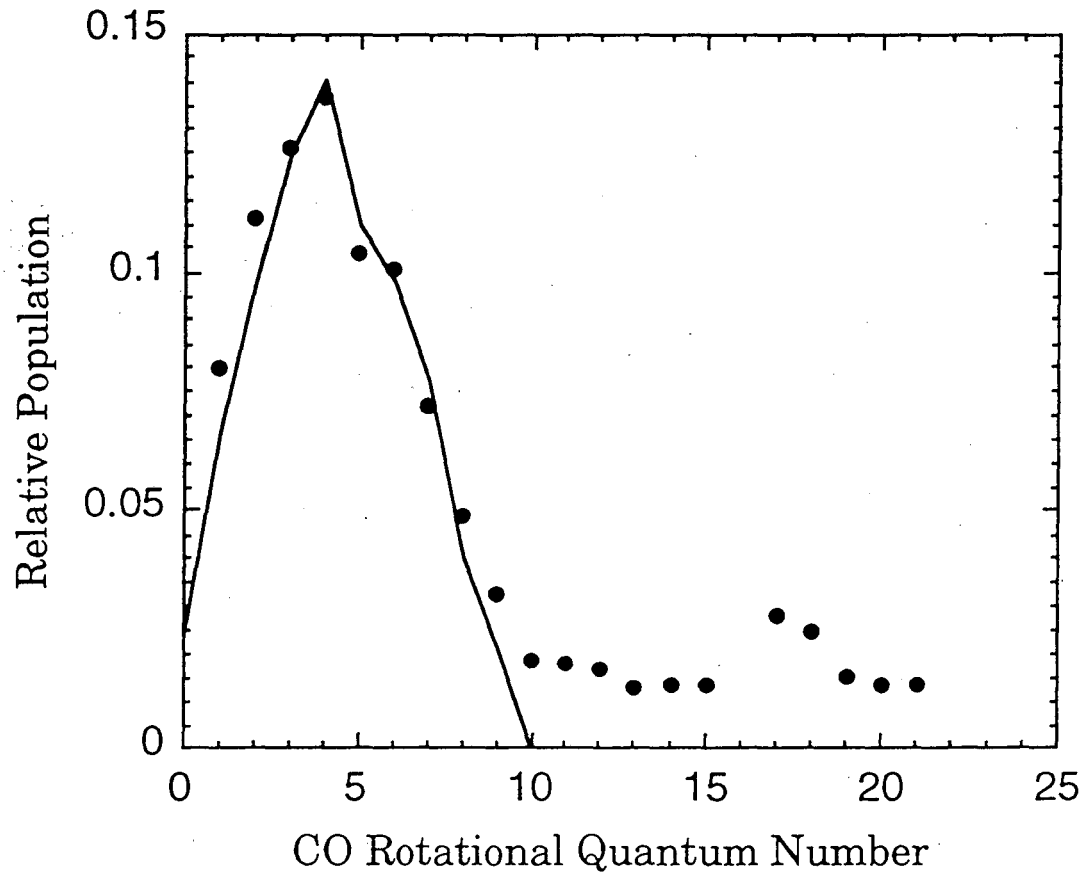

Figure 5d. Rotational Distribution at 200 cm^{-1}. PST scaled by 0.80.

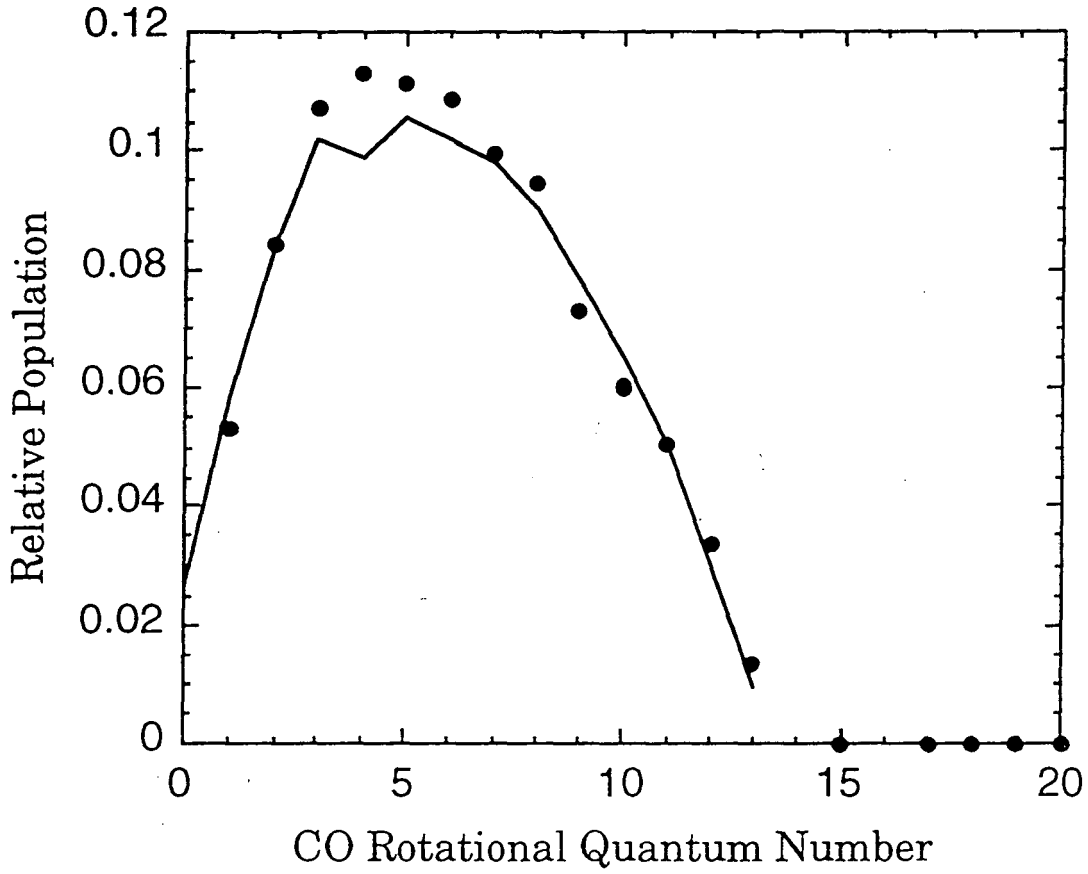

Figure 5e. Rotational Distribution at 357 cm^{-1}.

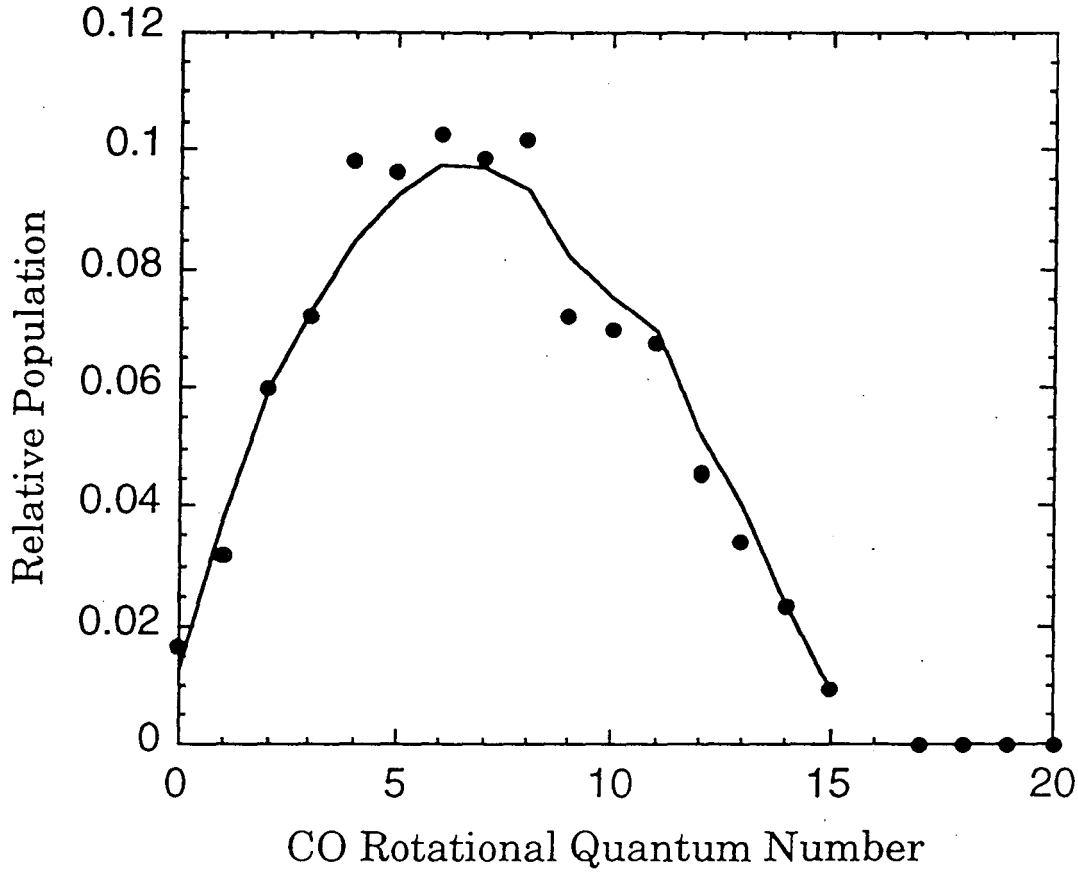

Figure 5f. Rotational Distribution at 490 cm^{-1}.

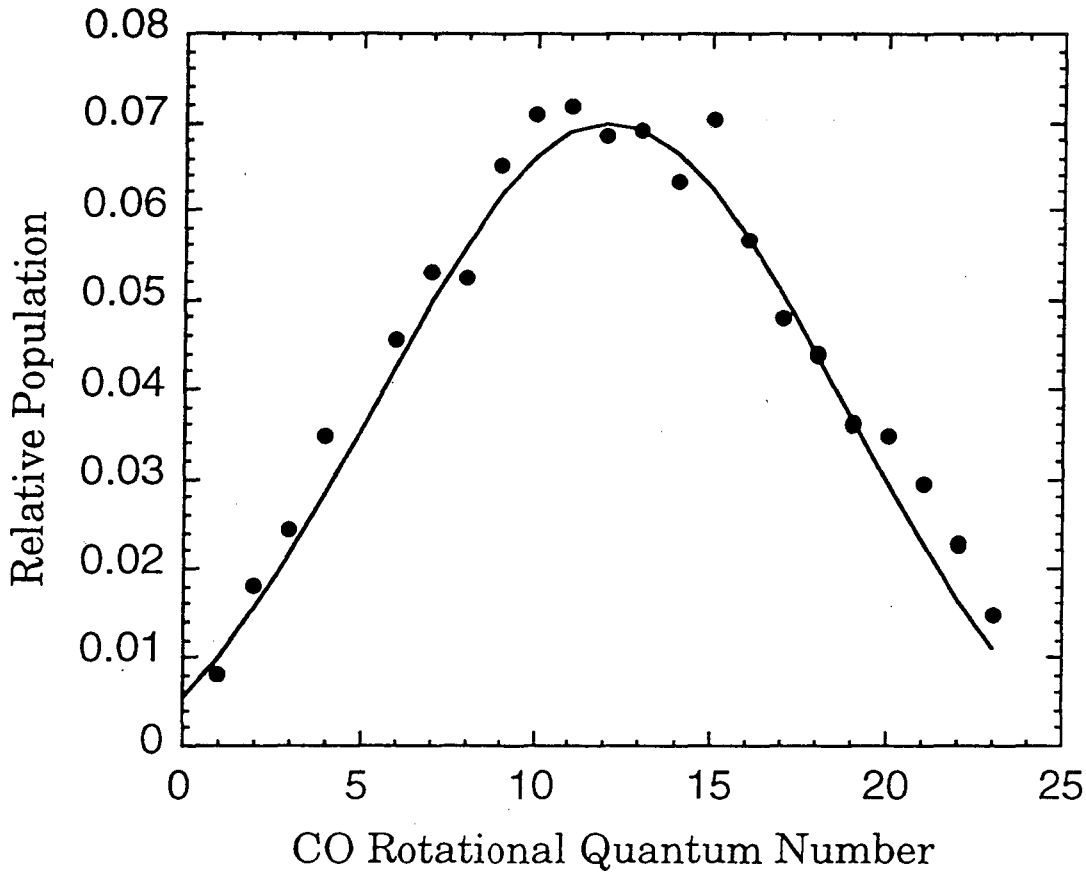

Figure 5g. Rotational Distribution at 1107 cm^{-1}.

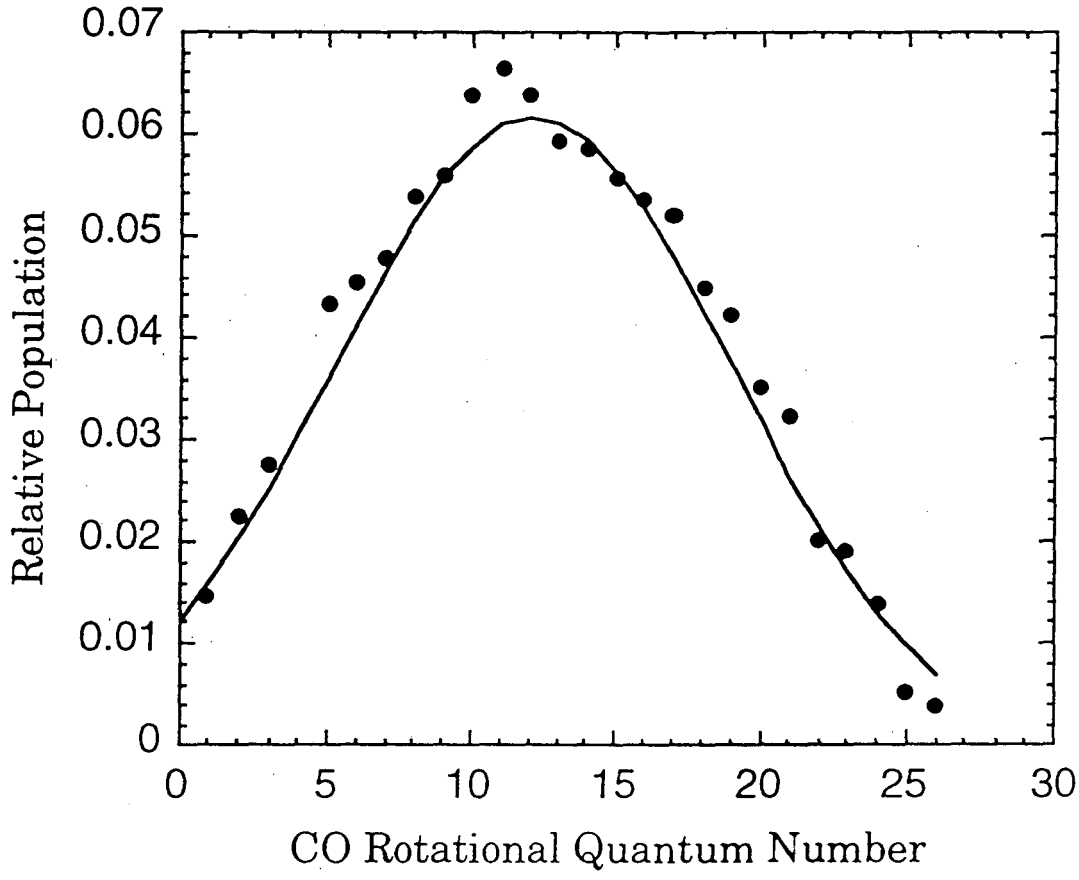

Figure 5h. Rotational Distribution at 1460 cm^{-1}.

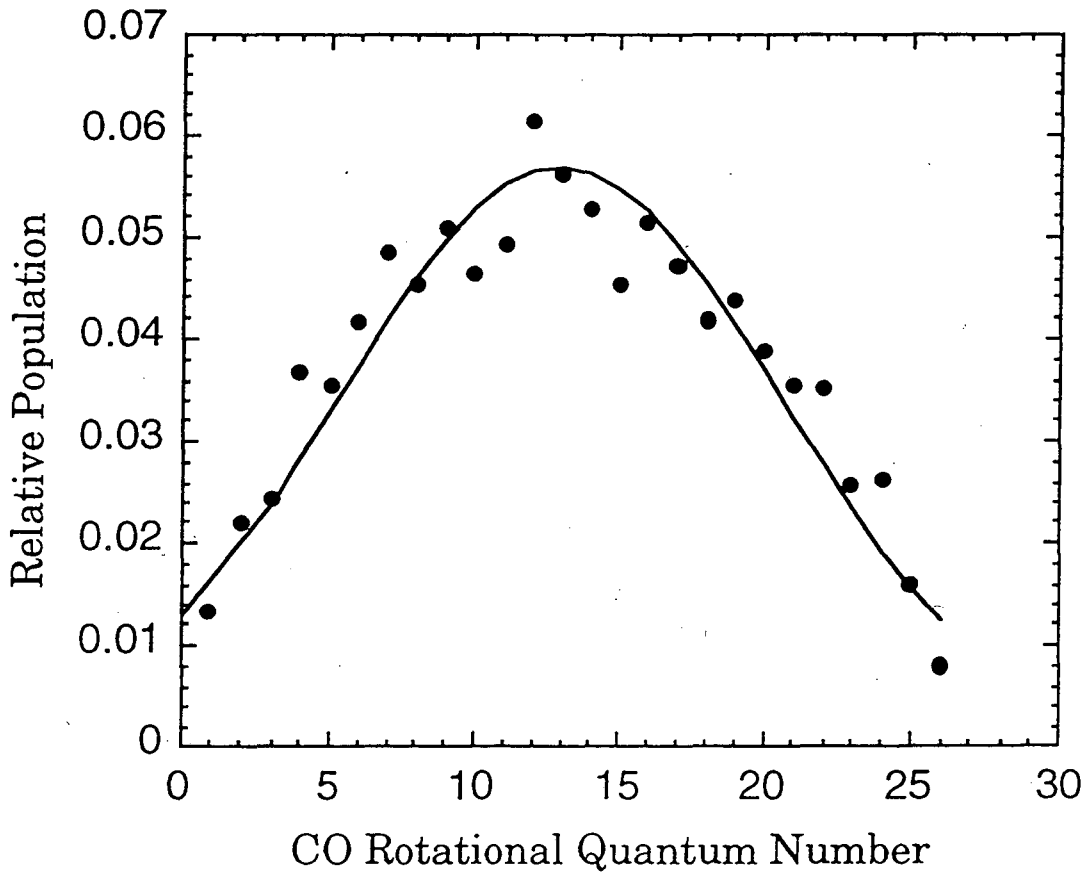

Figure 5i. Rotational Distribution at 1720 cm^{-1}.

IV. Modeling Rotational Distributions

These CO(v=1) distributions may be compared to a variety of limiting dynamical models for energy release to the reaction products. The completely statistical limit, in which energy is coupled rapidly among all degrees of freedom as the fragments separate, is PST. In PST, the transition state is assumed to be at infinite separation, and the number of open reaction channels at a given energy is simply the total number of accessible states:

$$W(v,J_{CO},J',J'',K_a'',E) = \sum_{J_{KaKc}} \sum_{jj=|J_{KaKc}-J_{CO}|}^{jj=J_{KaKc}+J_{CO}} \sum_{l=|J'-jj|}^{l=J'+jj} \Theta(x) \qquad (3\text{-}1)$$

$$x = E + E_{rot}(J'',K_a'') - D_0 - E_{CO} - E_{CH_2} \qquad (3\text{-}2)$$

where $W(v,J_{CO}, J',J'', K_a'',E)$ is the number of accessible states at that energy for a given state of CO, (v,J_{CO}); J_{KaKc} denotes the rovibrational states of methylene; E_{CH_2} and E_{CO} are the internal energy of methylene and CO, respectively ; v is the vibrational state of CO; J' and J'' are the rotational quantum numbers of excited state and ground state ketene, respectively, such that J'=J'' or J''±1; K_a'' is the K_a quantum number for ground state ketene, which is treated as a prolate symmetric top; *l* is the orbital angular momentum quantum number; E_{rot} is the initial rotational energy of the parent ketene molecule; D_0 is the threshold energy for singlet dissociation; and $\Theta(x)$ is the Heaviside function. To determine a rotational distribution, $P(v,J_{CO},J',J'', K_a'',E)$ is calculated for each J_{CO} state and averaged over J'=J''±1, J'' and K_a'' for a Boltzmann rotational distribution at 4K

$$P(v,J_{CO},J',J'',K_a'',E) = \frac{W(v,J_{CO},J',J'',K_a'',E)}{\sum_{J'_{CO}} W(v,J'_{CO},J',J'',K_a'',E)} \qquad (3\text{-}3)$$

$$P(v,J_{CO},E) = \sum_{J',J'',K_a''} P(J',J'',K_a'')P(v,J_{CO},J',J'',K_a'',E) \qquad (3\text{-}4)$$

where $P(J',J'', K_a'')$ is the product of the Boltzmann rotational distribution for the ground state and the Hönl-London factor for the transition. The resulting distributions are shown in Figures 5-7.

The rotational distribution of methylene has been measured[17] and is known to be significantly colder than PST for energies well above the reaction threshold. Thus it makes sense to calculate the most random distribution of $CO(v=1,J_{CO})$ consistent with the observed $^1CH_2$ rotational distribution. The energy available for the CO fragment is assumed to randomize freely subject to the constraint of the observed methylene distributions.[17] In this constrained PST (CPST), a PST distribution for the CO(v=1) fragment is calculated for each energetically accessible $^1CH_2$ rovibrational state.

$$W(v,J_{CO},J_{KaKc},J',J'',K_a'',E) = \sum_{jj=|J_{KaKc}-J_{CO}|}^{jj=J_{KaKc}+J_{CO}} \sum_{l=|J'-jj|}^{l=J'+jj} \Theta(x) \qquad (3\text{-}5)$$

where x is as defined in Equation 3-2. These distributions are then weighted by the experimental population of that $^1CH_2$ rovibrational state,[17] $P_{exp}(E,J_{KaKc})$, and summed together. The $P_{exp}(E,J_{KaKc})$ for $^1CH_2$ +CO(v=1) is assumed to be the same as for $^1CH_2$ +CO(v=0), where E is referenced to the respective product vibronic channel thresholds. Dynamics beyond the transition state appear to be vibronically adiabatic[3] and there is no reason to expect a substantial difference in rotation-translation couplings and dynamics to result from the small difference in bond length or dipole moment between CO(v=0) and CO(v=1).

$$P(v,J_{CO},J_{KaKc},J',J'',K_a'',E) = \frac{W(v,J_{CO},J_{KaKc},J',J'',K_a'',E)}{\sum_{J'_{CO}} W(v,J'_{CO},J_{KaKc},J',J'',K_a'',E)} \quad (3\text{-}6)$$

$$P(v,J_{CO},J',J'',K_a'',E) = \sum_{J_{KaKc}} P(v,J_{CO},J_{KaKc},J',J'',K_a'',E)P_{exp}(J_{KaKc},E) \quad (3\text{-}7)$$

When the experimental population of $^1CH_2$ matches PST, PST and CPST are identical.

Since the previously measured $^1CH_2$ rotational distributions did not include all accessible rovibrational states,[17] the distributions are approximated by calculating a Boltzmann distribution at the appropriate temperature for the energy of interest, estimated by a linear fit to the Boltzmann temperatures determined in Ref. 17. The Boltzmann distributions are cut to zero population at the maximum available energy. It is possible that CPST overestimates low-J_{CO} states in the CO(v=1) rotational distributions (see Figure 7) because $^1CH_2$ distributions are likely to fall more rapidly than the thermal distributions as the maximum energy is approached. CPST calculations with the high-energy tail of the J_{KaKc} distributions cut off at the maximum and at 80% of the maximum energy are shown in Figure 6. The difference between the resulting CO distributions is smaller than the experimental uncertainties in population measurements and not a concern. The yield of vibrationally excited $^1CH_2(0,1,0)$, above its threshold at 1352.5 cm^{-1}, was calculated using SSE,[9]

$$P(v) = \frac{(E-E_v)^{3/2}}{\sum_{v'}(E-E_{v'})^{3/2}} \quad (3\text{-}8)$$

This expression fits the measured branching ratios.[14,18,22] $P_{exp}(E,J_{KaKc})$ for

$^1CH_2(0,1,0)$ is approximated by a Boltzmann rotational distribution with $T_{rot}(E,^1CH_2(0,1,0))=T_{rot}(E - 1352.5\ cm^{-1}, ^1CH_2\ (0,0,0))$.[18] The total $P_{exp}(E,J_{KaKc})$ for Equation 3-7 is the sum of the Boltzmann rotational distribution for each vibrational state weighted by its vibrational yield. Like PST, CPST contains no adjustable fitting parameters. Calculated distributions are compared to experiment in Figures 5-7.

Neither PST nor CPST adequately describes all of the distributions. PST fits the lowest energy distributions, at 57, 110, and 200 cm^{-1} in Figure 5, just as it describes the $^1CH_2$ distributions and PHOFEX spectra for $E \leq 200$ cm^{-1}.[17] At 357 and 490 cm^{-1}, CPST gives a significantly better fit than PST, Figure 7. For $E \geq 1107$ cm^{-1}, PST overestimates the population of the low J_{CO} states and underestimates the population of higher J_{CO} states and CPST matches the center and overestimates the width of the distributions. Several functional forms for the CO(v=1) rotational distributions were tested for $E \geq$ 490 cm^{-1}. The best fits were provided by Gaussian (two fitting parameters) and Boltzmann (one fitting parameter) distributions, Figure 7. In Figure 5, the solid lines are given by PST at 57, 110, and 200 cm^{-1}, CPST at 357 and 490 cm^{-1}, and by the best Gaussian fit at 1107, 1460, and 1720 cm^{-1}. The best fit Boltzmann rotational temperatures are given in Table 1 along with temperatures derived for the PST and CPST distributions. These temperatures are simply fitting parameters and have no fundamental significance as the distributions are not thermal; in fact, for CPST at energies above 1000 cm^{-1} a rotational temperature completely misrepresents the distribution, Figure 8. Table 1 also compares the average fraction of the total available energy released as CO rotation for these different distributions. The

measured value is 26±1% for the entire range 1720≥E≥357 cm^{-1}.

Doppler-resolved spectra of $^1CH_2$ fragments give the translational energy release distribution. The CO rovibrational distribution paired to an individual $^1CH_2$ state is then derived by energy conservation. Chang *et al.* report measurements on the 4_{14} rotational level for photodissociation of room temperature ketene at 308 nm, or 2351 cm^{-1} over the singlet channel threshold.[23] They were able to fit these Doppler profiles by assuming that the rotational distribution of CO follows PST, or equivalently CPST since only a single rotational state of $^1CH_2$ is considered, with a population of CO(v=1) twice the average given by SSE.[23] Measurements of the vibrational branching ratio summed over all product rotational states give values identical to SSE.[14,18,22] However, the $^1CH_2$ fragments coincident with CO(v=1) are in relatively low-J states compared to those for CO(v=0). Near 308 nm, direct measurements of populations indicate that the rotational distributions of CO, described here, and $^1CH_2$[17,18] are far from PST. Furthermore, CO time-of-flight data, Figures 6-8 of Ref. 19, suggest that for low $^1CH_2$ rotational energies the J_{CO} distribution is skewed to much higher values than for PST. The consequence is smaller velocities than for PST. It might also be possible that some of the fast moving $^1CH_2$ product collides and is thermalized during the 100 ns observation time. The reported fits do not seem to be sufficiently sensitive to the J_{CO} distribution to distiguish between PST and the distributions reported here.

PST calculations may be carried out including a variety of dynamical constraints. One approach is to restrict the range of impact

paramenters, b. This in turn limits the orbital angular momentum quantum number l for a given kinetic energy release, E_{trans},

$$b = ((l(l+1)h^2)/2\mu E_{trans})^{1/2} \quad (3\text{-}9)$$

Garcia-Moreno *et al.* found that methylene rotational distributions could be fit better by setting a maximum impact parameter, b_{max}, constrained to a fraction of an Å.[17] However, the PHOFEX spectra for such impact parameter constraints were displaced to higher energy from PST and completely inconsistent with experiment.[17,24] This method has recently been used by Wodtke and co-workers, who refer to it as RPST, to fit their correlated product state distributions.[19] For $5<J_{CO}<20$, most of the distribution, their data require $b_{max} - b_{min} \sim 0.3$ Å with b_{max} increasing from 0.6 to 1.2 Å as J_{CO} increases from 5 to 20 for $^1CH_2(0,0,0) + CO(v=0)$.[19] These impact parameter ranges are not only inconsistent with PHOFEX data but are also unrealistically small compared to the 2.2-3.1 Å range for the C-C bond length for the variational transition state.[21] The data on rate constant, $^1CH_2$ rotational distributions and CO time of flight show that the photodissociation of ketene is clearly dynamically constrained. However, a simple limitation on the range of impact parameters does not describe that constraint.

SACM is a statistical model based on a physically different set of dynamical constraints. SACM, like variational RRKM, considers the increase in energy level spacing which occurs as the chemical bond forms betwen the approaching fragments.[21] In SACM, adiabatic channel curves are defined by connecting the transition state energy levels smoothly and without crossings to the asymptotic levels of the freely rotating products.[6-8] The reaction rate is defined by the number of channels with energy maxima less than the total

available energy. If the dynamics beyond the maxima were strictly adiabatic repulsion for each channel, only the lowest energy product channels would be observed and each channel would open at an energy well above its asymptotic threshold. Such is not the case for CO or for $^1CH_2$,[17,18,22] and indicates that the dissociation dynamics of ketene from transition state to products are clearly not in this strict adiabatic limit. Nevertheless, the SACM suggests that repulsive energy release may play a significant role in the dynamics.

The simplest impulsive model predicts that the rotational distribution should be a Gaussian centered around an average rotational energy

$$\overline{E}_{rot}(CO) = \frac{m_O}{m_C + m_O} \sin^2 \delta \frac{E_{avl}}{2} \qquad (4\text{-}10)$$

where m_O and m_C are the mass of O and C respectively, E_{avl} is the energy available for rotation of CO and translation, and δ is the angle of the CCO bend at the transition state and beyond.[26] If the bending angle is not a strong function of the excess energy, then the average rotational energy is a constant fraction of the available energy. At 1460 cm^{-1}, 26% of the available energy is converted into CO rotation. This corresponds to $\delta \sim 110°$ if no energy is reserved for $^1CH_2$ rotation. Recent *ab initio* calculations predict the CCO angle at the transition state for the singlet channel to be nearly linear, ~170°.[21] Even allowing for the energy in rotational excitation of $^1CH_2$, impulsive models clearly predict much lower rotational excitation of CO than observed. Even at energies over a few hundred cm^{-1}, where the transition state has tightened, the observed CO roational distribution is not so far from the CPST statistical limit and is dramatically different from the adiabatic limit. The basic dynamics of the SACM may be correct if hops through some

narrowly avoided crossings are permitted. Such hopping will tend to preserve the rovibrational wavefunction of the molecule as it proceeds from transition state to products. Thus, a Franck-Condon model might be appropriate. This limiting model is at the opposite extreme from PST which assumes strong coupling among rotational and translational degrees of freedom beyond the transition state. In this limit, the rotational distribution is given by the overlap integral between the bound and free wavefunctions.[26,27]

$$P(J_{CO}) = |\langle \Psi_{bound} | \Psi_{free} \rangle|^2 \qquad (4\text{-}11)$$

where J_{CO} is the rotational quantum number of the product species. This method has been used successfully to calculate rotational distributions by Houston and co-workers for HCO[28] and for Reisler and co-workers for NO_2.[27] For a triatomic, the bending and stretching vibrations of the parent are assumed to be uncoupled, and the free wavefunctions are given by the spherical harmonics. If parent rotation is not considered and the bending vibration is approximated as a harmonic oscillator,[26]

$$P_n(J_{CO}) \mu \sin^2[(J_{CO}+1/2)\,\delta + (-1)^n(\pi/4)]H_n^2[\alpha'(J_{CO}+1/2)]$$

$$x \exp[-\alpha'^2 (J_{CO}+1/2)^2] \qquad (4\text{-}12)$$

where n is the number of quanta in the bending mode, $H_n[x]$ are the Hermite polynomials, δ is the equilibrium bend angle, and α' is a function of the molecular geometry and the bending frequency.[26,27] This model has been applied to ketene, treating CH_2 as an atom, and considering only the CCO bend at the transition state, taken from a recent *ab initio* analysis by Klippenstein, East, and Allen.[21] The distributions were averaged over the possible vibrational states of the bending vibration at the transition state, using the

variational RRKM sum of states for the 3N-7 modes at the transition state of Ref. 21. Since the CCO angle is close to 180°, those vibrational distributions were calculated in two ways, treating the CCO bend as a degenerate or non-degenerate bend. When the bend was assumed to be degenerate, the population at that vibration was multiplied by the degeneracy factor of n+1 and both degenerate bends are considered. Since these assumptions only affected the weighting of the vibrations and not the overall shape of each vibration's rotational distribution, the two distributions were quite similar. The results of this calculation, assuming a non-degenerate bend, are compared with experiment in Figure 9. This model predicts large oscillations in population with J_{CO} such as have been observed in HCO[28] and NO_2[27] but are not present in ketene distributions. Inclusion of the $^1CH_2$ degrees of freedom, averaging over initial ketene states, and other refinements will reduce or possibly even eliminate these oscillations. The smoothed result is qualitatively similar to the data.

The release of energy to rotation in singlet channel ketene fragmentation is completely statistical for energies up to 200 cm^{-1} above threshold. As energy increases above 200 cm^{-1}, $^1CH_2$ departs from the strongly coupled limit and receives progressively less than its statistical share of energy as total energy increases. CO continues be statistically distributed among its rotational states to energies 500 cm^{-1} and possibly approaching 1000 cm^{-1} above threshold. That CO should remain statistical to higher energies than $^1CH_2$ may be understood in terms of the smaller energy level spacings for CO and the consequently smaller rotation-translation couplings required for energy randomization. Above this energy, the average rotational

energy and average J_{CO} are still predicted correctly by CPST, Table 1, but the distributions are narrower than statistical. Hence, the dynamics for CO are close to the strongly coupled statistical limit but modestly constrained to populate a narrower range of quantum states while the dynamics for $^1CH_2$ are far from statistical. None of the simple dynamical models discussed to date provide a satisfactory quantitative picture of the dynamics from threshold to a few thousand cm^{-1} above threshold.

Table I: Comparison of Experiment and Constrained PST

E_{exc}[a] (cm^{-1})	T_{rot} (K)			$\bar{E}_{rot}/E_{exc}$ (%)	
	Expt.	PST	CPST	Expt.	CPST
57	34 ± 6	41	41	32 ± 3	31.7
200	88 ± 9	83	83	27 ± 2	27.1
357	167 ± 17	135	162	26.0 ± 0.7	27.0
490	227 ± 23	198	224	26.0 ± 0.7	27.0
1107	602 ± 60	407	--[b]	26.0 ± 0.7	26.8
1460	730 ± 73	521	--[b]	26.6 ± 0.7	26.2
1720	817 ± 82	589	--[b]	25.9 ± 0.7	25.0

a. E_{exc} is the energy above the dissociation threshold, $E\text{-}D_0$.

b. At these energies, constrained PST cannot be fit to a Boltzmann plot. See Figure 11.

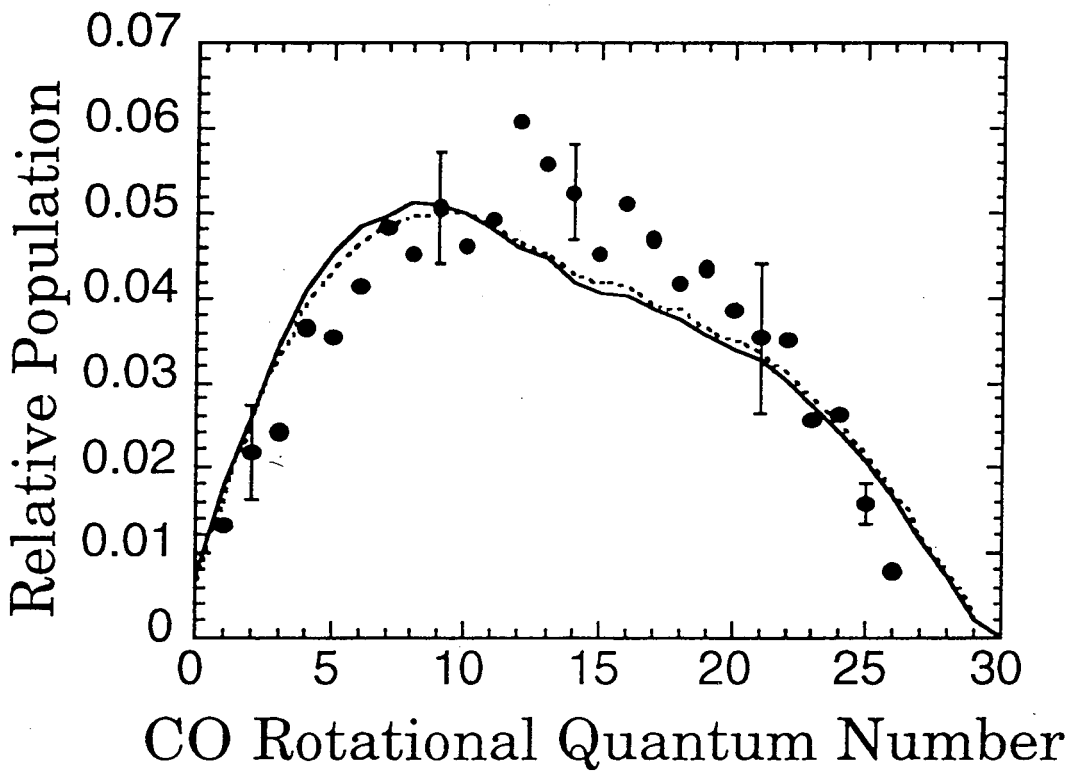

Figure 6. Comparison of two constrained PST predictions at 1720 cm^{-1} based on different models of the $^1CH_2$ distributions. The closed circles are the experimental points, with sample 1σ error bars given. The solid line is the resultant distribution when the $^1CH_2$ rotational population is approximated by the Boltzmann distribution which best fits the data (Ref. 17). The population is cut to zero sharply for any $^1CH_2$ state whose term value is greater than the available energy. The dotted line is the resultant distribution when that Boltzmann distribution is adjusted to cut off sharply in a similar way any state whose term value is greater than 80% of the available energy.

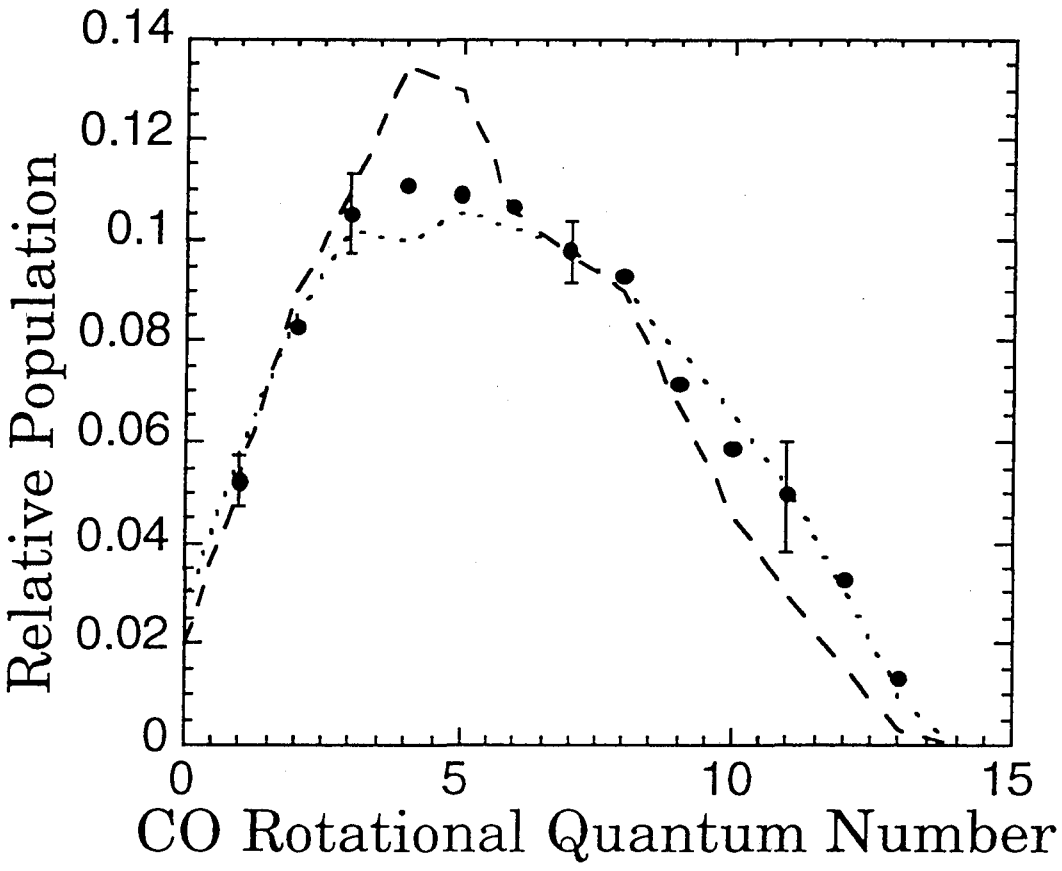

Figure 7a. Comparison of experiment, PST, and constrained PST at 357 cm^{-1} above the singlet threshold for production of CO(v=1). The solid circles are the experimental points. Sample 1σ error bars are given. The dashed line is PST and the dotted line is constrained PST. At 357 cm^{-1}, constrained PST provides the better fit.

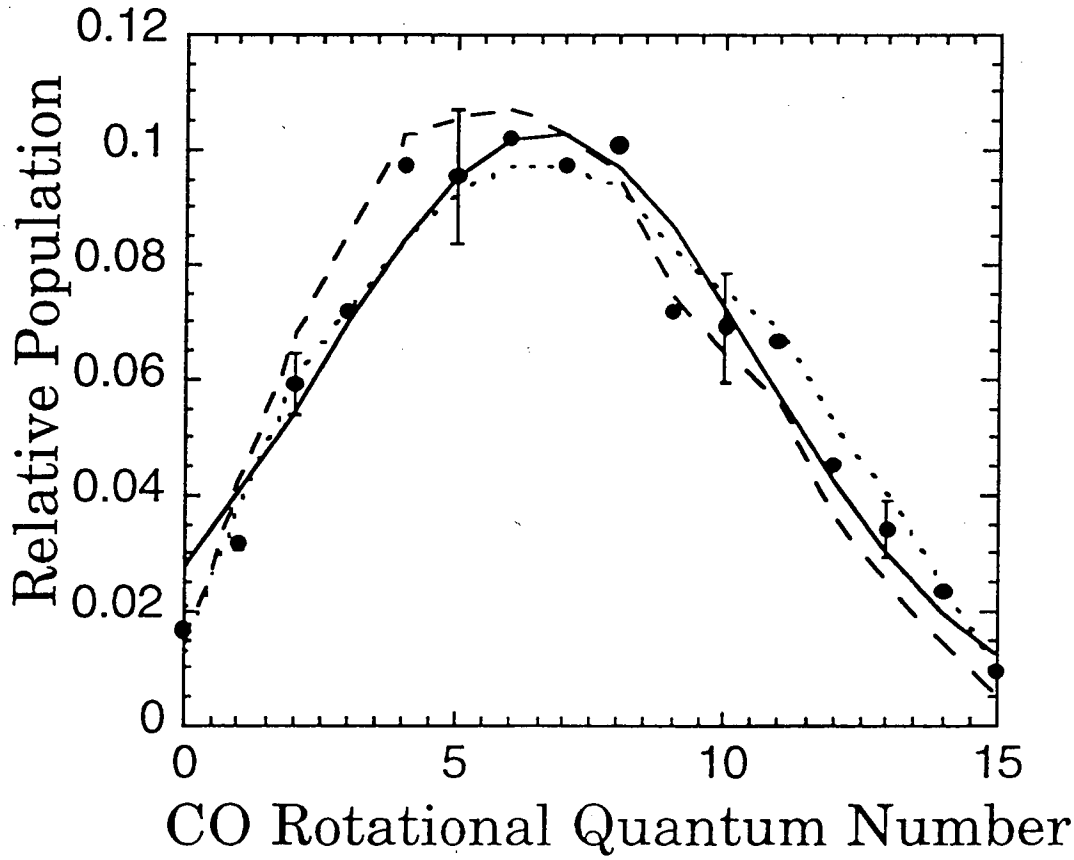

Figure 7b. Comparison of experiment, PST, and constrained PST at 490 cm^{-1} above the singlet threshold for production of CO(v=1). The solid circles are the experimental points. Sample 1σ error bars are given. The dashed line is PST, the dotted line is constrained PST, and the solid line is the best Gaussian fit to the data. At 490 cm^{-1}, constrained PST provides the better fit.

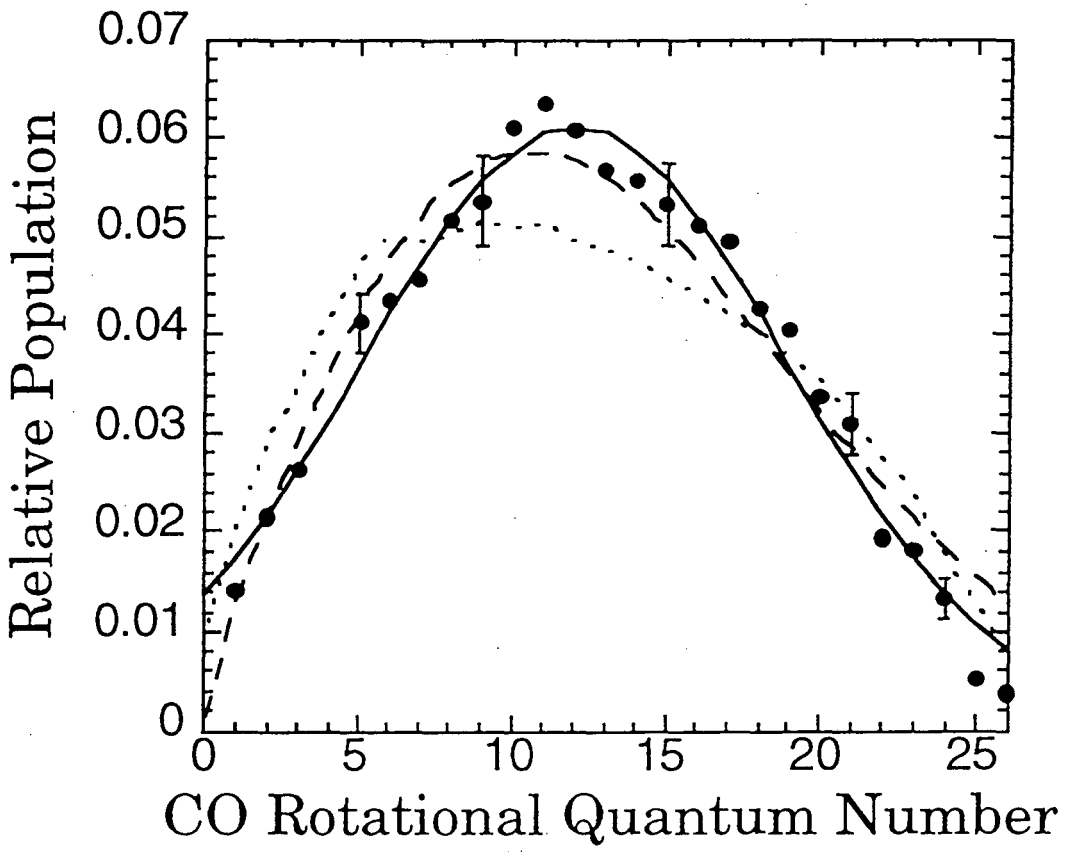

Figure 7c. Comparison of experiment, constrained PST, and the Gaussian fit at 1460 cm^{-1} above the singlet threshold for production of CO(v=1). The solid circles are the experimental points. Sample 1σ error bars are given. The dotted line is constrained PST, the solid line is the best Gaussian fit, and the dashed line is the Boltzmann fit. The PST fit is not shown. At 1460 cm^{-1}, the best fit is given by the Gaussian.

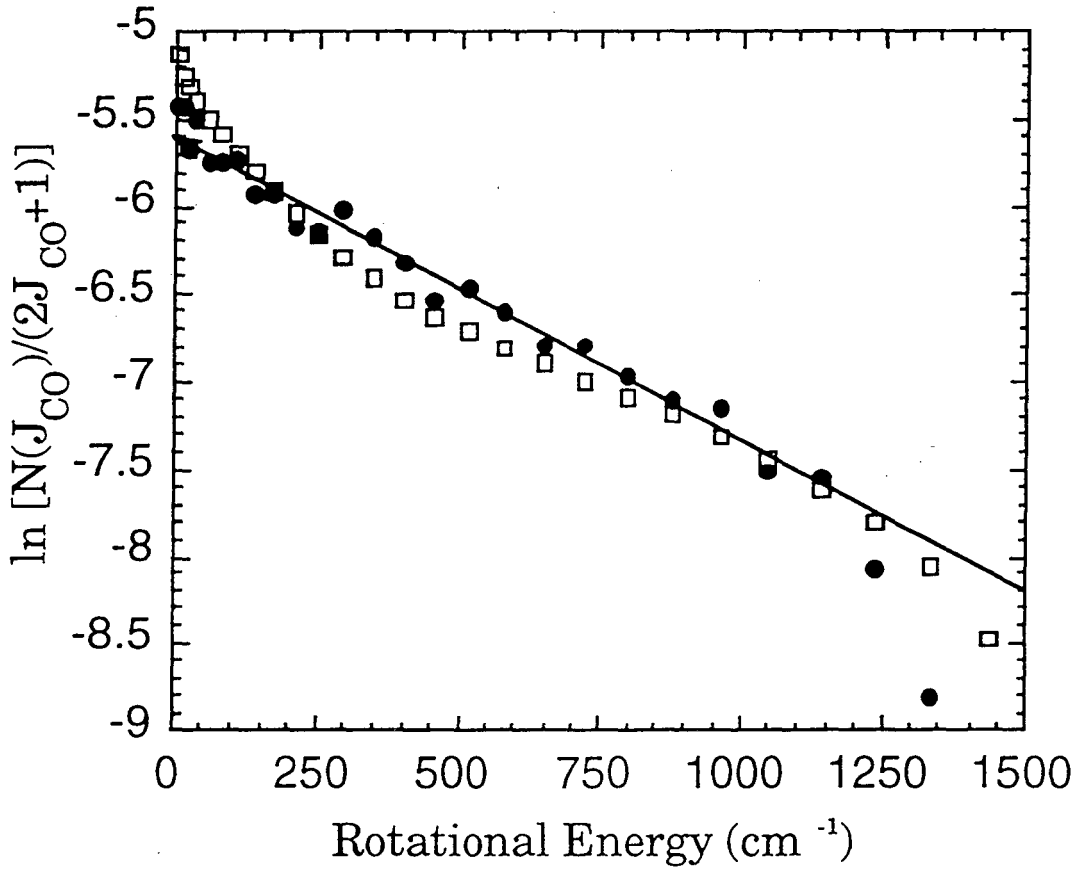

Figure 8. Boltzmann plots at 1460 cm-1. The solid circles are the experimental distribution and the open squares are the constrained PST distribution. The solid line is the Boltzmann fit to the experimental distribution. While the downward curve at high energy is typical of a PST-like distribution, which does not continue out to infinite energy, the initial curve is not. For the constrained PST, this initial curve makes it impossible to determine a meaningful slope, which is necessary to determine a meaningful temperature.

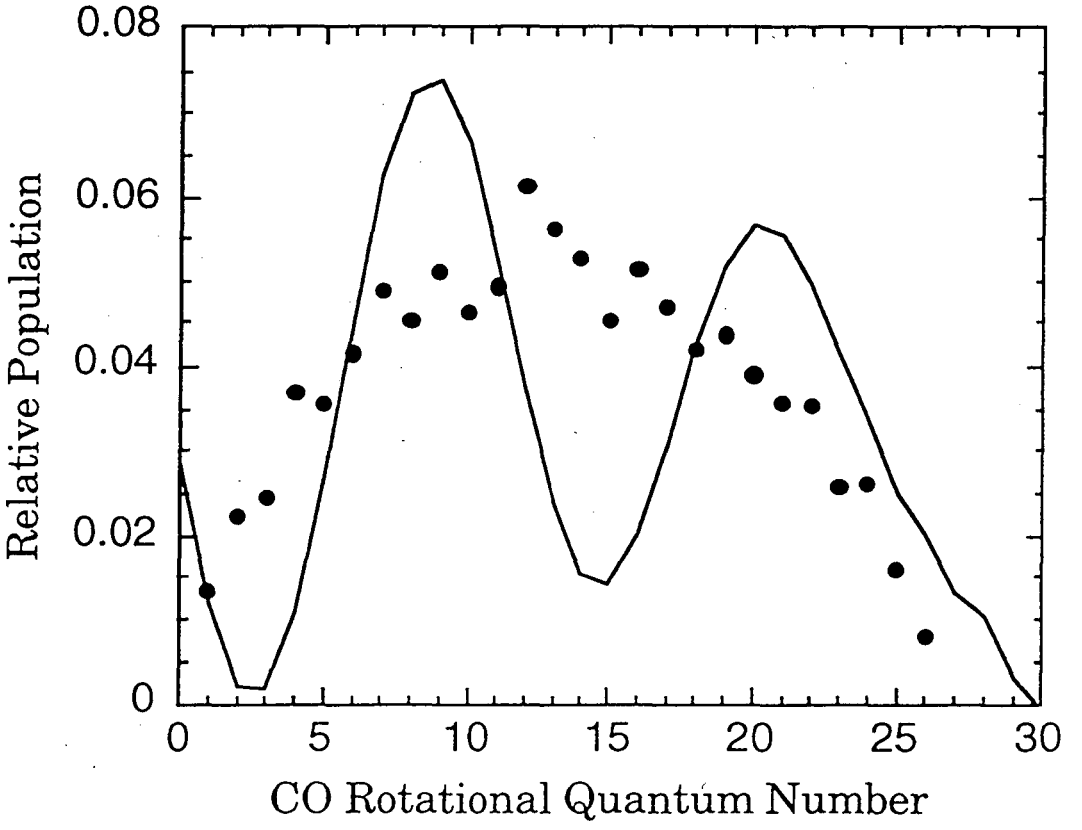

Figure 9. Comparison of experiment and Franck-Condon mapping at 1720 cm^{-1} above the singlet threshold for production of CO(v=1). The solid circles are the experimental points, and the solid line is the distribution produced by Franck-Condon mapping.

IV. Singlet Yield

As the CO(v=1) rotational distributions for excess energies ≥ 357 cm^{-1} contain no discernible contribution from the triplet channel, they can be used to partition the previously determined CO(v=0) rotational distributions[14] into singlet and triplet contributions. Below 200 cm^{-1}, where PST adequately models both the CO(v=0) and the CO(v=1) rotational distributions, the singlet yield is calculated accurately by Kim et al.[14] The singlet part of the distribution is modeled by PST, while the triplet part is approximated by a single Gaussian. Above 200 cm^{-1}, the experimental CO(v=1) distributions are assumed, in the present calculation, to be identical to the singlet part of the CO(v=0) distributions taken from Ref. 14. The singlet yield is calculated in two ways, neither of which perfectly fits the ground state rotational distributions.

First, the singlet yield was calculated by matching the height of the CO(v=1) distribution to the peak of the singlet part of the CO(v=0) distribution. This gives an upper limit, since the contribution of the triplet channel to the population of the J_{CO} at the peak of the singlet channel distribution is ignored. To try to incorporate this contribution, the triplet was modeled, as by Kim et al.,[14] as a single Gaussian centered at J_{CO} =18 with a width of 11.4. This model describes the high-J_{CO} populations, which are completely due to the triplet, but overestimates the triplet where it overlaps the singlet. This approach thus gives a lower limit for the singlet yield. An example of these estimates is given in Figures 10 and 11. It was not possible to fit the CO(v=0) rotational distribution perfectly by varying the singlet-triplet branching ratio. This is probably because the triplet rotational distribution is not really a single Gaussian, Figure 5. However, there is no solid basis for choosing a more complex form at the energies considered here. At 1107 cm^{-1}, it was necessary

to incorporate another Gaussian, centered at J_{CO} =7 with a width of 10, in order to account for low-J_{CO} population due to CO associated with vibrationally excited $^3CH_2$. From 357 to 1107 cm^{-1}, the upper and lower limits differ by no more than 0.1, except at 490 cm^{-1}, where they differ by 0.15. This large difference is due to the difference in energy over threshold, 425 and 490 cm^{-1}, at which the CO(v=0) and CO(v=1) distributions, respectively, were measured. While the CO(v=1) distributions were not all collected at exactly the same energies as the CO(v=0) distributions, the energy difference was typically no more than 10%. (See Table 2)

At 1460 and 1720 cm^{-1}, there is no clear difference between the observed CO(v=0) and CO(v=1) rotational distributions (see Figure 12) so a singlet yield of unity is consistent with the data. While some high-J_{CO} points are observed in CO(v=0) that were not detected for CO(v=1), if it is assumed that these high-J_{CO} states contain all of the triplet population at that energy, the resultant triplet yield is so low that the corresponding triplet rate constant decreases with increasing energy, which seems unlikely. Thus, for higher energies, two limiting models are used to extrapolate the triplet rate constant to 6000 cm^{-1} (see Figure 13) and calculate the singlet yields implied.

In the lower limit case, the triplet rate constant is assumed to be constant above 1107 cm^{-1}, so that

$$k_t(E>1107) = k_t(1107) \qquad (13)$$

Since the total rate constants in this energy region have been determined by Zewail and co-workers,[29] this approximated triplet rate constant allows for the calculation of a singlet rate constant,

$$k_s(E>1107) = k_{tot}(E>1107) - k_t(1107) \qquad (14)$$

As this method underestimates the triplet and so overestimates the singlet, another method was used to give a lower limit for the singlet yield.

The upper limit for k_t was calculated by extrapolating from the known triplet rate constants. The triplet rate constants below the singlet threshold have been determined by Chen *et al.*[30] Additionally, triplet rate constants were calculated from the total rate constants[29] and the experimental singlet yields at 490 and 1107 cm^{-1} (450 and 1107 cm^{-1} in Ref. 29),

$$k_t(E) = (1 - \phi_s(E))\, k_{tot}(E) \qquad (15)$$

where $\phi_s(E)$ is the singlet yield at that energy. The two triplet rate constants closest in energy below the singlet threshold and the first two above were least-squares to a linear log k_t vs. E function. Since the slope of the data actually decreases as energy increases, the linear extrapolation overestimates the true rate constants and underestimates the singlet yield. The extrapolated triplet rate constants are shown in Figure 13.

The singlet yield is shown in Figure 14 and compared to that calculated by Kim *et al.*[14] The upper and lower limits are given in Table 2. The singlet yield rises more quickly, and to a higher value than previously predicted. The upper limit of the current and previous results is supported by the more direct determination of 0.94±.02 for 308 nm photolysis obtained by Wodtke and co-workers.[19] The singlet yields will be used in a later publication to determine the singlet rate constant.[22]

Table II: Singlet Yield

E_{exc}[a] (cm^{-1})	Singlet Yield		
	Ref. 14[b]	lower	upper
57 (56)[c]	0.15 ± 0.03	0.12	0.18
110 (110)[c]	0.34 ± 0.03	0.31	0.37
357 (325)	0.60 ± 0.06	0.60	0.67
490 (425)	0.62 ± 0.06	0.63	0.78
1107 (1107)	0.65 ± 0.10	0.75	0.85
1435	0.70 ± 0.08	0.85	0.88
1720	0.80 ± 0.10	0.86	0.90
2521	0.75 ± 0.20	0.88	0.95
2942		0.88	0.96
3217		0.87	0.97
3538		0.88	0.97
3763		0.85	0.97
4367		0.89	0.99
4870		0.88	0.99
4920		0.88	0.99
5598		0.85	0.99

a. The value in parentheses is the excess energy for the CO(v=0) distribution taken from Ref. 14, while the other value is for the CO(v=1) distribution. Above 1107 cm^{-1}, the singlet yield is approximated from the total rate constants given in Ref. 29 and the extrapolated triplet rate constants (Figure 13), and the energy is that at which the total rate constant was measured.

b. No singlet yield was calculated above 2500 cm^{-1}.

c. At 57 and 110 cm^{-1}, the distribution is described by PST, so the yield is calculated as in Ref. 14.

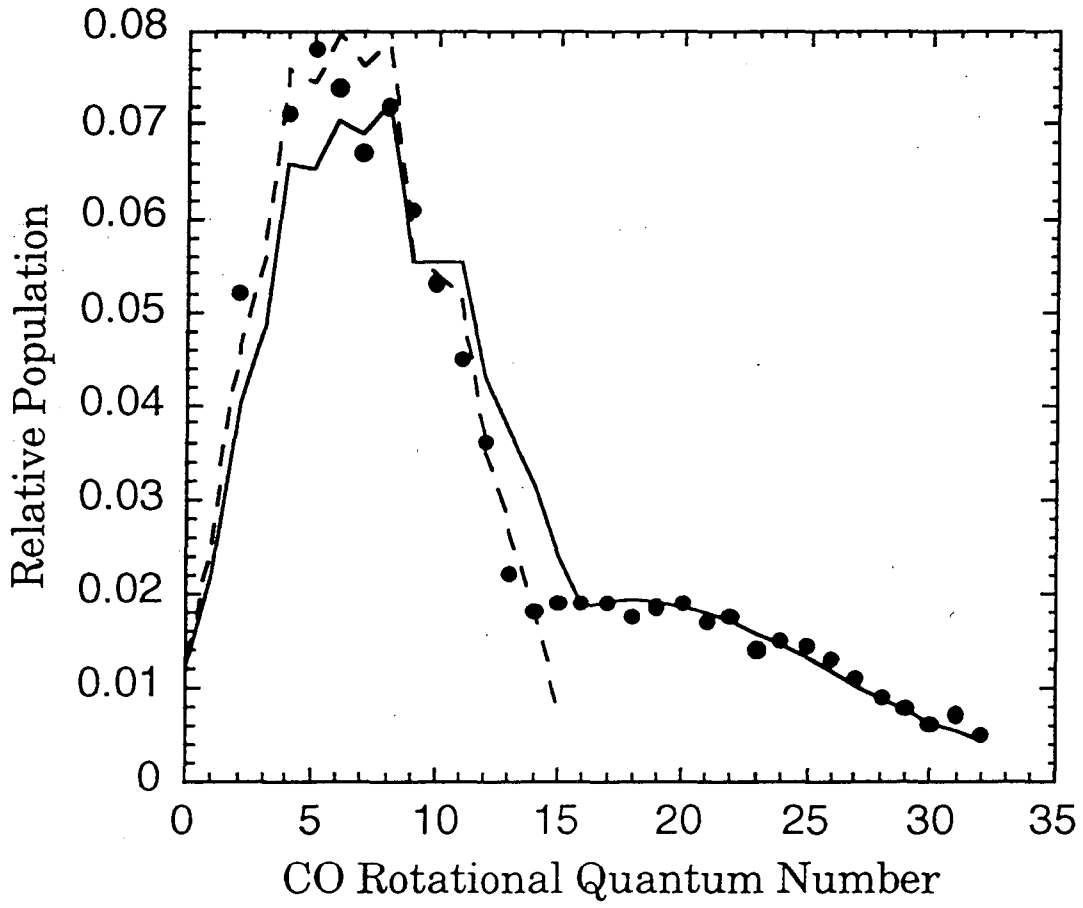

Figure 10. The CO(v=0) and CO(v=1) rotational distributions, at 425 and 490 cm-1 over the respective thresholds, are used to calculate the upper and lower limits on the singlet yield. The solid circles are the CO(v=0) experimental distribution. The dashed line is the upper limit, given by the CO(v=1) distribution times a scaling factor of 0.78. The solid line is the lower limit, which is the weighted sum of the CO(v=1) distribution and a Gaussian centered at J=18 with a width of 11.4 which is used to approximate the triplet channel CO. This gives a singlet yield of 0.63.

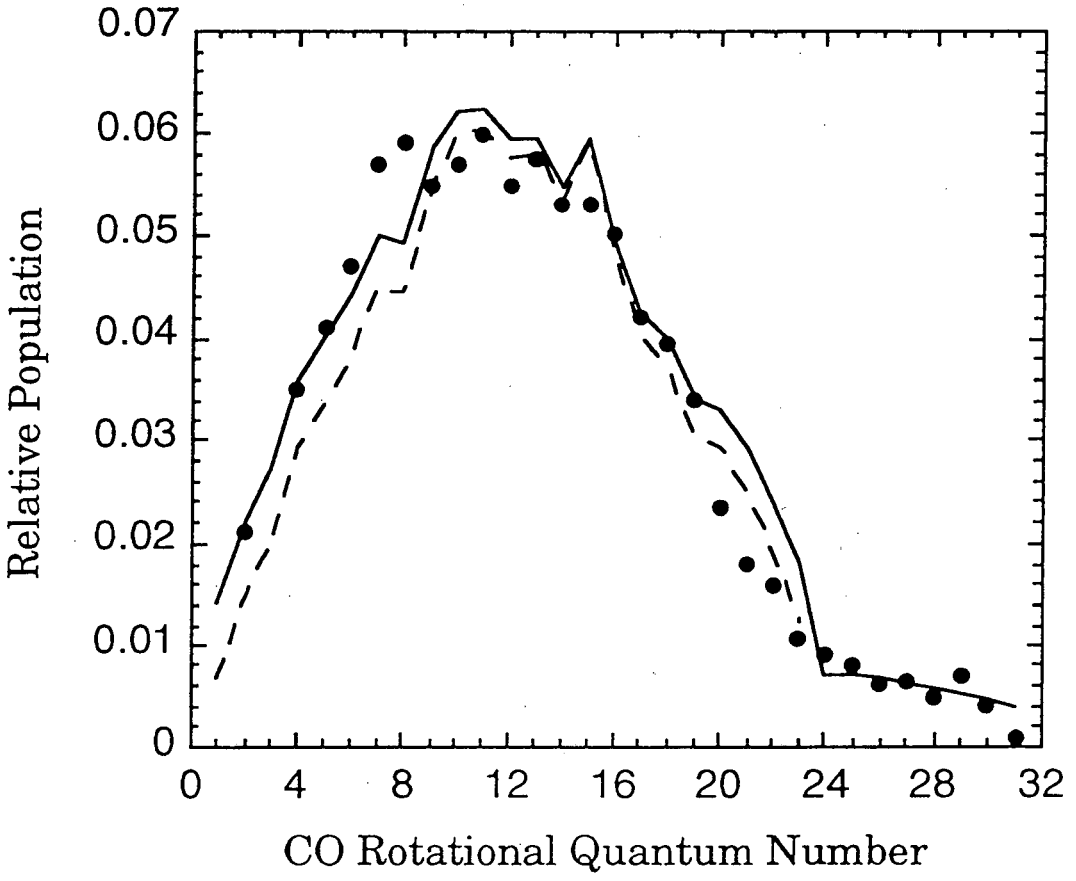

Figure 11. The CO(v=0) and CO(v=1) rotational distributions, at 1107 cm^{-1} over the respective thresholds, are used to calculate the upper and lower limits on the singlet yield. The solid circles are the CO(v=0) experimental distribution. The dashed line is the upper limit, given by the CO(v=1) distribution times a scaling factor of 0.85. The solid line is the lower limit, which is the weighted sum of the CO(v=1) distribution and two Gaussians centered at J=7 and 18 with widths of 10 and 11.4, respectively, which are used to approximate the CO from the triplet channel. This gives a singlet yield of 0.75.

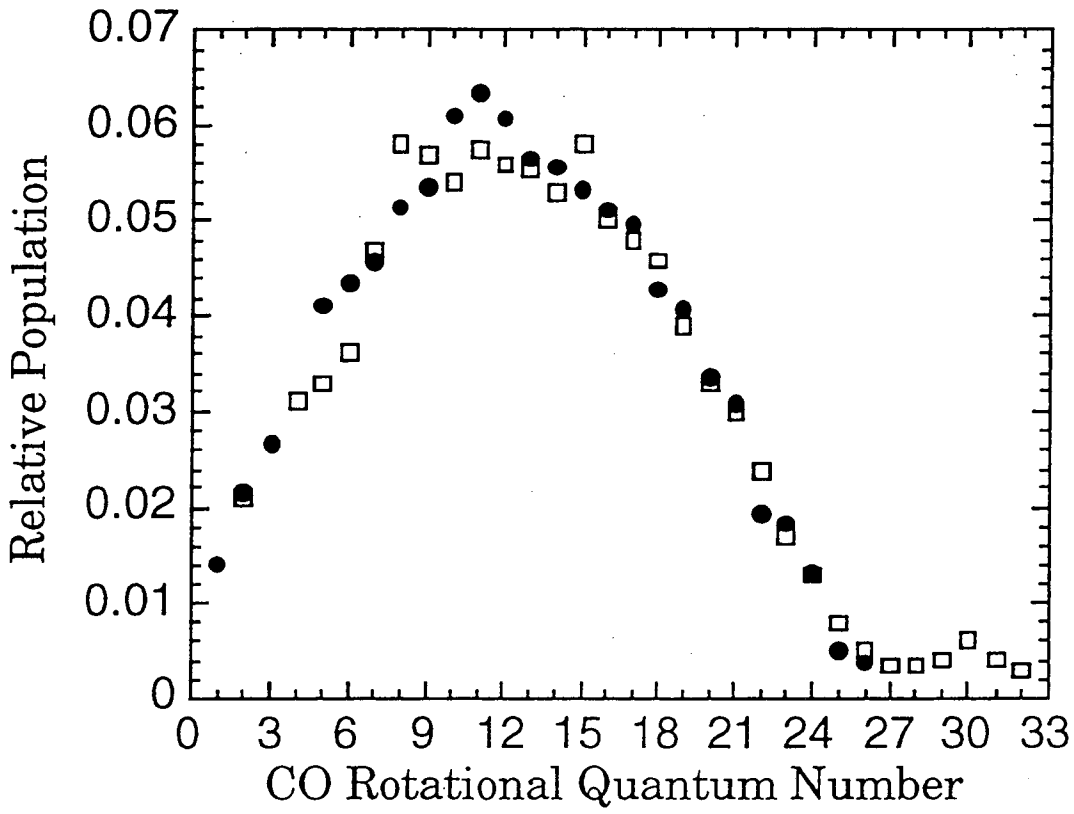

Figure 12. The CO(v=0) and CO(v=1) rotational distributions, at 1435 and 1460 cm^{-1} over the respective thresholds. The open squares are the CO(v=0) distribution and the solid circles are the CO(v=1) distribution. There is essentially no difference between the distributions.

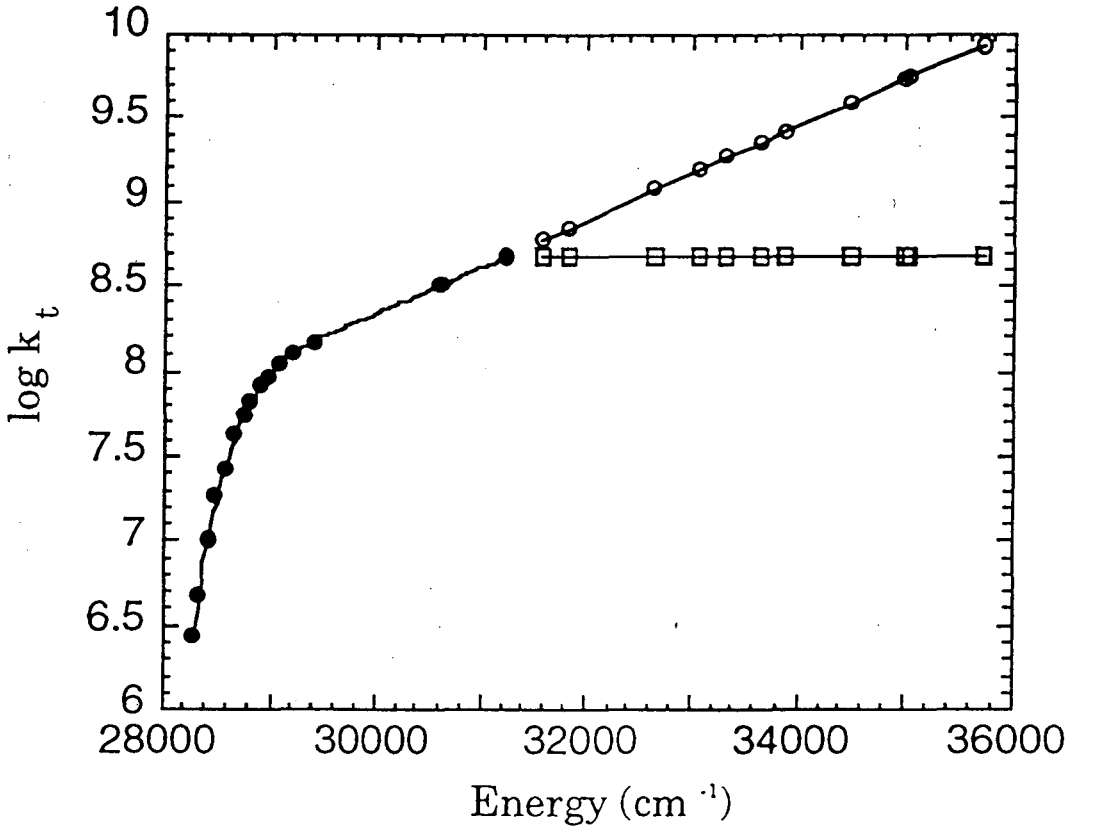

Figure 13. The triplet rate constant as a function of energy. The solid circles below the singlet threshold at 30116.2 cm^{-1} are the data of Ref. 30. The solid circles above the singlet threshold are calculated from the total rate constant (Ref. 29) and the singlet yield. The open circles and open squares are the approximated upper and lower limit triplet rate constants described in the text.

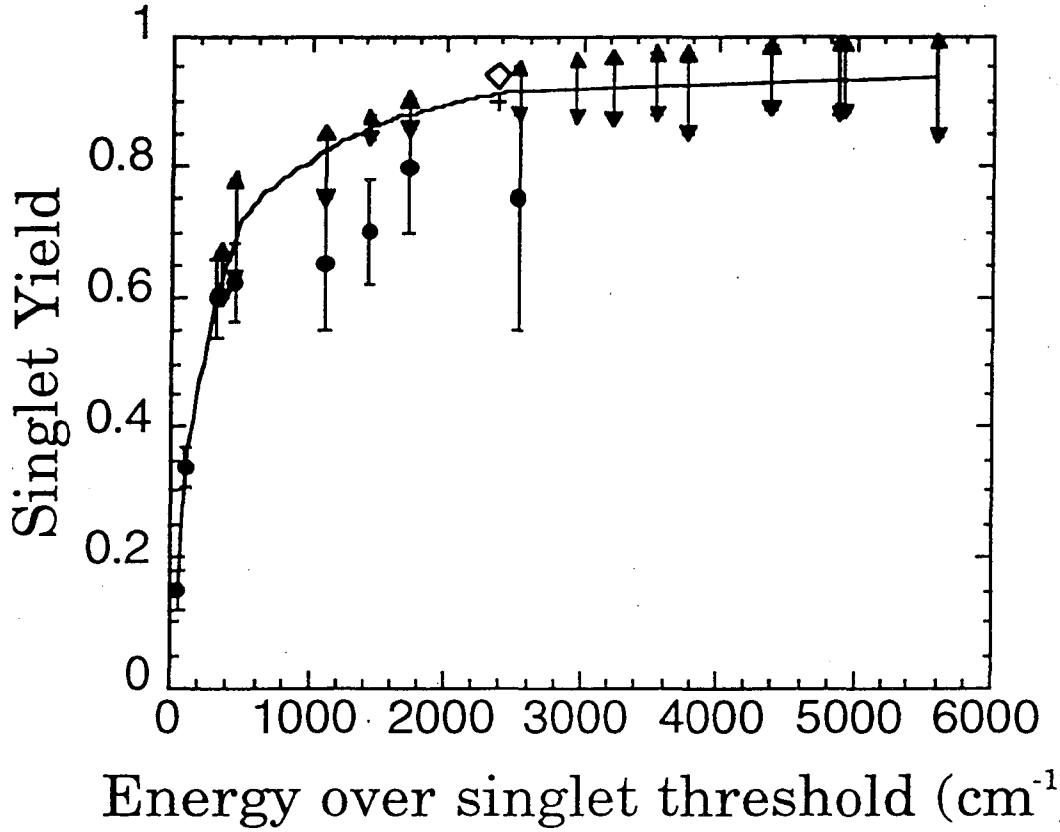

Figure 14. The singlet yield as a function of excess energy. The upper and lower limits calculated here are given by the triangles at either end of the error bars. The solid line is a smooth interpolation given to guide the eye. The solid circles are the earlier estimates of Kim et al. (Ref. 14) The "+" is the lower limit at 308 nm determined by Hayden et al. (Ref. 20) The "◊" is the value measured from the correlated-product-state distributions at 308 nm by Wodtke and co-workers. (Ref. 19)

V. References

1. R.G. Gilbert and S.C. Smith, *Theory of Unimolecular and Recombination Reactions*; (Oxford, Blackwell Scientific, 1990).
2. H. Reisler and C. Wittig, *Annu. Rev. Phys. Chem.* **37**, 307 (1986).
3. W.H. Green, C.B. Moore, and W.F. Polik, *Annu. Rev. Phys. Chem.* **43**, 59 (1992); C.B. Moore, and I.W.M. Smith, *J. Phys. Chem.* **100**, (1996) in press.
4. T. Baer and W.L. Hase, *Unimolecular Reaction Dynamics: Theory and Experiments*, (Oxford, Oxford University Press, 1996).
5. P. Pechukas, and J.C. Light, *J. Chem. Phys.* **42**, 3281 (1965); P. Pechukas, C. Rankin, and J.C. Light, *J. Chem. Phys.* **44**, 794 (1965).
6. M. Quack, and J. Troe, *Ber. Bunsenges. Phys. Chem.*. **78**, 240 (1974).
7. M. Quack, and J. Troe,*Ber. Bunsenges. Phys. Chem.*. **79**, 170 (1975); **79**, 469 (1975).
8. J. Troe, *J. Chem. Phys.* **75**, 226 (1981); **79**, 6017 (1983).
9. C. Wittig, I. Nadler, H. Reisler, J. Catanzarite, and G. Radhakrishnan, *J. Chem. Phys.* **83**, 5581 (1985).
10. R.A. Marcus, *J. Chem. Phys.* **85**, 5035 (1986); *Chem. Phys. Lett.* **144**, 208 (1988); D.M. Wardlaw and R.A. Marcus, *Adv. Chem. Phys.* **70**, 231 (1988).
11. S.J. Klippenstein, and R.A. Marcus, *J. Chem. Phys.* **91**, 2280 (1989); **93**, 2418 (1990).
12. J. Yu, and S.J. Klippenstein, *J. Phys. Chem.* **95**, 9332 (1991).
13. I. Nadler, M. Noble, H. Reisler, and C. Wittig, *J. Chem. Phys.* **82**, 2608 (1985).
14. S.K. Kim, Y.S. Choi, C.D. Pibel, Q.-K. Zheng, and C.B. Moore, *J. Chem. Phys.* **94**, 1954 (1991).
15. S.A. Reid and H. Reisler, *J. Phys. Chem.* **100**, 474 (1996).

16. T.M. Ticich, T.R. Rizzo, H.-R. Dübal, and F.F. Crim, *J. Chem. Phys.* **84**, 1508 (1986).
17. I. Garcia-Moreno, E.R. Lovejoy, and C.B. Moore, *J. Chem. Phys.* **100**, 8890 (1994).
18. I. Garcia-Moreno, E.R. Lovejoy, and C.B. Moore, *J. Chem. Phys.* **100**, 8904 (1994).
19. C.G. Morgan, M. Drabbels, and A.M. Wodtke, *J. Chem. Phys.* **104**, 7460 (1996); M. Drabbels, C.G. Morgan, D.S. McGuire, and A.M. Wodtke, *J. Chem. Phys.* **102**, 611 (1995).
20. C.C. Hayden, D.M. Neumark, K. Shobatake, R.K. Sparks, and Y.T. Lee, *J. Chem. Phys.* **76**, 3607 (1982).
21. S.J. Klippenstein, A.L.L. East, and W.D. Allen, *J. Chem. Phys.* **105**, 118 (1996).
22. E.A. Wade, A. Mellinger, and C.B. Moore, *J. Chem. Phys.* submitted.
23. B.-C. Chang, M. Wu, G.E. Hall, and T.J. Sears, *J. Chem. Phys.* **101**, 9236 (1994).
24. W.H. Green, I.-C. Chen, and C.B. Moore, *Ber. Bunsenges. Phys. Chem.* **92**, 389 (1988); I.-C. Chen, W.H. Green, and C.B. Moore, *J. Chem. Phys.* **89**, 314 (1988).
25. I.-C. Chen and C.B. Moore, *J. Chem. Phys.* **94**, 269 (1990).
26. M.D. Morse and K.F. Freed, *Chem. Phys. Lett.* **74**, 49 (1980).
27. C.X.W. Qian, A. Ogai, J. Brandon, Y.Y. Bai, and H. Reisler, H. *J. Phys. Chem.* **95**, 6763 (1991).
28. D.W. Neyer, X. Luo, I. Burak, and P.L. Houston, *J. Chem. Phys.* **102**, 1645 (1995); D.W. Neyer, X. Luo, P.L. Houston, and I. Burak, *J. Chem. Phys.* **98**, 5095 (1993).
29. E.D. Potter, M. Gruebele, L.R. Khundkar, and A.H. Zewail, *Chem. Phys. Lett.* **164**, 463 (1989).
30. I.-C. Chen and C.B. Moore, *J. Chem. Phys.* **94**, 263 (1990).

Chapter 4. Vibrational Adiabaticity and the Tightening Transition State in the Photodissociation of Singlet Ketene

I. Introduction

In unimolecular reactions controlled by a transition state at the top of a barrier between reactant and products, Rice-Ramsperger-Kassel-Marcus (RRKM) theory can provide quantitative predictions of the rate.[1-5] In the absence of a barrier to recombination, it is significantly more difficult to define and locate a transition state on the potential energy surface (PES) for the reaction. At the energetic threshold for unimolecular reactions without a barrier to recombination, the rate is limited only by the number of available product states, the phase space theory (PST) limit.[6-8] The sum of states or open reaction channels, W, in the statistical rate theory expression for the rate constant

$$k(E,J) = W(E,J)/h\rho(E,J) \qquad (4\text{-}1)$$

is easily calculated from the energy levels of the products, where E is the total energy and J is the total angular momentum quantum number of the reactant molecule prior to dissociation. The density of states, $\rho(E,J)$, is estimated from the spectroscopy of the stable molecule[1] or directly measured spectroscopically.[3,8,9] Exactly at threshold, there is only one energetically accessible channel, and PST must, by definition, provide the correct statistical rate constant. The product energy state distributions for NCNO[10,11] and CH_2CO,[7,12-16] and indirect measurements of rate constants for CH_2CO[17] and NO_2[8,9] are consistent with PST predictions near the energetic threshold.

As fragments approach each other along the reaction coordinate, a

bond begins to form, rotations become hindered, and energy level spacings increase. As total energy increases, the number of open channels W(E,J) has its minimum value at steadily smaller values of the reaction coordinate, R, as shown in Figure 1. In variational RRKM (var. RRKM) theory,[18-23] the rate constant is calculated by finding this minimum value of W(E,J) and the corresponding location of the transition state along the reaction coordinate, $R^{\ddagger}(E,J)$. In the statistical adiabatic channel model (SACM),[24,25] the energy states are correlated to define adiabatic channel potentials along R. A channel is counted in W(E,J) if its maximum along R is below E. The positions of the adiabatic channel maxima define a transition state region. In both var. RRKM and SACM, the position of the transition state moves inward along the reaction coordinate with increasing energy. These two models are identical to PST at threshold and give rate constants which increase much less rapidly with energy than do PST rate constants. Additionally, while SACM and var. RRKM are based on different physical models, they give identical rate constants, as long as the adiabatic channel curves do not cross.[3]

Product vibrational degrees of freedom do appear to evolve adiabatically from transition state to products.[3-5,13,15,17,20] Product vibrational distributions can be understood quantitatively in terms of a model in which the transition state is defined separately for vibrationally adiabatic potentials leading to each combination of vibrational states of the fragments. Vibrational branching ratios are seriously underestimated by PST since the transition state for the vibrational ground state products is much tighter than that for vibrationally excited products, Figure 1. Var. RRKM calculations[20] predict the experimental branching ratios quantitatively with this vibrationally adiabatic model for both $^1CH_2$[15] and

CO[17] produced via photodissociation of ketene.

The photodissociation of ketene provides a good test case for unimolecular reaction models. Ketene is excited by a UV pulse using a transition whose oscillator strength is derived from electronic excitation to the first excited state, S_1. Internal conversion to S_0 and intersystem crossing to T_1 provide strong coupling to these two potential energy surfaces from which dissociation occurs. Dissociation along the S_0 surface produces $CH_2(\tilde{a}\ ^1A_1) + CO(\tilde{X}\ ^1\Sigma^+)$ ($^1CH_2$ + CO). There is no barrier to dissociation along this surface and there is only one surface leading to these singlet products.[3]

Indirect measurements[17] and var. RRKM calculations[22,23] of the singlet channel rate constant have suggested that the transition state is loose (PST) up to about 100 cm^{-1} over threshold. Above 100 cm^{-1}, the experimental rate constant rises less rapidly than predicted by PST, which indicates that the transition state is tightening, consistent with var. RRKM and SACM.[19,26] However, the energy at which the transition state begins to tighten was not clearly established. For the dissociation of NO_2, *ab initio* calculations indicate that the transition state tightens within the first 10 cm^{-1} above threshold.[27]

If the dissociation of ketene to singlet products proceeds strictly along single non-crossing adiabatic channel potential curves to fragments, then the production threshold for a given state would be shifted from the product energetic threshold up to the barrier height of the specific adiabatic channel. However, in photofragment excitation (PHOFEX) spectra, each product rotational state is detected at its energetic threshold.[7,13,14] This indicates that the dynamics between the transition state region and products do not

proceed along non-crossing adiabatic channels.

The primary goal of this work is to observe how the transition state for the singlet channel photodissociation of ketene tightens above threshold. Measurements of vibrational branching ratios and PHOFEX spectra for CO(v=1) are combined with the previously determined singlet yield[16] and total rate constants[26] for ketene photodissociation in order to determine the rate constant for singlet ketene dissociation to CO(v=1) as a function of energy near its threshold. By observing where this experimental rate constant becomes smaller than the PST rate constant, the energy at which the transition state begins to tighten can be determined. Additionally, the measured vibrational branching ratios and PHOFEX spectra are compared with theory, including PST, var. RRKM, and separate statistical ensembles (SSE).[11]

II. Results

A. Vibrational Branching Ratios

For photon energies 57, 110, 200, 357, and 490 cm^{-1} over the CO(v=1) threshold (2200, 2253, 2343, 2500, and 2633 cm^{-1} over singlet threshold), vibrational branching ratios were measured, Table III and Figure 15. These ratios are an average over the thermally (4K) populated states of ketene, since they are based on the experimental signal.

$$\frac{\overline{P}(1\,|\,s)}{\overline{P}(0\,|\,s)} \equiv \frac{S_s(h\nu, v=1)}{S_s(h\nu, v=0)} \quad (4\text{-}2)$$

A vibrational branching ratio can also be obtained for the triplet channel in this energy region.

$$\frac{\overline{P}(1\,|\,t)}{\overline{P}(0\,|\,t)} \equiv \frac{\overline{P}(1\,|\,s)}{\overline{P}(0\,|\,s)} \left\{\frac{S_t(h\nu, v=1)}{S_s(h\nu, v=1)}\right\} \left\{\frac{S_s(h\nu, v=0)}{S_t(h\nu, v=0)}\right\} \quad (4\text{-}3)$$

Here the bracketed ratios are the measured ratio of triplet signal intensity to singlet signal intensity in the rotational distributions given in Ref. 16, in Table II and Sec. III of that work. Values of $\overline{P}(1\,|\,t)/\overline{P}(0\,|\,t)$ are given in Table IV.

Table III. Vibrational Branching Ratios for Singlet Product Channel.

Excess Energy (cm-1)[a]	$\bar{P}(1\mid s)/\bar{P}(0\mid s)$					
	Experimental[b]	PST	PST*[c]	SSE	var. RRKM	Prev. Exp.
57	0.0041 ± 0.0006	0.00066	0.0052	0.0034		
110	0.0082 ± 0.0010	0.0021	0.016	0.0086		
200	0.022 ± 0.004	0.0063	0.048	0.020		
357	0.044 ± 0.008	0.017	0.125	0.041	0.038[d]	0.037±0.010[e]
490	0.070 ± 0.017	0.029	0.208	0.061		

a. Excess Energy is photon energy over threshold for production of CO(v=1) by the singlet channel, 32259.4 cm-1 = 30116.2 + 2143.2 cm-1.

b. Error is 95% confidence interval.

c. PST* uses the PST rate for CO(v=1) and experiment (Ref. 26) for the total rate.

d. From Ref. 20.

e. From Ref. 17, multiplied by singlet yield Ref. 15.

Table IV. Vibrational Branching Ratios for Triplet Product Channel.

hν (cm^{-1})	Energy over triplet threshold (cm^{-1})[a]	$\bar{P}(1\mid t)/\bar{P}(0\mid t)$
32369	4070	0.074 ± 0.016
32459	4160	0.050 ± 0.006
32829	4530	0.044 ± 0.022

a. Energy over triplet threshold is hν-Et, for CO(v=0), where Et is the dissociation threshold for the triplet channel surface, 28299 cm-1, taken from Ref. 7.

b. This is calculated from the triplet vibrational branching ratio and the total triplet rate constant, taken from Ref. 16.

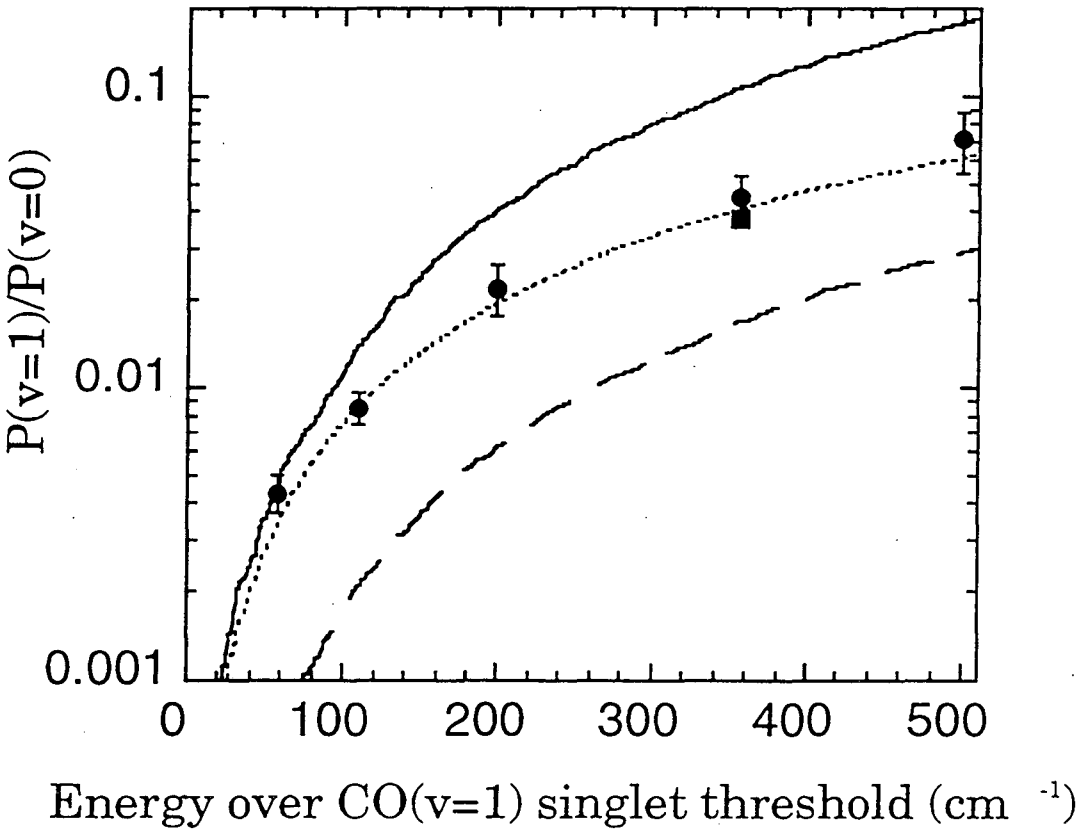

Figure 15. Singlet vibrational branching ratios. The solid circles are the experimental data. The error bars indicate 95% confidence intervals. The solid square is the single available var. RRKM calculation. The dashed line is PST. The solid line combines the PST rate for CO(v=1) with the measured rate for CO(v=0). The dotted line is the SSE prediction, Eq. (4-16).

B. PHOFEX Spectra

The PHOFEX signal, $S(h\nu,v,J_{CO})$ is proportional to the ketene absorption cross section, $\sigma(h\nu)$, the quantum yield, $\Phi(v, J_{CO}, h\nu + E_i)$, for the particular (v, J_{CO}) rovibrational level of CO probed from each particular initial state of ketene, J_i, averaged over the population, $P(T_{beam},J_i)$, of each initial ketene state. $h\nu$ is the photon energy and E_i is the initial thermal energy of ketene in state i at T_{beam}=4 K.

$$S(h\nu, v, J_{CO}) \propto \sigma(h\nu)\sum_i P(T_{beam}, J_i)\Phi(v, J_{CO}, h\nu + E_i) \quad (4\text{-}4)$$

This assumes that $\sigma(h\nu)$, which is a sum over all optically allowed rotational transitions, is not a function of the initial state of ketene. The total quantum yield from each initial state of ketene is the sum of the quantum yields for product from the triplet and singlet channels.

$$\Phi(v, J_{CO}, h\nu + E_i) = \Phi_s(v, J_{CO}, h\nu + E_i) + \Phi_t(v, J_{CO}, h\nu + E_i) \quad (4\text{-}5)$$

Eq. (4-4) can be rewritten as

$$S(h\nu, v, J_{CO}) \propto \sigma(h\nu)[\overline{\Phi}_s(v, J_{CO}, h\nu) + \overline{\Phi}_t(v, J_{CO}, h\nu)], \quad (4\text{-}6)$$

where

$$\overline{\Phi}_s(v, J_{CO}, h\nu) = \sum_i P(T_{beam}, J_i)\Phi_s(v, J_{CO}, h\nu + E_i) \quad (4\text{-}7)$$

and

$$\overline{\Phi}_t(v, J_{CO}, h\nu) = \sum_i P(T_{beam}, J_i)\Phi_t(v, J_{CO}, h\nu + E_i). \quad (4\text{-}8)$$

Two series of PHOFEX spectra are measured on the Q branch, one for $CO(v=1,J_{CO}=3)$ and one for $CO(v=1,J_{CO}=7)$. The PHOFEX curves rise

sharply from the energy threshold for the production of the CO state being probed, then decline at higher energies as other CO rotational states become energetically accessible. As additional $^1CH_2$ states become energetically accessible, in combination with the observed CO state, more product channels open, giving rise to the observed steps in the PHOFEX spectra. These steps match the energies of the $^1CH_2$ term values to within the experimental uncertainty of ± 0.5 cm^{-1}.

In this work, the CO(v=1) product from singlet channel fragmentation is of interest. It is possible that the CO(v=1) product from triplet channel fragmentation has an energy dependence which complicates these spectra. To test for this, $\overline{\Phi}_t(v, J_{CO}, h\nu)$ was calculated at several energies. The singlet and triplet quantum yields may each be written as a series of conditional probabilities[3]

$$\Phi_t(v, J_{CO}, h\nu + E_i) = P_i(t)P_i(v \mid t)P_i(J_{CO} \mid t, v), \qquad (4\text{-}9)$$

where $P_i(t)$ is the triplet yield, $P_i(v \mid t)$ is the fraction of CO formed in vibrational state v along with $^3CH_2$ products, and $P_i(J_{CO} \mid t,v)$ is the rotational distribution for the triplet channel. There is an equivalent formula for the singlet quantum yield. Averaged conditional probabilities may be defined in terms of the measured spectra as follows:

$$\overline{P}(J_{CO} \mid t, v) \equiv \frac{S_t(h\nu, v, J_{CO})}{\sum_{J'CO} S_t(h\nu, v, J'_{CO})} = \frac{\overline{\Phi}_t(v, J_{CO}, h\nu)}{\sum_{J'CO} \overline{\Phi}_t(v, J'_{CO}, h\nu)}, \qquad (4\text{-}10)$$

$$\overline{P}(v \mid t) = \frac{\sum_{J_{CO}} \overline{\Phi}_t(v, J_{CO}, h\nu)}{\sum_{v'} \sum_{J'CO} \overline{\Phi}_t(v', J'_{CO}, h\nu)}, \qquad (4\text{-}11)$$

$$\overline{P}(t) = \frac{\sum_{v',J'_{CO}} \overline{\Phi}_t(v', J'_{CO}, h\nu)}{\sum_{v',J'_{CO}} \overline{\Phi}_t(v', J'_{CO}, h\nu) + \sum_{v',J'_{CO}} \overline{\Phi}_s(v', J'_{CO}, h\nu)}. \qquad (4\text{-}12)$$

Since all excited ketene molecules dissociate,

$$\sum_{v',J'_{CO}} \overline{\Phi}_t(v', J'_{CO}, h\nu) + \sum_{v',J'_{CO}} \overline{\Phi}_s(v', J'_{CO}, h\nu) \equiv 1, \qquad (4\text{-}13)$$

and $\overline{P}(t)$ is (1- $\overline{P}(s)$) from Ref. 16. $\overline{P}(1 \mid t)$ is taken from Table IV, and $\overline{P}(J_{CO} \mid t, v)$ is taken from the rotational distribution of CO observed slightly below the singlet channel threshold from Ref. 17. A triplet yield can be calculated from these experimental probabilities, if the average of products of the conditional probabilities are equal to the product of the averages defined in Eqs. (4-10)-(4-12).

$$\overline{\Phi}_t(v, J_{CO}, h\nu) \approx \overline{P}(t)\overline{P}(v \mid t)\overline{P}(J_{CO} \mid t, v) \qquad (4\text{-}14)$$

Near the threshold for a vibronic channel, its yield increases significantly as individual product rotational channels open and Eq. (4-14) is not valid. However, in the energy region considered here, >100 cm^{-1} over the threshold for singlet channel CO(v=1) and >1900 cm^{-1} over the threshold for triplet channel CO(v=1), such structure in the quantum yields is smaller than the noise levels in the PHOFEX spectra. The estimated values of $\overline{\Phi}_t(v = 1, J_{CO}, h\nu)$ for J_{CO}=3 and J_{CO}=7 are given in Table V, along with $\overline{\Phi}_s(v, J_{CO}, h\nu)$ calculated using Eq. (4-14) with t replaced by s. $\overline{\Phi}_t(v, J_{CO}, h\nu)$ is nearly constant throughout this energy range, and is small compared with $\overline{\Phi}_s(v, J_{CO}, h\nu)$.

The absorption spectrum of jet-cooled ketene has been assumed[7,12,13]

to be independent of the photolysis energy. This assumption was tested by Garcia-Moreno *et al.*,[14] who found the cross section to be constant within 5% for the first 500 cm^{-1} over the singlet channel threshold, and within 10% up to 1000 cm^{-1} over the singlet channel threshold. As this work is at much higher energies, E>2150 cm^{-1} over the singlet channel threshold, this assumption was tested in the same way for the current energy range. From Eqs. (4-6)-(4-13) and their singlet counterparts,

$$\sigma(h\nu) \propto \frac{[S(h\nu, v, J_{CO}) - S_t(h\nu, v, J_{CO})]}{\bar{\Phi}_s(v, J_{CO}, h\nu)} = \frac{S_s(h\nu, v, J_{CO})}{\bar{\Phi}_s(v, J_{CO}, h\nu)} \qquad (4\text{-}15)$$

$\bar{P}(s)$ and $\bar{P}(J_{CO} \mid s,v)$ are taken from Ref. 16 and $\bar{P}(v \mid s)$ is taken from the vibrational branching ratios discussed above. $S_t(h\nu,v=1,J_{CO})$ is set to its value just below the singlet channel threshold for CO(v=1); the difference between the above and below threshold signal, $S_s(h\nu,v=1,J_{CO})$, was measured directly. The results are normalized to the 200 cm^{-1} point for each PHOFEX curve, as shown in Table V. The ratios are generally constant to within ±0.05, except for the lowest energy ratio at 110 cm^{-1} for $CO(v=1,J_{CO}=7)$, which is less than than 0.1 higher. Given the near constancy of $\sigma(h\nu)$, the PHOFEX spectra can be absolutely calibrated as in Ref. 14. The absolute quantum yield of each singlet rotational state is given in Figure 16, using the vibrotational distributions and singlet yield taken from Ref. 16, and the experimental vibrational yield at 200 cm^{-1} over the CO(v=1) singlet channel threshold as the calibration point for each curve.

Table V. Test for Dependence of PHOFEX on Triplet Quantum Yield and Dependence of Optical Cross Section on hν.

Excess Energy (cm^{-1})[a]	Triplet Quantum Yield(%) $CO(v=1,J_{CO}=3)$	$CO(v=1,J_{CO}=7)$
110	0.074 ± 0.017	0.19 ± 0.04
200	0.050 ± 0.011	0.13 ± 0.03
357	0.044 ± 0.023	0.11 ± 0.06
Excess Energy (cm^{-1})[a]	Singlet Quantum Yield (%) $CO(v=1,J_{CO}=3)$	$CO(v=1,J_{CO}=7)$
110	0.14 ± 0.02	0.009 ± 0.002
200	0.29 ± 0.04	0.18 ± 0.03
357	0.40 ± 0.06	0.38 ± 0.06
Excess Energy (cm^{-1})[a]	PHOFEX/Singlet Quantum Yield $CO(v=1,J_{CO}=3)$	$CO(v=1,J_{CO}=7)$
110	1.04	1.08
200	1.00	1.00
357	0.96	0.99

a. As in Table III.

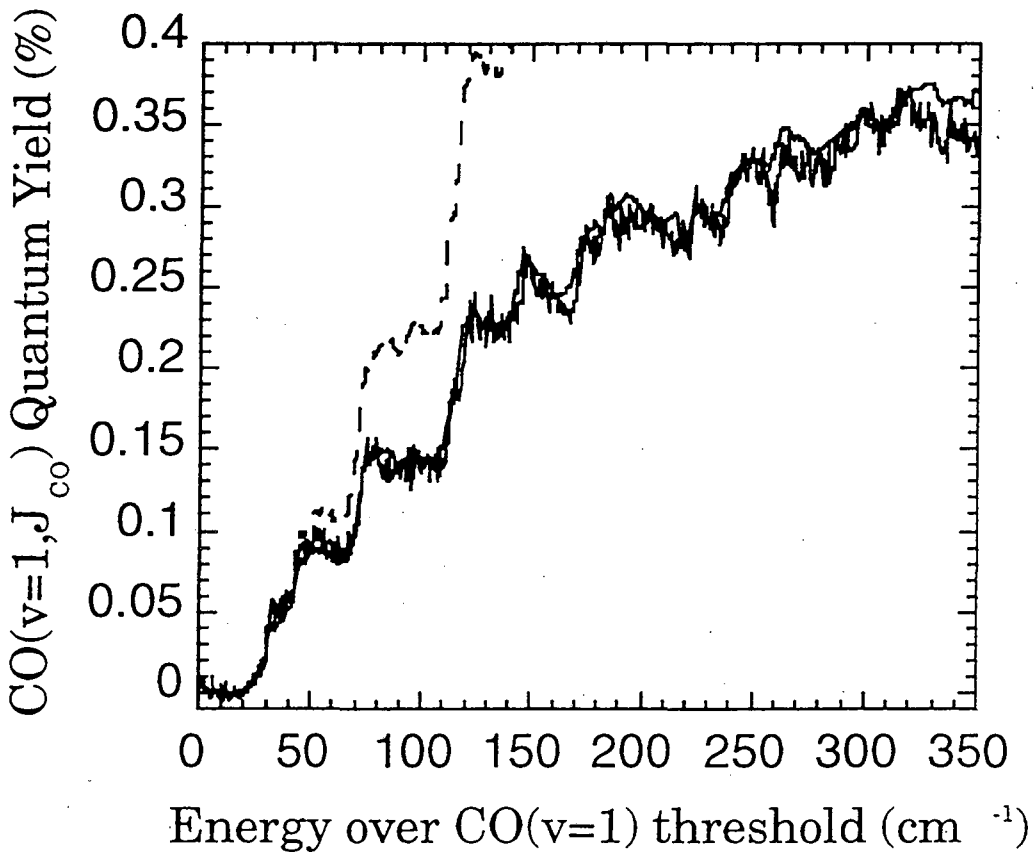

Figure 16a. PHOFEX spectra and PST calculations for CO(v=1,J_{CO}=3). The experimental PHOFEX spectra are placed on an absolute scale using the population distributions at 200 cm^{-1}. The PST curves are on the same absolute scale, showing quantum yield as a percentage of total yield. The solid theoretical line is the yield when $\overline{P}(J_{CO} \mid v,s)$ is given by CPST, and $\overline{P}(v \mid s)$ is given by SSE. The dotted line is the yield when $\overline{P}(J_{CO} \mid v,s)$ is given by PST and $\overline{P}(v \mid s)$ is calculated by assuming that CO(v=1) follows PST while CO(v=0) follows experiment.

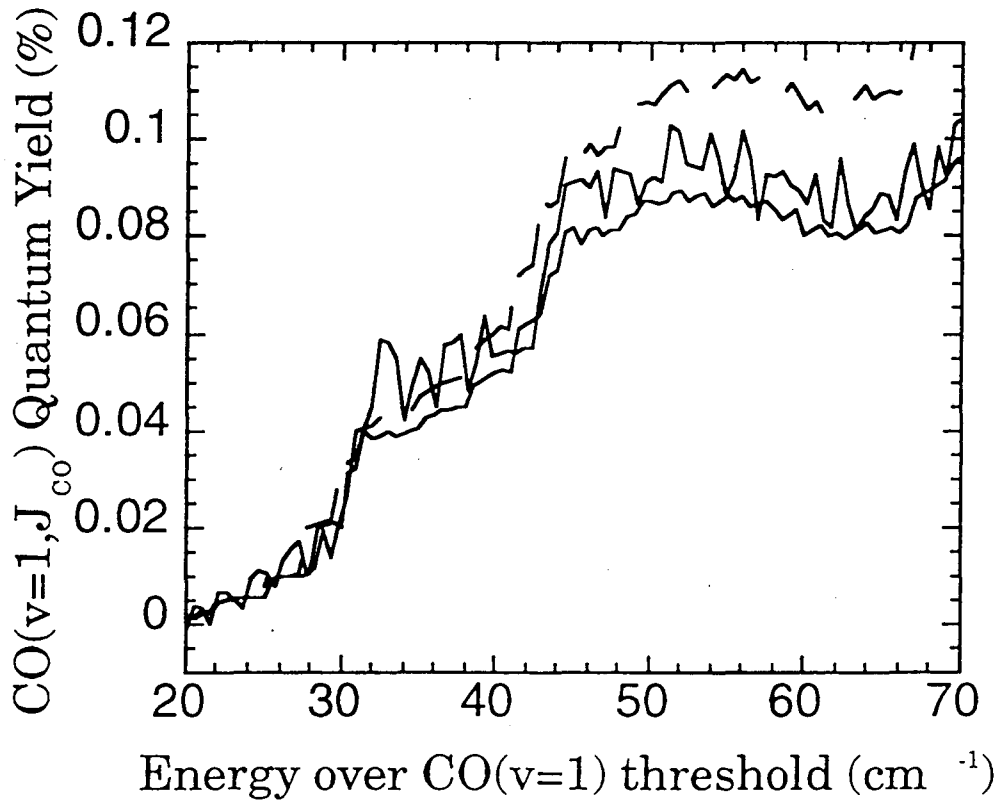

Figure 16b. Expanded view of $CO(v=1,J_{CO}=3)$ PHOFEX Spectra, to show first step more clearly.

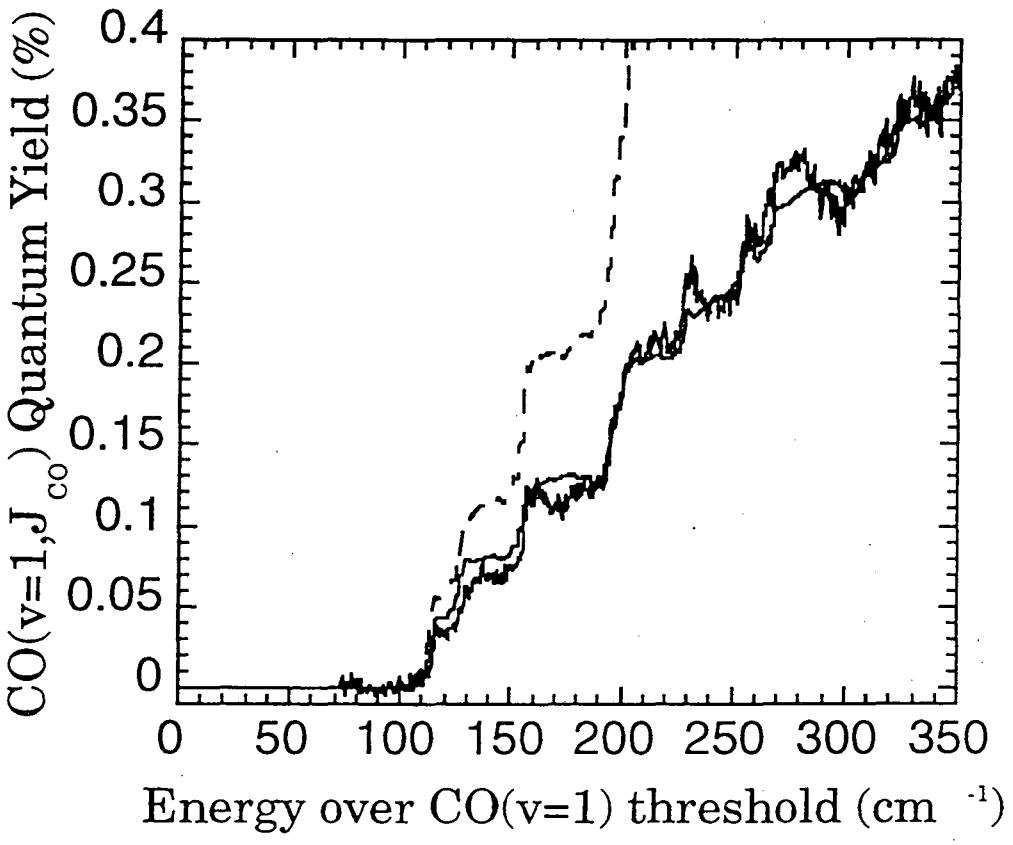

Figure 16c. PHOFEX spectra and PST calculations for CO(v=1,J_{CO}=7).

III. Discussion

A. Singlet Channel Vibrational Branching Ratios

The experimental vibrational branching ratios are compared with the PST, SSE, and var. RRKM models, Table III. PST uses the statistical weights for each set of product excitations at a very loose transition state, with the only restrictions being conservation of energy and total angular momentum. PST strongly underestimates the extent of vibrational excitation. Since PST is known to overestimate the singlet rate constant near 2500 cm^{-1},[17,20] a second approach is used in which the CO(v=1) rate constant is taken from PST while the experimental rate is used for CO(v=0). This model is appropriate for vibrationally adiabatic dynamics with a tightened transition state for the CO(v=0) surface and a completely loose transition state for CO(v=1). PST underestimates the experimental branching ratio at all energies, while this modification of PST overestimates the experimental branching ratio by 25% at 57 cm^{-1}, increasing with energy to a factor of 3 at 490 cm^{-1}.

SSE, developed by Wittig and co-workers,[11] assumes PST-like rotational state distributions within each vibrational state, and assumes that $\overline{P}(v \mid s)$, the probability of forming vibrational state v, is proportional to the density of states of an ensemble of the disappearing oscillators. For ketene, which dissociates to give a diatomic and a polyatomic,

$$\overline{P}(v) = \frac{(E - E_v)^{3/2}}{\sum_{v'} (E - E_{v'})^{3/2}} \qquad (4\text{-}16)$$

where v gives the product vibrational state of interest and v' represents all the possible combinations of product vibrational states for both products,

including $CO(v=0) + {}^1CH_2(0,1,0)$. Although SSE contains no adjustable parameters, it predicts the vibrational distributions of ${}^1CH_2$[15] and the single vibrational branching ratio for CO determined at 357 cm^{-1} by Kim *et. al* [17] as well as did the more complex var. RRKM. SSE describes the vibrational branching ratio for CO(v=1)/CO(v=0) accurately for 110 $cm^{-1} \leq E \leq 490$ cm^{-1}, Table III. At 57 cm^{-1}, it underestimates the branching ratio by ~20%. At 357 cm^{-1}, the only energy at which a var. RRKM branching ratio is available,[20] var. RRKM, SSE, and the experimental vibrational branching ratio compare very well, Table III. SSE generally gives the same vibrational yield as var. RRKM.[3,15,17] These results confirm previous results, and indicate that the dynamics from transition state to fragments are vibrationally adiabatic for the CO stretch.

B. PHOFEX Spectra

The absolute quantum yields of CO(v=1,J_{CO}=3,7) determined from the PHOFEX spectra are compared with two theoretical models in Figure 16. For the dashed line, the yield is calculated using PST for CO(v=1) and experiment for CO(v=0) as in Figure 16 and Table III, and as described in Sec. IV.A. For the solid line, $\overline{P}(v \mid s)$ is assumed to follow SSE, and $\overline{P}(J_{CO} \mid s, v)$ is calculated by PST constrained to the experimental $^1CH_2$ rotational distributions (CPST).[14,16] For E≤200 cm^{-1}, the rotational distribution of $^1CH_2$ is described well by PST,[14] and the calculation is simply PST.

For CO(v=1, J_{CO}=3) and CO(v=1, J_{CO}=7), the agreement between the constrained PST/SSE model and the experiment is very good. For CO(v=1, J_{CO}=3), the model underestimates the yield at low energy, E≤70 cm^{-1}. Since SSE does not deal with the individual rotational channels of the loose transition state, it cannot be accurate at energies for which $\overline{P}(v \mid s)$ exhibits stepwise increases.[15] At higher energies, E≥250 cm^{-1}, the model still gives a yield very close to the experimental yield, but the shape of the model curve begins to deviate from the experimental yield curve. This is to be anticipated since the rotational distributions and yields for $^1CH_2$ deviate from PST for E ≥ 200 cm^{-1}.[14] While CPST predicted the rotational distributions of the CO(v=1) fragments well up to E≤500 cm^{-1},[16] the rotational distributions are not sensitive to the very small deviations detected here.

The PST model for CO(v=1) production gives the energetic position of the steps accurately, but does not describe the amplitude well at all for E ≥ 40 cm^{-1}. This necessarily follows from the overestimate of the $\overline{P}(v = 1 \mid s)$

values in Figure 15 for $E \geq 57$ cm^{-1}. For the CO(v=1, J=3) PHOFEX, this model does predict the first two steps, $E<40$ cm^{-1}, better than the constrained PST/SSE, which suggests that PST is correct for $0 \leq E \leq 40$ cm^{-1}.

C. Singlet Rate Constant

All of the above experimental measurements give product yields rather than rate constants. The quantum yield for any product state is proportional to the rate constant for production of that state:

$$\overline{\Phi}_s(v, J_{CO}, h\nu) = \frac{\overline{k}_s(v, J_{CO}, h\nu)}{\overline{k}_{tot}(h\nu)}, \qquad (4\text{-}17)$$

where $\overline{k}_{tot}(h\nu)$ is given by

$$\overline{k}_{tot}(h\nu) = \sum_i \sum_{J=J_i-1}^{J=J_i+1} P(J, J_i) P(T_{beam}, J_i) k_{tot}(h\nu + E_i, J) \qquad (4\text{-}18)$$

and $P(J,J_i)$ is the normalized oscillator strength of the electronic transition from J_i to J in excited state of ketene.

Potter *et al.* have measured total rate constants for the dissociation of ketene from 450 to 6000 cm^{-1} over the singlet threshold.[26] These are used, along with the previously determined singlet yield,[16] to determine the singlet rate constant for energies between 450 and 6000 cm^{-1}. Rearranging Eq. (4-17), summing over all possible singlet product states, and combining that with the singlet equivalent of Eq. (4-12) gives

$$\overline{k}_s(h\nu) = \overline{P}(s)\overline{k}_{tot}(h\nu), \qquad (4\text{-}19)$$

where $\overline{k}_s(h\nu)$ and $\overline{k}_{tot}(h\nu)$ are the averaged singlet and total rate constants, respectively, and $\overline{P}(s)$ is the singlet yield taken from Ref. (16). These rate constants are given in Table VI.

Below 500 cm^{-1}, there is no measured total rate constant. However, the vibrational branching ratios and singlet rate constants just above the $^1CH_2$ + CO(v=1) threshold can be combined to give a singlet rate constant for

production of CO(v=1), $\bar{k}_s(v=1,h\nu)$. Since the singlet rate constant is only available at a single energy, 2521 cm^{-1}, a linear interpolation of log $\bar{k}_s(h\nu)$ in the energy region 2143-2643 cm^{-1} over threshold is used. The least squares fit gives slope, 3.6577x10-4 1/cm^{-1}, and intercept, 9.007. The interpolated singlet rate constants and the vibrational branching ratios are then used to calculate a singlet rate constant for CO(v=1),

$$\bar{k}_s(v=1,h\nu) = \bar{P}(1\,|\,s)\bar{k}_s(h\nu). \quad (4\text{-}20)$$

In the statistical definition of the rate constant given in Eq. (4-1), the rovibrational density of states, $\rho(h\nu+E_i,J)$, can be written as the product of the vibrational density of states and the rotational degeneracy of the electronically excited ketene

$$\rho(h\nu+E_i,J) = (2J+1)\rho_v(h\nu+E_i). \quad (4\text{-}21)$$

Over the range of energies represented by E_i, $\rho_v(h\nu+E_i)$ is nearly constant, and can be approximated by $\rho_v(h\nu)$. Substituting into Eq. (4-18), then,

$$\bar{k}_{tot}(h\nu) = \frac{\sum_{v',J'_{CO}} \bar{W}(v',J'_{CO},h\nu)}{h\rho_v(h\nu)}, \quad (4\text{-}22)$$

where

$$\bar{W}(v',J'_{CO},h\nu) \equiv \sum_i \sum_{J=J_i-1}^{J=J_i+1} P(J,J_i)P(T_{beam},J_i)\frac{W(v',J'_{CO},h\nu+E_i,J)}{2J+1}. \quad (4\text{-}23)$$

The rate constants for v=1 and v=0 at a given energy above their respective thresholds are expected to differ even though the values of $\bar{W}(v,J_{CO},h\nu)$ are virtually identical. This is because the total rovibrational density of states is a function of the absolute energy. To calculate

$\bar{k}_s(v = 0, h\nu)$, the density of states is assumed to be proportional to the direct count density of states, ρ_{DC}, which is calculated by East *et al.* using a complete *ab initio* anharmonic vibrational analysis of ketene.[28] Based on the measured vibrational branching ratios for CO and $^1CH_2$, Ref. 15 and Sec. IV.A above, there is strong evidence that the dissociation of ketene is vibrationally adiabatic. Given this adiabatic assumption, and because the rotational constant of CO changes very little with v, $W(v,J_{CO},h\nu+E_i)$ is a function of excess energy, so that

$$W(v = 0, J_{CO}, h\nu + E_i) = W\left(v = 1, J_{CO}, h\nu + E_i + 2143.2\ cm^{-1}\right). \tag{4-24}$$

Therefore, using Eq. (4-22),

$$\bar{k}_s(v = 1, h\nu + 2143.2\ cm^{-1}) = \bar{k}_s(v = 0, h\nu)\frac{\rho_{DC}(h\nu)}{\rho_{DC}(h\nu + 2143.2\ cm^{-1})}. \tag{4-25}$$

This direct count gives a vibrational density of states of 18,000 $1/cm^{-1}$ at 30,000 cm^{-1} and 27,700 $1/cm^{-1}$ at 32,000 cm^{-1}, which are basically identical to the Whitten-Rabinovich vibrational density of states, $1.8x10^4$ $1/cm^{-1}$ at 30,000 cm^{-1} and $2.8x10^4$ $1/cm^{-1}$ at 32,000 cm^{-1}.[29] $\bar{k}_s(v = 0, h\nu + 2143.2\ cm^{-1})$ is therefore expected to be 54% larger than $\bar{k}_s(v = 1, h\nu)$, near their respective thresholds. The singlet rate constants, $\bar{k}_s(v = 1, h\nu)$ and $\bar{k}_s(v = 0, h\nu)$, for $E \leq 500\ cm^{-1}$, are given in Table VI. $\bar{k}_s(v = 0, h\nu)$ for $57\ cm^{-1} \leq E \leq 6000\ cm^{-1}$ is shown in Figure 17. Below 500 cm^{-1}, of course, $\bar{k}_s(v = 0, h\nu)$ is identical to $\bar{k}_s(h\nu)$, since no CO(v=1) can be produced. At 490 cm^{-1}, the singlet rate

constant $\bar{k}_s(v = 0, h\nu)$ can be calculated either from the total rate constant and singlet yield[16] or by using the vibrational branching ratio. The two values of log $\bar{k}_s(v = 0, h\nu)$, 8.89(0.07) and 8.98(0.09), agree quite closely and confirm the validity of the assumptions.

At energies below 300 cm^{-1}, the PHOFEX spectra can be used to calculate a continuous rate constant. As in Eqs. (4-19) and (4-20), this rate constant,

$\bar{k}_s(v, J_{CO}, h\nu)$, is proportional to the yield of that state, as defined in Eq. (4-10), and $\bar{k}_s(v = 1, h\nu)$,

$$\bar{k}_s(v = 1, J_{CO}, h\nu) = \bar{k}_s(v = 1, h\nu)\bar{P}(J_{CO} \mid s, v = 1). \qquad (4\text{-}26)$$

Since the PHOFEX signal is proportional to $\bar{\Phi}_s(v = 1, J_{CO}, h\nu)$, see Eq. (4-15) and Sec. III.B, Eqs. (4-17) and (4-26) can be rearranged to give an experimental, continuous form of the effective rate constant, $\bar{k}_s(v = 1, h\nu)$,

$$\bar{k}_s(v = 1, h\nu) = \frac{\bar{\Phi}_s(v = 1, J_{CO}, h\nu)\bar{k}_{tot}(h\nu)}{\bar{P}(J_{CO}|s, v = 1)} \propto \frac{S_s(h\nu, v = 1, J_{CO})\bar{k}_{tot}(h\nu)}{\bar{P}(J_{CO}|s, v = 1)}. \qquad (4\text{-}27)$$

$S_s(h\nu, v=1, J_{CO})$ is measured every 0.5 cm^{-1}. $\bar{P}(J_{CO}|s, v = 1)$ and $\bar{k}_{tot}(h\nu)$, on the other hand, have only been measured at specific energies. In order to obtain continuous values, some assumptions must be made. $\bar{k}_{tot}(h\nu)$ is interpolated from the experimental values, since it is not expected to contain significant structure in this energy region. $\bar{P}(J_{CO}|s, v = 1)$ does contain significant structure. Since much of the observed structure in the PHOFEX spectra reflects the rotational distribution, interpolation is not reasonable. However, the experimentally determined rotational distributions are

described well by PST up to 200 cm^{-1} and by CPST up to 500 cm^{-1} over the singlet channel CO(v=1) threshold.[16] $\overline{P}(J_{CO}|s, v = 1)$ is therefore given by these PST calculations.[16]

Rate constants were calculated from the Q(3) and Q(7) spectra, as well as from a previously reported PHOFEX spectrum for $^1CH_2(0,1,0)1_{01}$.[15] The spectrum for $^1CH_2(0,1,0)1_{01}$ was only used up to 200 cm^{-1}, the highest energy at which the rotational distribution is given accurately by PST. The rate constants calculated from all three PHOFEX spectra were normalized to the experimental rate at 200 cm^{-1}. For $^1CH_2(0,1,0)1_{01}$, there is no vibrational yield available at 200 cm^{-1} over the threshold for production of $^1CH_2(0,1,0)1_{01}$. There is a vibrational yield available 108 cm^{-1} over that production threshold,[15] however, and the resultant rate constant, (log $\overline{k}_S((0,1,0), h\nu) = 7.94$), corrected for the relative density of states, (ρ_{DC}=24,900 $1/cm^{-1}$) as in Eq. (4-25), was compared with the CO(v=1) rate constant at 110 cm^{-1}. The comparable values of log $\overline{k}_S(h\nu)$, 7.92±0.10 for CO(v=1) and 8.09±0.07 for $^1CH_2(0,1,0)$, agree just within experimental error. To avoid steps in the rate constant due solely to averaging the rate constants derived from the PHOFEX curves, all three spectra were normalized to $\overline{k}_S(v = 1, h\nu)$ at 200 cm^{-1}. The results of those calculations were averaged together to give the rate constants shown in Figure 18. The graph does not begin at threshold, since a J_{CO}=0 spectrum could not be measured.

Given experimental values of $\overline{k}_S(v = 1, h\nu)$, a density of states can be derived from Eq. (4-22). When $\overline{W}(v = 1, h\nu)$ is assumed to be given by PST,

the $\rho_v(h\nu)$ derived increases more rapidly than the Whitten-Rabinovich prediction. This is an effect of assuming $\overline{W}(v = 1, h\nu)$ to be PST, since PST overcounts $\overline{W}(v = 1, h\nu)$, which leads to an overestimate of $\rho_v(h\nu)$. At the energy of first two steps for the PHOFEX spectra of $^1CH_2(0,1,0)1_{01}$, 10 cm^{-1}<E<30 cm^{-1} above threshold, $\rho_v(h\nu)$ is constant at (2.52±0.17)x10^4 1/cm^{-1}, 0.91±0.06 times the direct count density of states of 2.77 x10^4 1/cm^{-1}.

However, the $\rho_v(h\nu)$ determined in this work, $\rho_{eff}(h\nu)$, is not the same as the total density of states, $\rho_{tot}(h\nu)$. Since the point group symmetry of ketene is C_{2v}, its rovibrational wavefunctions belong to one of four irreducible representations. Thus only one fourth of the open channels will be available to any one initial dissociative ketene state. Since the *ortho-para* nuclear spin symmetry is conserved and identified in the product states, they are treated separately.[12] The symmetry corresponding to + and - parity in ketene is not resolved in the product studies here, and thus $\overline{W}_{s,n}(h\nu)$ in the PST calculations is summed over two of the four symmetry classes and the density of states thus derived is for the two combined irreducible representations. The total singlet rate constant can be approximated by the weighted sum of the *ortho* and *para* singlet rate constants.[20]

$$\overline{k}_s(h\nu) = (3/4)\overline{k}_{s,ortho}(h\nu) + (1/4)\overline{k}_{s,para}(h\nu) \quad (4\text{-}28)$$

since the statistical weights are 3 to 1, where each $\overline{k}_{s,n}(h\nu)$ is summed over the + and - parity states, as described above.[3]

The *ortho* and *para* rate constants can be defined in terms of Eq. (4-22), where $\rho_n(h\nu)$ is the vibrational density of states for the desired nuclear

spin state, and $\overline{W}_{s,n}(h\nu)$ and $\overline{k}_{s,n}(h\nu)$ are the number of open singlet channels and the singlet rate constant for that nuclear spin state,

$$\overline{k}_{s,n}(h\nu) = \frac{\overline{W}_{s,n}(h\nu)}{h\rho_n(h\nu)} \tag{4-29}$$

Since dissociation occurs >28,000 cm^{-1} above the ground state, the density of states for both *ortho* and *para* are expected to be large and nearly equal. By direct count, at 30,000 cm^{-1} total energy, $\rho_{ortho}(h\nu)$ is 8891.7 $1/cm^{-1}$ and $\rho_{para}(h\nu)$ is 8850.1 $1/cm^{-1}$, while at 33,000 cm^{-1}, $\rho_{ortho}(h\nu)$ is 16,774.5 $1/cm^{-1}$ and $\rho_{para}(h\nu)$ is 16725.4 $1/cm^{-1}$. At the above energies, $\rho_{para}(h\nu)$ is 0.995 and 0.997 of $\rho_{ortho}(h\nu)$, respectively. Within the uncertainty in this experiment, then,

$$\rho_{ortho}(h\nu) = \rho_{para}(h\nu) = \frac{\rho_{tot}(h\nu)}{2} \tag{4-30}$$

so that

$$\overline{k}_{s,n}(h\nu) = \frac{\overline{W}_{s,n}(h\nu)}{h\rho_{tot}(h\nu)/2} \tag{4-31}$$

and the $\rho_{eff}(h\nu)$ calculated above corresponds to $\rho_{tot}(h\nu)/2$, and the value of $\rho_{tot}(h\nu)$ at the CO(v=1) singlet threshold is $(5.04\pm0.33)\times10^4$ $1/cm^{-1}$, 1.82 ± 0.12 times the direct count density of states. $\rho_{DC}(h\nu)$, and $\rho_{tot}(h\nu)$ are shown in Figure 19.

RRKM fits of the rate constant for the dissociation of ketene along the triplet channel determined the density of states for ketene to be $1.11g_t$ times the Whitten-Rabinovich density of states, where g_t is the number of strongly

coupled triplet levels.[30] Since for the singlet level, the density of states is 1.82±0.12 times the direct count density of states, that suggests that g_t is 1.6±0.1.

Using Eq. (4-22) above, and the experimental value for $\rho_{eff}(h\nu)$, a continuous PST rate constant can be calculated. Since the rate constant is a function of energy, and this density of states is calculated at one energy, the density of states is assumed to be proportional to the Whitten-Rabinovich density of states. The PST rate constant is compared with the experimental rate constant for $E \leq 300$ cm^{-1} in Figure 18. Up to 35±5 cm^{-1} over threshold, PST compares extremely well with experiment, including following the two steps at 15 and 21 cm^{-1}. Above 35±5 cm^{-1}, the PST rate constant increases more rapidly than experiment as the transition state tightens.

This continuous rate constant and the rate constants measured at particular energies are compared to PST, SACM[24,25] and three versions of var. RRKM,[20,23] as shown in Figures 17 and 18. For this comparison, the density of states is $\rho_{eff}(h\nu)$, or $\rho_{tot}(h\nu)/2$. The first calculation was performed by Klippenstein and Marcus, based on a model potential, which is identified below as KM var. RRKM.[20] The other two are recent calculations by Klippenstein *et al.*[23] based on a high-level *ab initio* anharmonic vibrational analysis.[28] In KEA1 var. RRKM, W(hν) is the minimum number of available states, at any point along the reaction coordinate. In the KEA2 var. RRKM, two transition states are considered. One is the PST transition state, at large separation, while the other is the inner transition state between 2.2 and 3.1 Å.[23] These two transition states are treated serially, so that for any energy, the effective number of open channels is given by

$$\frac{1}{\overline{W}_{eff}(h\nu)} = \frac{1}{\overline{W}_{PST}(h\nu)} + \frac{1}{\overline{W}_{inner}(h\nu)} \qquad (4\text{-}32)$$

As expected, PST increasingly overestimates the rate as energy increases. The two steps observed in the experimental and PST rate are not predicted by any of the var. RRKM, although since the var. RRKM calculations were performed with resolution of 10 cm^{-1} or worse, they could not be expected to predict the steps. As energy approaches zero, the var. RRKM transition state moves outward until it is identical with the PST transition state, so that, by definition, at E=0, $k_{var.RRKM}(h\nu) = k_{PST}(h\nu)$.

The KM var. RRKM generally predicts the rate less accurately than do the recent *ab initio* based calculations. At high energies, E<2500 cm^{-1}, all three versions of var. RRKM are essentially identical, as shown in Figure 17. The KEA1 var. RRKM predicts a rapid initial rise in the rate, identical to PST up to 170 cm^{-1}, which is shown most clearly in Figure 18b. This is not observed. The KEA2 var. RRKM, underestimates the rate at low energy, E<70 cm^{-1}. At intermediate energies, 70 cm^{-1}<E≤2500 cm^{-1}, KEA2 var. RRKM provides the best estimate of the rates, as shown in Table VI and Figures 17 and 18. From $\overline{W}_{PST}(h\nu)$ and the KEA1 and KEA2 var. RRKM rate constants, $\overline{W}_{eff}(h\nu)$, and $\overline{W}_{inner}(h\nu)$ were calculated, using Eq. (4-22) and the experimentally determined $\rho_{eff}(h\nu)$. For comparison, an experimental value of W, $\overline{W}_{exp}(h\nu)$, was also calculated from the continuous rate constant from threshold to 300 cm^{-1}.

$$\overline{W}_{exp}(h\nu) = \overline{k}_s(h\nu)h\rho_{tot}(h\nu)/2 \qquad (4\text{-}33)$$

These values are shown in Figure 20. This shows clearly that the value of

$\overline{W}_{inner}(h\nu)$ is much larger than $\overline{W}_{exp}(h\nu)$ over this energy region, while $\overline{W}_{eff}(h\nu)$ is within 10% of $\overline{W}_{exp}(h\nu)$. Additionally, an experimental value of $\overline{W}_{inner}(h\nu)$, $\overline{W}_{exp,inner}(h\nu)$, was calculated for 40 cm^{-1} <E< 300 cm^{-1},

$$\frac{1}{\overline{W}_{exp,inner}(h\nu)} = \frac{1}{\overline{W}_{exp}(h\nu)} - \frac{1}{\overline{W}_{PST}(h\nu)} \qquad (4\text{-}34)$$

$\overline{W}_{exp,inner}(h\nu)$ is also shown in Figure 20, and is nearly 40% lower than the value of $\overline{W}_{inner}(h\nu)$ calculated by Klippenstein *et al.*[23] This suggests that the current *ab intitio* calculations still need to be optimized in the low energy region. This is not surprising because, until now, there has been very little experimental data available in this energy region and little attention paid to the potential for R_{CC}>3.1 Å.

SACM rate constants were calculated following Troe[24,25] for a simple Morse attractive potential with a dependence on fragment rotational angle. For this model, the parameter α/β controls the angle dependence of the potential and consequently how rapidly the energy level spacings increase as the chemical bond forms. For α/β=1, SACM and PST are identical; for α/β=0, SACM is equivalent to RRKM for a rigid transition state. Much thermal data for reactions without barriers can be fit with $\alpha/\beta \approx 0.5$.[25] This model does not fit the ketene data near threshold, Fig. 18. If smaller values of α/β are chosen to fit the rate at higher energy, the rate near threshold is calculated to be much smaller than observed. This model potential tightens the transition state much too near to threshold, compared to well above threshold.

All of these results suggest the following. The transition state for the dissociation of ketene is at large separation at low energy, as predicted by

PST. At 35±5 cm^{-1} over threshold, the transition state begins to tighten. This occurs at a significantly lower energy than has been predicted by var. RRKM calculations. KEA1, for example, predicts that the transition state tightens at about 150 cm^{-1}.[23] Additionally, even after the transition state tightens, the large separation transition state appears to have an effect on the dissociation until $\overline{W}_{PST}(h\nu) >> \overline{W}_{inner}(h\nu)$, around 2500 cm^{-1}. Once a molecule has passed through the first transition state, it can remain trapped between the first and the second transition states. This may explain why the rotational distributions are still well described by PST even at energies where the rate constant is much lower than predicted by PST, E≤200 cm^{-1} for $^1CH_2$[14,15] and E≤490 cm^{-1} for CO.[16] At high energies, above 2500 cm^{-1} over threshold, the rate is primarily controlled by the tight transition state, and all three versions of var. RRKM are nearly identical.

Table VI. Rate Constants.

Part I.

Excess Energy[a]	Singlet Yield[c]	$\log \bar{k}_{tot}$[d]	$\log \bar{k}_s(v=1)$[e]
56	0.15 (0.03)	---	7.42 (0.11)
110	0.34 (0.03)	---	7.74 (0.10)
200	---	---	8.21 (0.09)
325	0.63 (0.04)	---	8.55 (0.09)
450[b]	0.71 (0.08)	9.04 (0.03)	8.80 (0.09)
1107	0.80 (0.05)	9.38 (0.07)	---
1435	0.86 (0.02)	9.59 (0.04)	---
1720	0.88 (0.02)	9.70 (0.10)	---
2521	0.92 (0.04)	10.00 (0.10)	---
2942	0.92 (0.04)	10.10 (0.08)	---
3217	0.92 (0.05)	10.17 (0.11)	---
3538	0.93 (0.05)	10.28 (0.04)	---
3763	0.91 (0.06)	10.25 (0.33)	---
4367	0.94 (0.05)	10.54 (0.07)	---
4870	0.94 (0.05)	10.66 (0.36)	---
4920	0.94 (0.05)	10.68 (0.28)	---
5598	0.92 (0.07)	10.75 (0.22)	---

a. As in Table I.

b. At this energy, the singlet yield was calculated at 490 cm^{-1}, while the total rate constant is measured at 450 cm^{-1}.

c. From Ref 16; $\bar{P}(s)$ defined in Eqn. (4-18).

d. The total rate constants are taken from Ref. 26.

Part II.

Excess Energy[a]	log $\bar{k}_s(v=0)$					
	Expt. A[e]	Expt. B[e]	PST[f]	var. RRKM		
				KM[f]	KEA1[g]	KEA2[g]
	---	7.60 (0.11)	7.75	7.71	7.67	7.56
56	---	7.92 (0.10)	8.27	8.03	8.25	8.03
110	---	8.39 (0.09)	8.77	8.37	8.68	8.43
200	---	8.73 (0.09)	9.22	8.63	8.90	8.73
325	8.89 (0.07)	8.98 (0.09)	9.43	8.83	9.04	8.90
450[b]	9.28 (0.06)	---	10.1	9.43	9.47	9.37
1107	9.52 (0.03)	---	10.4	9.63	9.61	9.55
1435	9.64 (0.05)	---	10.5	9.78	9.75	9.70
1720	9.96 (0.06)	---	10.8	10.0	10.02	9.99
2521	10.06 (0.09)	---	10.9	10.1	10.15	10.07
2942	10.13 (0.12)	---	11.0	10.2	10.24	10.21
3217	10.25 (0.07)	---	11.1	10.3	10.32	10.30
3538	10.21 (0.34)	---	11.1	10.4	10.38	10.36
3763	10.51 (0.09)	---	11.3	10.5	10.52	10.50
4367	10.63 (0.37)	---	11.5	10.7	10.63	10.61
4870	10.65 (0.29)	---	11.5	10.7	10.64	10.62
4920	10.71 (0.24)	---	11.7	10.8	10.76	10.75

a. As in Table I.

e. Expt. A is calculated from the singlet yield and the total rate constant at the appropriate energy. log $\bar{k}_s(v=1)$ is calculated from the singlet rate constant and the vibrational branching ratio at the appropriate energy. See text for details.

Expt. B is calculated from log $\bar{k}_s(v=1)$, adjusted for the correct density of states at 30,000 cm^{-1}.

f. From Ref. 20. Using effective density of states and Eq. (4-25).

g. From Ref. 23. Using effective density of states and Eq. (4-25).

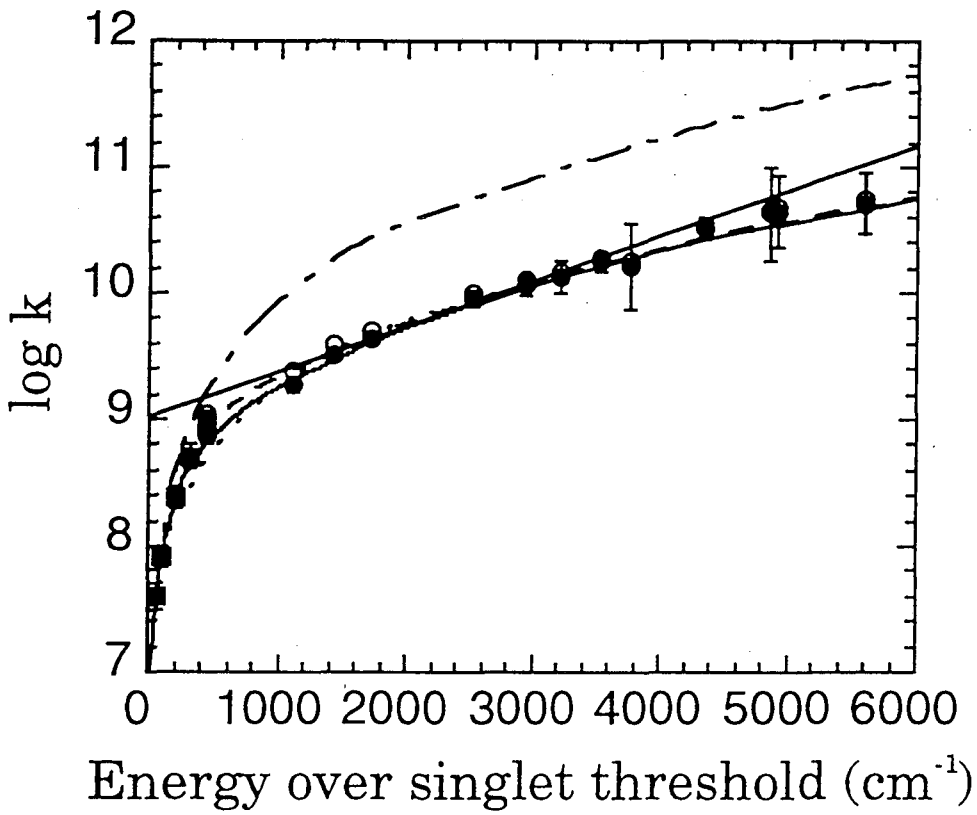

Figure 17. Singlet rate constants. The open circles are the measured total rate constant, singlet plus triplet, Ref. 26. The solid circles are the points for the singlet rate constant calculated from the singlet yield (Ref. 16) and the total rate constant. The solid squares are from the experimental values of the rate constants for CO(v=1) production, the vibrational branching ratio at E, and the direct count density of states near 32,500 and 30,000 cm^{-1}. (See text.) The straight solid line is the linear fit used to approximate $\bar{k}_s(h\nu)$ for use in Eqn. (4-20). The dot-dashed line is the PST rate constant. The dotted line is the KM var. RRKM calculation, Ref. 20, the dashed line and the solid line are the KEA1 and KAE2 var. RRKM calculations, respectively, Ref. 23.

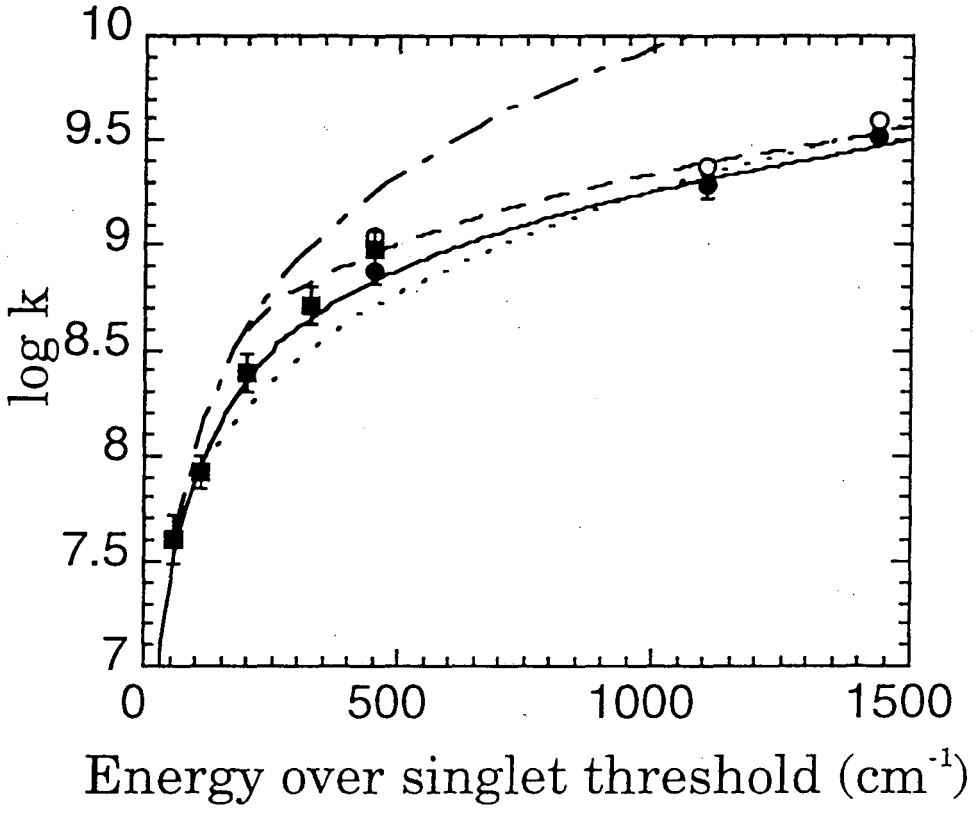

Figure 17b. An expanded view of Figure 17, up to 1500 cm^{-1}.

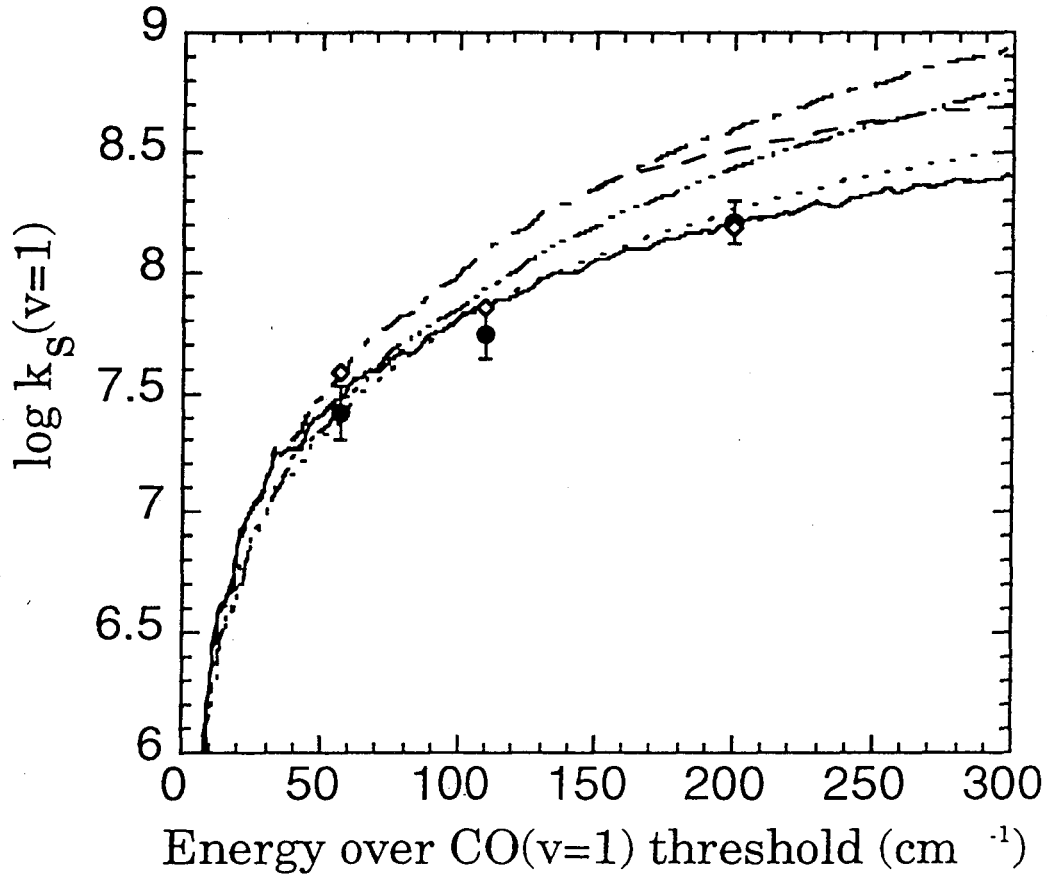

Figure 18. Singlet channel rate constant from PHOFEX data at low energy. The solid line is the continuous experimental rate constant from the PHOFEX data. The solid circles are the experimental rate constants derived from the singlet rate at ~2500 cm^{-1} and the vibrational branching ratios. The dot-dashed line is the PST rate constant. The dot-dot-dashed line is an SACM rate constant, with $\alpha/\beta=0.6$. The open diamonds are the KM var. RRKM, which is only available at two energies in this range. The dashed line is the KEA1 var. RRKM calculation. The dotted line is the KEA2 var. RRKM calculation.

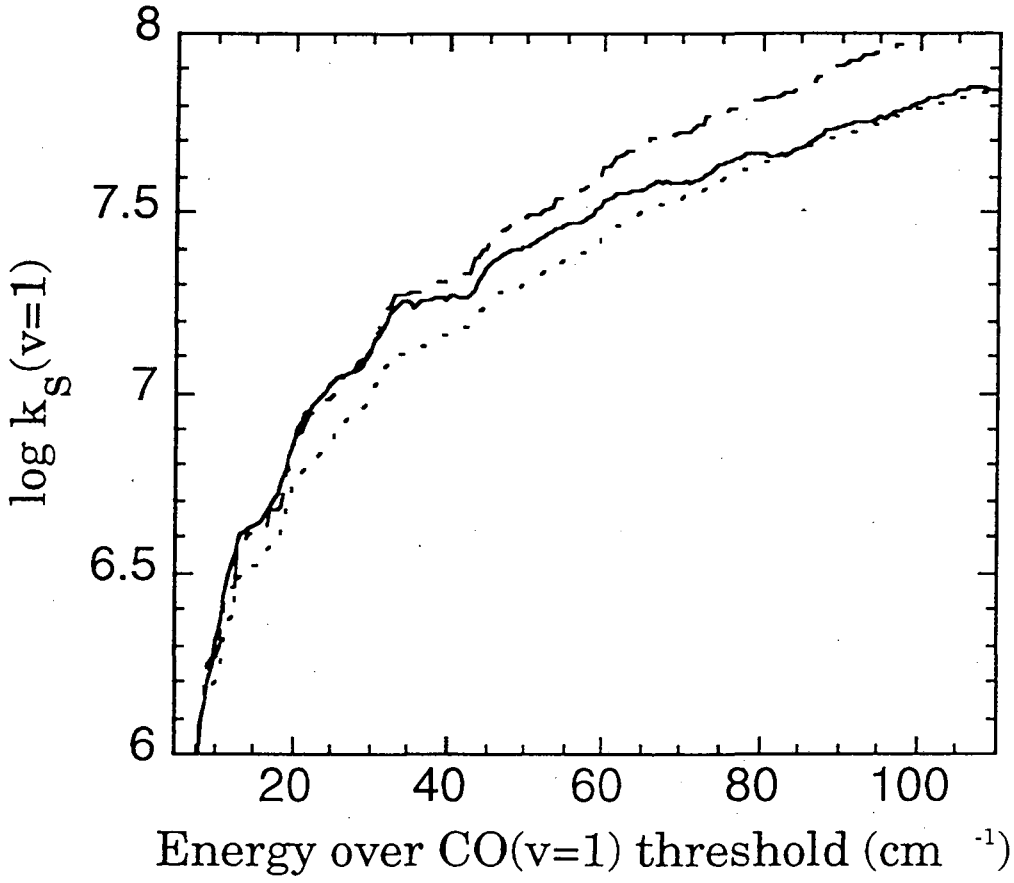

Figure 18b. This expanded view of Figure 18 shows more clearly the region where PST begins to fail. Only PST, KEA2, and the experimental lines are shown.

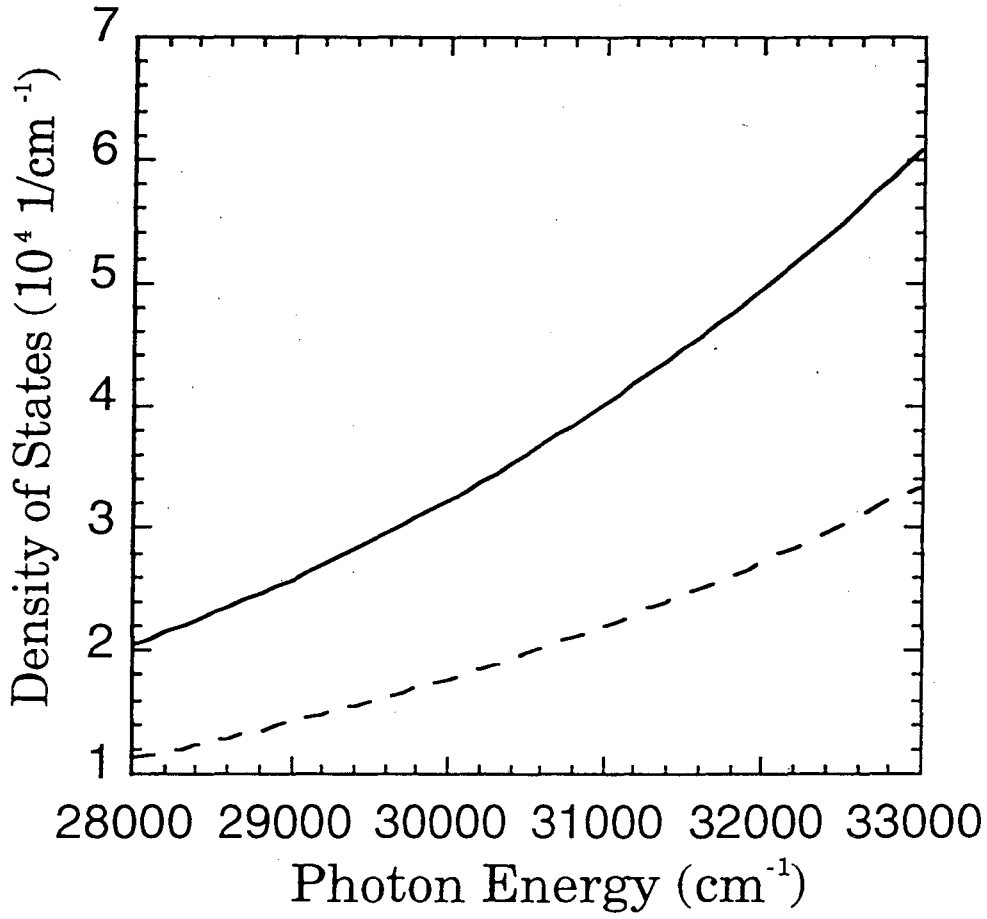

Figure 19. Density of states. The dashed line is the direct count density of states, which is nearly identical to the Whitten-Rabinovich density of states. The solid line is $\rho_{tot}(h\nu)$, which is twice $\rho_{eff}(h\nu)$ determined from the measured rate near threshold.

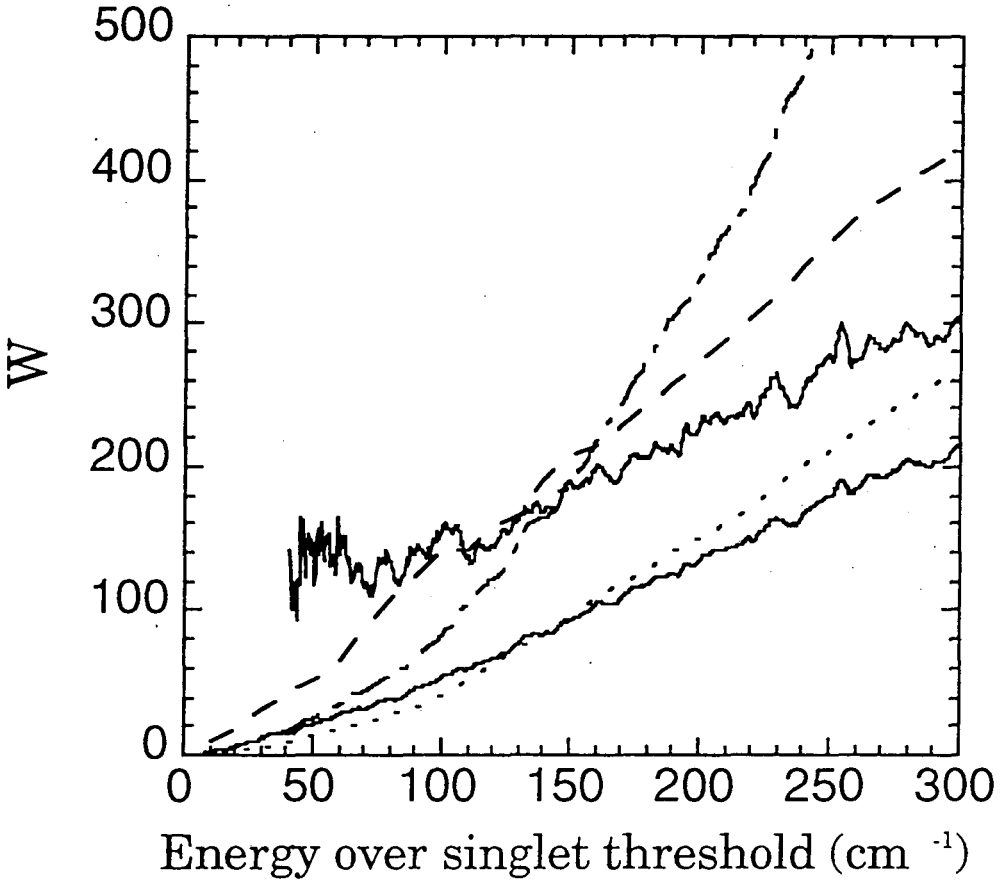

Figure 20. Number of open channels for tight and loose transition states. The dot-dashed line is $\overline{W}_{PST}(h\nu)$, for a loose, PST transition state. The dashed line is $\overline{W}_{inner}(h\nu)$, taken from Ref. 23 for a tight transition state with a CC bond between 2.1-3.1 Å. The dotted line is $\overline{W}_{eff}(h\nu)$, as described in Eq. (4-32) in the text. The lower solid line is $\overline{W}_{exp}(h\nu)$, the experimental number of open channels, and the upper solid line is an experimental value of $\overline{W}_{inner}(h\nu)$, calculated by treating $\overline{W}_{exp}(h\nu)$ as an effective number of open channels.

D. Triplet Vibrational Branching Ratio and Rate Constant

For the triplet channel, unlike the singlet channel, there is no simple theoretical model for calculation of the vibrational branching ratio determined in Sec. III.B and given in Table IV. If the dynamics are assumed to be vibrationally adiabatic, the triplet rate constants determined in Ref. 16 may be used to estimate a branching ratio using Eqs. (4-11), (4-17), and (4-25)

$$\frac{\overline{P}(1\,|\,t)}{\overline{P}(0\,|\,t)} = \frac{\overline{k}_t(h\nu - h\nu_2^{\ddagger})}{\overline{k}_t(h\nu)} \frac{\rho_v(h\nu - h\nu_2^{\ddagger})}{\rho_v(h\nu)}. \qquad (35)$$

Here $\nu_2^{\ddagger}$ is the frequency of the CO stretch at the transition state. This equation is based on the assumption that the triplet channel, like the singlet channel, is vibrationally adiabatic. $\nu_2^{\ddagger}$ is taken from Allen and Schaefer,[31] and is 1878 cm^{-1} for the C_S^I transition state and 1841 cm^{-1} for the C_S^{II} transition state. At energies just over the singlet threshold for production of CO(v=1), the log $\overline{k}_t(h\nu)$ is 8.83±0.10. At 1850 cm^{-1} below that energy, log $\overline{k}_t(h\nu)$ is 8.5±0.1. This gives a predicted value of 0.47±0.09 for $\overline{P}(1\,|\,t)/\overline{P}(0\,|\,t)$, about 8 times larger than the measured value. If $\nu_2^{\ddagger}$ is taken to be 2143.2 cm^{-1}, the vibrational frequency of free CO, log $\overline{k}_t(h\nu)$ is 8.4±0.1, and the predicted vibrational branching ratio is 0.37±0.07. If the triplet channel were vibrationally adiabatic, then the triplet yield of CO(v=1) would have been comparable to, rather than much less than, the singlet yield. These results indicate that CO vibrational excitation relaxes in the exit channel of the triplet PES.

IV. Conclusions

Vibrational branching ratios have been determined experimentally for the dissociation of ketene to $CH_2(\tilde{a}\ ^1A_1)$ + CO(v=1). At energies above 100 cm^{-1}, SSE or var. RRKM provide good predictions of the CO(v=1) yield. This confirms earlier results[15,17] that indicate that product vibrations, unlike product rotations, are adiabatic. PHOFEX spectra have also been measured and compared with theory. These spectra indicate that the rotational distributions for CO(v=1) are described well by CPST up to 350 cm^{-1}, which confirms earlier measurements of CO(v=1) rotational distributions. Additionally, since the production thresholds are observed at the thermodynamic product threshold, these spectra confirm that the dynamics between the transition state and products are not strictly adiabatic.

The rate constants for the production of CO(v=1) and CO(v=0) are derived from the experimental measurements at various energies between 57 and 6000 cm^{-1} above the singlet channel threshold and as a continuous function of energy from near threshold to 300 cm^{-1} above the singlet channel threshold. These experimental values are compared with PST and three var. RRKM calculations that differed in their assumptions about the potential surface. PST was the best model for energies below 35±5 cm^{-1} over threshold. As E increases, var. RRKM becomes the best model for these rates. The transition state begins to tighten at 35±5 cm^{-1} above the singlet channel threshold.

While in general var. RRKM was a better model for E>100 cm^{-1} above the singlet channel threshold, the three versions of var. RRKM varied in their performance. One version is based on a model potential[20] and the other two

are based on a recent high-level *ab initio* potential.[23,28] At intermediate energies, where the three models were most different, the best model was the *ab initio*-based calculations in which both the tight inner transition state and the outer (PST) transition state affect the rate.

While the majority of this work has focused on the singlet channel dissociation, it has also produced some new information on the triplet channel dissociation. Measurement of an experimental rate constant near the singlet channel threshold also allowed for the determination of an experimental density of states, which is found to be 1.82±0.12 times the direct count or the Whitten-Rabinovich density of states, $\rho_{WR}(h\nu)$. Previous work on the triplet channel rate constant had determined the experimental density of states to be $1.11g_t$ times $\rho_{WR}(h\nu)$,[30] which indicates that g_t is 1.6±0.1. Additionally, the measured singlet yields for the ground state and vibrationally excited singlet channel dissociation[16] and the vibrational branching ratio for the singlet channel are used to calculate the vibrational branching ratio for the triplet channel. Unlike the singlet channel, the triplet channel dissociation is not found to be vibrationally adiabatic.

V. References

1. R.G. Gilbert and S.C. Smith, *Theory of Unimolecular and Recombination Reactions* (Blackwell Scientific, Oxford, 1990), and references cited therein.
2. H. Reisler and C. Wittig, Annu. Rev. Phys. Chem. **37**, 307 (1986).
3. W. H. Green, C.B. Moore, and W.F. Polik, Annu. Rev. Phys. Chem. **43**, 591 (1992).
4. C.B. Moore and I.W.M. Smith, J. Phys. Chem. **100** (1996) in press.
5. T. Baer and W.L. Hase, *Unimolecular Reaction Dynamics: Theory and Experiments* (Oxford University Press, Oxford, 1996).
6. P. Pechukas and J.C. Light, J. Chem. Phys. **42**, 3281 (1965); P. Pechukas, C. Rankin, and J.C. Light, J. Chem. Phys. **44**, 794 (1966).
7. I.C. Chen, W.H. Green, and C.B. Moore, J. Chem. Phys. **89**, 314 (1988).
8. J. Miyawaki, K. Yamanouchi, and S. Tsuchiya, Chem. Phys. Lett. **180**, 287 (1991).
9. S.I. Ionov, H.F. Davis, K. Mykhaylichenko, L. Valachovic, R.A. Beaudet, and C. Wittig, *J. Chem. Phys.* **101**, 4809 (1994); B. Abel, H.H. Hamman, and N. Lange, *Faraday Discuss. Chem. Soc.* **102**, (1996); R. Jost, J. Nygard, A. Pasinski, and A. Delon, *J. Chem. Phys.* **105**, 1287 (1996); B. Abel, H.H. Hamann, N. Lange, and J. Troe, *J. Chem. Phys.*, in press.
10. C.X.W. Qian, A. Ogai, H. Reisler, and C. Wittig, J. Chem. Phys. **90**, 209 (1989).
11. C. Wittig, I. Nadler, H. Reisler, J. Catanzarite, and G. Radhakrishnan, J. Chem. Phys. **83**, 5581 (1985).
12. W.H. Green, I. Chia-Chen, and C.B. Moore, Ber. Bunsenges. Phys. Chem. **92**, 389 (1988).
13. W.H. Green, A. H. Mahoney, Q.-K. Zheng, and C.B. Moore, J. Chem.

Phys. **94** 1961 (1991).

14. I. Garcia-Moreno, E.R. Lovejoy, and C.B. Moore, J. Chem. Phys. **100**, 8890 (1994).
15. I. Garcia-Moreno, E.R. Lovejoy, and C.B. Moore, J. Chem. Phys. **100**, 8902 (1994).
16. E.A. Wade, H. Clauberg, S.K. Kim, A. Mellinger, and C.B. Moore, J. Phys. Chem., submitted.
17. S.K. Kim, Y.S. Choi, C.D. Pibel, Q.-K. Zheng, and C.B. Moore, J. Chem. Phys. **94**, 1954 (1991).
18. R.A. Marcus, J. Chem. Phys. **85** 5035 (1986); Chem. Phys. Lett. **144**, 208 (1988); D.M. Wardlaw and R.A. Marcus, Adv. Chem. Phys. **70**, 231 (1988).
19. S.J. Klippenstein, L.R. Khundkar, A.H. Zewail, and R.A. Marcus, *J. Chem. Phys.* **89**, 4761 (1988).
20. S.J. Klippenstein and R.A. Marcus, J. Chem. Phys. **91**, 2280 (1989).
21. S.J. Klippenstein and R.A. Marcus, J. Chem. Phys. **93**, 2418 (1990).
22. J. Yu and S.J. Klippenstein, J. Phys. Chem. **95**, 9882 (1991).
23. S.J. Klippenstein, A.L.L. East, and W.D. Allen, J. Chem. Phys. **105**, 118 (1996); **101**, 9198 (1994).
24. M. Quack and J. Troe, Ber. Bunsenges. Phys. Chem. **78**, 240 (1974); **79**, 170 (1975);**79**, 469 (1975).
25. J. Troe, J. Chem. Phys. **75**, 226 (1981);**79**, 6017 (1983).
26. E.D. Potter, M. Gruebele, L.R. Khundkar, and A.H. Zewail, Chem. Phys. Lett. **164**, 463 (1989).
27. H. Katagiri and S. Kato, J. Chem. Phys. **99**, 8805 (1993).
28. B.-C. Chang, M. Wu, G.E. Hall, and T.J. Sears, J. Chem. Phys. **101**, 9236 (1994).

28. A.L.L. East, W.D. Allen, and S.J. Klippenstein, J. Chem. Phys. **102**, 8506 (1995).

29. K.A. Holbrook, M.J. Pilling, and S.H. Robertson, Unimolecular Reactions, 2nd Ed. (Wiley & Sons, New York, 1996).

30. S.K. Kim, E.R. Lovejoy, and C.B. Moore, J. Chem. Phys., **102**, 3218 (1995).

31. W.D. Allen and H.F. Schaefer, III, J. Chem. Phys. **84**, 2212 (1986).

Appendix A: Rotational Distributions for CO(v=1)
Energies are energies over the CO(v=1) singlet threshold, as in Figure 5

57 cm^{-1}

J_{CO}	Expt.	PST
0		0.07811
1	0.126	0.22469
2	0.145	0.23062
3	0.133	0.24248
4		0.19655
5		0.02751
6	0.035	
7	0.039	
8	0.042	
9	0.045	
11	0.044	
15	0.048	
16	0.052	
17	0.047	
21	0.054	
22	0.044	
23	0.034	
25	0.027	
28	0.018	

110 cm^{-1}

J_{CO}	Expt.	PST
0		0.05293
1	0.0661	0.14902
2		0.21721
3	0.0670	0.17251
4		0.16255
5		0.15162
6	0.0516	0.08392
7	0.0315	0.01025
8	0.0293	
9	0.0331	
10	0.0296	
11	0.0302	
14	0.0311	
15	0.0313	
16	0.0288	
17	0.0243	
21	0.0247	
22	0.0256	
23	0.0135	
24	0.0239	
25	0.0115	
26	0.0175	
27	0.0086	
28	0.0159	

Appendix A: Rotational Distributions for CO(v=1)
Energies are energies over the CO(v=1) singlet threshold, as in Figure 5

200 cm^{-1}

J_{CO}	Expt.	PST
0		0.029988
1	0.0999	0.082661
2	0.1400	0.121770
3	0.1583	0.155760
4	0.1710	0.175210
5	0.1307	0.137830
6	0.1265	0.123110
7	0.0906	0.096636
8	0.0610	0.050236
9	0.0407	0.026435
10		0.000000

357 cm^{-1}

J_{CO}	Expt.	PST	Const. PST
0		0.02000	0.026485
1	0.0522	0.05300	0.057948
2	0.0828	0.09000	0.085059
3	0.1051	0.11000	0.102070
4	0.1110	0.13500	0.099154
5	0.1090	0.13000	0.105670
6	0.1065	0.10500	0.101950
7	0.0975	0.09700	0.097796
8	0.0927	0.09000	0.089955
9	0.0715	0.06700	0.077832
10	0.0591	0.04500	0.065661
11	0.0495	0.03000	0.050451
12	0.0328	0.01500	0.030298
13	0.0130	0.00300	0.009680
14		0.00000	0.000000

Appendix A: Rotational Distributions for CO(v=1)
Energies are energies over the CO(v=1) singlet threshold, as in Figure 5

490 cm^{-1}

J_{CO}	Expt.	PST	Const. PST
0	0.0168	0.014321	0.012839
1	0.0317	0.042219	0.037699
2	0.0593	0.068009	0.060175
3	0.0716	0.086475	0.072139
4	0.0975	0.102670	0.084789
5	0.0955	0.105300	0.092543
6	0.1019	0.107010	0.097267
7	0.0977	0.102990	0.096971
8	0.1009	0.096057	0.093175
9	0.0716	0.074304	0.082386
10	0.0691	0.064478	0.075150
11	0.0668	0.056509	0.069269
12	0.0454	0.036335	0.052106
13	0.0341	0.024840	0.040273
14	0.0232	0.014002	0.024164
15	0.0094	0.004494	0.009063
16		0.000000	0.000000

1107 cm^{-1}

J_{CO}	Expt.	PST	Const. PST
0		0.006933	0.007209
1		0.020600	0.021266
2	0.0210	0.033287	0.032020
3		0.044723	0.041003
4	0.0350	0.055183	0.048622
5	0.0410	0.064729	0.055145
6	0.0470	0.070852	0.059004
7	0.0570	0.071336	0.059693
8	0.0590	0.072338	0.060143
9	0.0550	0.071694	0.060038
10	0.0570	0.067314	0.058709
11	0.0600	0.065439	0.058173
12	0.0550	0.060473	0.056146
13	0.0575	0.055140	0.054321
14	0.0530	0.050927	0.052684
15	0.0530	0.042953	0.049164
16	0.0500	0.039006	0.047176
17	0.0420	0.030651	0.042185
18	0.0395	0.026534	0.039217
19	0.0340	0.020502	0.034162
20	0.0235	0.013916	0.026856
21	0.0180	0.009266	0.020356
22	0.0160	0.004600	0.011853
23	0.0105	0.001603	0.004852
24		0.000000	0.000000

Appendix A: Rotational Distributions for CO(v=1)

Energies are energies over the CO(v=1) singlet threshold, as in Figure 5

1460 cm^{-1}

J_{CO}	Expt.	PST	Const. PST
0		0.005431	0.004386
1	0.0140	0.016014	0.012971
2	0.0215	0.026152	0.021002
3	0.0264	0.035251	0.028203
4		0.043991	0.034373
5	0.0412	0.051754	0.039425
6	0.0434	0.056480	0.043359
7	0.0456	0.060343	0.046267
8	0.0515	0.062105	0.048258
9	0.0535	0.063331	0.049548
10	0.0611	0.062664	0.050374
11	0.0634	0.063412	0.050741
12	0.0608	0.058256	0.050681
13	0.0566	0.055879	0.050757
14	0.0558	0.052520	0.050783
15	0.0532	0.047696	0.049913
16	0.0511	0.042947	0.049347
17	0.0495	0.038026	0.048265
18	0.0427	0.034711	0.047372
19	0.0405	0.029417	0.045556
20	0.0336	0.025989	0.042781
21	0.0309	0.021608	0.038585
22	0.0193	0.016462	0.029340
23	0.0182	0.012868	0.025033
24	0.0133	0.008284	0.018467
25	0.0051	0.005388	0.013867
26	0.0036	0.002551	0.008312
27		0.000471	0.001964

1720 cm^{-1}

J_{CO}	Expt.	PST	Const. PST
0		0.005112	0.007209
1	0.0132	0.015190	0.017820
2	0.0219	0.024690	0.026137
3	0.0241	0.033456	0.034315
4	0.0365	0.041339	0.040789
5	0.0352	0.047585	0.045064
6	0.0412	0.053089	0.048515
7	0.0483	0.055504	0.049732
8	0.0451	0.058829	0.051168
9	0.0505	0.059374	0.050753
10	0.0459	0.058646	0.050081
11	0.0490	0.056741	0.048042
12	0.0608	0.055669	0.045882
13	0.0556	0.052815	0.044423
14	0.0523	0.048819	0.041665
15	0.0450	0.045199	0.040552
16	0.0510	0.044017	0.040232
17	0.0468	0.038670	0.038325
18	0.0415	0.036268	0.037385
19	0.0434	0.031900	0.035475
20	0.0386	0.028459	0.033829
21	0.0352	0.025964	0.032759
22	0.0349	0.021919	0.030125
23	0.0255	0.018155	0.027315
24	0.0260	0.014837	0.024247
25	0.0158	0.011278	0.020732
26	0.0079	0.008156	0.016740
27		0.004955	0.011479
28		0.002716	0.007211
29		0.000647	0.001999

Appendix B: Continuous Rate Constant, log k (k in s^{-1})
Energy is energy over dissociation threshold. Rate is for CO(v=1) + $^1CH_2$.

Energy (cm^{-1})	Expt.	PST	Energy (cm^{-1})	Expt.	PST	Energy (cm^{-1})	Expt.	PST
7.7000	6.0008	6.0190	28.864	7.0799	7.0932	50.166	7.4058	7.4934
8.2000	6.0728	6.0190	29.383	7.0981	7.0932	50.686	7.4127	7.4944
8.7000	6.1389	6.1477	29.905	7.1201	7.1123	51.205	7.4232	7.4947
9.2000	6.1975	6.2424	30.420	7.1453	7.1619	51.727	7.4294	7.4969
9.8000	6.2542	6.2685	30.942	7.1598	7.1678	52.246	7.4342	7.5123
10.300	6.3115	6.2685	31.461	7.1740	7.2074	52.762	7.4405	7.5123
10.800	6.3722	6.3048	31.979	7.1961	7.2374	53.286	7.4482	7.5171
11.300	6.4402	6.4431	32.500	7.2184	7.2374	53.805	7.4541	7.5387
11.800	6.5024	6.4570	33.016	7.2354	7.2689	54.327	7.4574	7.5387
12.400	6.5502	6.4597	33.539	7.2447	7.2693	54.844	7.4624	7.5389
12.900	6.5854	6.5881	34.057	7.2545	7.2710	55.366	7.4702	7.5485
13.400	6.6088	6.5881	34.579	7.2547	7.2739	55.885	7.4711	7.5485
13.900	6.6181	6.5881	35.094	7.2483	7.2756	56.405	7.4688	7.5608
14.400	6.6236	6.6097	35.614	7.2380	7.2756	56.928	7.4749	7.5652
15.000	6.6301	6.6097	36.135	7.2485	7.2789	57.444	7.4810	7.5691
15.500	6.6388	6.6097	36.655	7.2547	7.2854	57.967	7.4871	7.5791
16.000	6.6503	6.6173	37.174	7.2599	7.2874	58.487	7.4940	7.5959
16.500	6.6649	6.6192	37.692	7.2562	7.2906	59.006	7.5086	7.5959
17.000	6.6813	6.6739	38.215	7.2639	7.3002	59.526	7.5196	7.5998
17.446	6.7016	6.6739	38.733	7.2678	7.3106	60.045	7.5309	7.6318
17.965	6.7192	6.6756	39.248	7.2644	7.3106	60.567	7.5367	7.6318
18.487	6.7512	6.6854	39.772	7.2603	7.3106	61.086	7.5428	7.6362
19.004	6.7876	6.7794	40.289	7.2693	7.3118	61.608	7.5534	7.6553
19.520	6.8258	6.7884	40.813	7.2680	7.3186	62.127	7.5578	7.6553
20.041	6.8598	6.8716	41.330	7.2610	7.3330	62.647	7.5560	7.6633
20.559	6.8988	6.8881	41.850	7.2612	7.3333	63.168	7.5577	7.6716
21.080	6.9247	6.8941	42.370	7.2630	7.3333	63.686	7.5610	7.6716
21.596	6.9421	6.9136	42.889	7.2723	7.3333	64.209	7.5590	7.6837
22.114	6.9555	6.9414	43.411	7.2898	7.3745	64.729	7.5634	7.6923
22.635	6.9670	6.9414	43.926	7.3095	7.3759	65.250	7.5699	7.6978
23.155	6.9804	6.9467	44.448	7.3291	7.4014	65.772	7.5796	7.7100
23.672	6.9906	6.9485	44.967	7.3488	7.4014	66.287	7.5871	7.7102
24.192	7.0028	6.9848	45.487	7.3593	7.4241	66.811	7.5883	7.7136
24.713	7.0172	6.9848	46.006	7.3709	7.4270	67.330	7.5859	7.7136
25.231	7.0319	6.9999	46.526	7.3761	7.4526	67.854	7.5902	7.7140
25.750	7.0393	7.0409	47.047	7.3855	7.4529	68.370	7.5871	7.7140
26.268	7.0459	7.0409	47.567	7.3912	7.4565	68.889	7.5820	7.7144
26.788	7.0513	7.0452	48.088	7.3976	7.4619	69.412	7.5825	7.7244
27.309	7.0534	7.0591	48.606	7.3957	7.4675	69.932	7.5871	7.7263
27.827	7.0551	7.0591	49.123	7.4011	7.4675	70.454	7.5883	7.7263
28.346	7.0651	7.0862	49.647	7.4032	7.4742	70.973	7.5858	7.7265

Appendix B: Continuous Rate Constant, log k (k in s^{-1})

Energy is energy over dissociation threshold. Rate is for CO(v=1) + $^1CH_2$.

Energy (cm^{-1})	Expt.	PST	Energy (cm^{-1})	Expt.	PST	Energy (cm^{-1})	Expt.	PST
71.496	7.5911	7.7436	92.850	7.7561	7.9389	114.24	7.8808	8.1314
72.016	7.5948	7.7453	93.371	7.7564	7.9412	114.76	7.8809	8.1315
72.536	7.6017	7.7474	93.895	7.7546	7.9414	115.28	7.8821	8.1369
73.055	7.6067	7.7670	94.416	7.7603	7.9461	115.81	7.8842	8.1372
73.577	7.6170	7.7674	94.936	7.7671	7.9503	116.33	7.8843	8.1455
74.100	7.6230	7.7696	95.457	7.7633	7.9555	116.85	7.8846	8.1458
74.620	7.6352	7.7736	95.979	7.7699	7.9558	117.37	7.8862	8.1475
75.139	7.6394	7.7765	96.502	7.7779	7.9558	117.89	7.8885	8.1567
75.659	7.6418	7.7841	97.024	7.7823	7.9670	118.41	7.8893	8.1586
76.180	7.6452	7.7893	97.543	7.7834	7.9682	118.94	7.8940	8.1617
76.704	7.6519	7.7926	98.065	7.7901	7.9682	119.46	7.8967	8.1621
77.219	7.6514	7.7926	98.588	7.7927	7.9786	119.98	7.8975	8.1621
77.743	7.6557	7.8027	99.110	7.7997	7.9866	120.50	7.8975	8.1651
78.264	7.6638	7.8034	99.627	7.8038	7.9876	121.03	7.9016	8.1679
78.787	7.6682	7.8137	100.15	7.8090	7.9897	121.55	7.9051	8.1679
79.303	7.6677	7.8171	100.67	7.8165	8.0047	122.07	7.9062	8.1698
79.825	7.6674	7.8171	101.20	7.8220	8.0073	122.59	7.9111	8.1737
80.348	7.6658	7.8189	101.71	7.8242	8.0145	123.11	7.9164	8.1758
80.868	7.6616	7.8190	102.24	7.8230	8.0150	123.64	7.9211	8.1805
81.391	7.6594	7.8219	102.76	7.8271	8.0214	124.15	7.9233	8.1823
81.909	7.6582	7.8255	103.28	7.8283	8.0228	124.68	7.9233	8.1826
82.428	7.6620	7.8300	103.81	7.8296	8.0297	125.20	7.9221	8.1895
82.952	7.6615	7.8339	104.32	7.8313	8.0306	125.73	7.9256	8.1956
83.473	7.6632	7.8363	104.85	7.8410	8.0394	126.24	7.9309	8.1995
83.993	7.6712	7.8389	105.37	7.8407	8.0408	126.77	7.9328	8.2060
84.512	7.6770	7.8482	105.89	7.8476	8.0520	127.29	7.9419	8.2180
85.037	7.6794	7.8492	106.41	7.8511	8.0623	127.81	7.9507	8.2193
85.557	7.6869	7.8555	106.93	7.8529	8.0660	128.34	7.9527	8.2229
86.075	7.6964	7.8556	107.46	7.8486	8.0773	128.86	7.9552	8.2322
86.598	7.7012	7.8698	107.98	7.8517	8.0793	129.38	7.9638	8.2373
87.118	7.7108	7.8777	108.50	7.8458	8.0839	129.90	7.9641	8.2466
87.643	7.7209	7.8817	109.02	7.8444	8.0877	130.43	7.9689	8.2507
88.162	7.7293	7.8956	109.54	7.8461	8.0926	130.95	7.9728	8.2507
88.684	7.7331	7.9039	110.06	7.8504	8.0965	131.47	7.9750	8.2580
89.204	7.7353	7.9098	110.58	7.8466	8.1052	131.99	7.9769	8.2604
89.725	7.7383	7.9129	111.11	7.8499	8.1091	132.52	7.9854	8.2652
90.248	7.7422	7.9129	111.63	7.8541	8.1117	133.04	7.9856	8.2742
90.766	7.7456	7.9149	112.15	7.8609	8.1222	133.56	7.9900	8.2753
91.289	7.7489	7.9255	112.67	7.8660	8.1223	134.08	7.9914	8.2827
91.809	7.7517	7.9275	113.19	7.8747	8.1224	134.61	7.9913	8.2827
92.334	7.7522	7.9294	113.72	7.8770	8.1225	135.13	7.9914	8.2827

Appendix B: Continuous Rate Constant, log k (k in s^{-1})

Energy is energy over dissociation threshold. Rate is for CO(v=1) + $^1CH_2$.

Energy (cm^{-1})	Expt.	PST	Energy (cm^{-1})	Expt.	PST	Energy (cm^{-1})	Expt.	PST
135.65	7.9948	8.2830	157.09	8.0718	8.3918	178.56	8.1413	8.5070
136.17	7.9977	8.2847	157.61	8.0732	8.3979	179.09	8.1439	8.5101
136.70	7.9988	8.2856	158.14	8.0769	8.3984	179.61	8.1461	8.5110
137.22	8.0018	8.2874	158.66	8.0822	8.4002	180.13	8.1470	8.5169
137.74	8.0007	8.2874	159.19	8.0866	8.4062	180.66	8.1486	8.5209
138.27	7.9981	8.2883	159.71	8.0892	8.4121	181.18	8.1538	8.5225
138.79	7.9943	8.2884	160.23	8.0957	8.4132	181.71	8.1545	8.5234
139.31	7.9943	8.2900	160.76	8.0989	8.4232	182.23	8.1577	8.5234
139.83	7.9946	8.2908	161.28	8.0997	8.4252	182.76	8.1615	8.5273
140.35	7.9968	8.2920	161.81	8.0994	8.4266	183.28	8.1633	8.5273
140.88	7.9988	8.2920	162.33	8.1003	8.4269	183.81	8.1629	8.5294
141.40	8.0004	8.2920	162.85	8.0982	8.4289	184.33	8.1642	8.5359
141.92	8.0008	8.2962	163.38	8.0968	8.4308	184.85	8.1639	8.5362
142.45	8.0029	8.2985	163.90	8.0961	8.4337	185.38	8.1645	8.5364
142.97	8.0020	8.3016	164.42	8.0977	8.4362	185.90	8.1641	8.5413
143.49	8.0014	8.3018	164.94	8.0982	8.4398	186.43	8.1650	8.5441
144.02	8.0038	8.3090	165.47	8.0968	8.4409	186.95	8.1676	8.5443
144.54	8.0074	8.3118	165.99	8.0971	8.4439	187.47	8.1676	8.5531
145.06	8.0118	8.3184	166.52	8.0966	8.4449	188.00	8.1672	8.5544
145.59	8.0184	8.3253	167.04	8.0953	8.4450	188.52	8.1707	8.5549
146.11	8.0243	8.3355	167.56	8.0941	8.4452	189.05	8.1730	8.5549
146.63	8.0319	8.3360	168.09	8.0963	8.4487	189.57	8.1732	8.5557
147.15	8.0353	8.3363	168.61	8.0981	8.4511	190.10	8.1729	8.5587
147.68	8.0384	8.3376	169.14	8.1021	8.4582	190.62	8.1722	8.5604
148.20	8.0417	8.3383	169.66	8.1066	8.4585	191.14	8.1710	8.5604
148.72	8.0462	8.3419	170.18	8.1113	8.4588	191.67	8.1693	8.5631
149.25	8.0454	8.3442	170.71	8.1147	8.4630	192.19	8.1680	8.5653
149.77	8.0494	8.3445	171.23	8.1187	8.4672	192.72	8.1728	8.5680
150.29	8.0489	8.3460	171.75	8.1220	8.4701	193.24	8.1786	8.5690
150.81	8.0485	8.3536	172.28	8.1235	8.4745	193.77	8.1857	8.5710
151.34	8.0478	8.3564	172.80	8.1275	8.4790	194.29	8.1908	8.5711
151.86	8.0503	8.3580	173.32	8.1313	8.4796	194.82	8.1972	8.5737
152.39	8.0538	8.3650	173.85	8.1350	8.4853	195.34	8.1979	8.5739
152.91	8.0532	8.3691	174.37	8.1360	8.4859	195.86	8.1977	8.5749
153.43	8.0546	8.3720	174.90	8.1379	8.4876	196.39	8.1949	8.5801
153.95	8.0574	8.3725	175.42	8.1388	8.4923	196.92	8.1941	8.5813
154.48	8.0602	8.3745	175.94	8.1400	8.4939	197.44	8.1935	8.5821
155.00	8.0598	8.3760	176.47	8.1380	8.4964	197.96	8.1933	8.5821
155.52	8.0657	8.3809	176.99	8.1395	8.4995	198.49	8.1954	8.5891
156.05	8.0684	8.3824	177.52	8.1417	8.4995	199.01	8.1976	8.5891
156.57	8.0706	8.3842	178.04	8.1429	8.5019	199.54	8.2036	8.5957

Appendix B: Continuous Rate Constant, log k (k in s^{-1})

Energy is energy over dissociation threshold. Rate is for CO(v=1) + $^1CH_2$.

Energy (cm^{-1})	Expt.	PST	Energy (cm^{-1})	Expt.	PST	Energy (cm^{-1})	Expt.	PST
200.07	8.2061	8.5970	221.59	8.2485	8.6805	243.14	8.3077	8.7674
200.59	8.2110	8.6015	222.12	8.2551	8.6835	243.67	8.3096	8.7692
201.11	8.2154	8.6018	222.64	8.2579	8.6865	244.20	8.3103	8.7696
201.64	8.2169	8.6053	223.17	8.2637	8.6872	244.73	8.3132	8.7700
202.16	8.2155	8.6102	223.69	8.2645	8.6899	245.25	8.3156	8.7712
202.69	8.2165	8.6102	224.22	8.2670	8.6905	245.78	8.3180	8.7723
203.21	8.2174	8.6161	224.74	8.2655	8.6917	246.31	8.3186	8.7728
203.74	8.2174	8.6182	225.27	8.2705	8.6932	246.83	8.3199	8.7738
204.26	8.2203	8.6182	225.79	8.2732	8.6959	247.36	8.3200	8.7757
204.78	8.2221	8.6185	226.32	8.2753	8.6986	247.88	8.3247	8.7763
205.31	8.2250	8.6229	226.85	8.2774	8.7049	248.41	8.3254	8.7773
205.84	8.2264	8.6242	227.37	8.2853	8.7058	248.94	8.3273	8.7805
206.36	8.2274	8.6284	227.90	8.2859	8.7059	249.46	8.3290	8.7823
206.89	8.2289	8.6290	228.42	8.2873	8.7135	249.99	8.3293	8.7823
207.41	8.2287	8.6307	228.95	8.2881	8.7144	250.51	8.3285	8.7852
207.94	8.2254	8.6332	229.47	8.2928	8.7187	251.04	8.3270	8.7862
208.46	8.2259	8.6335	230.00	8.2879	8.7220	251.57	8.3272	8.7885
208.99	8.2251	8.6340	230.53	8.2859	8.7229	252.09	8.3320	8.7890
209.51	8.2243	8.6361	231.05	8.2838	8.7242	252.62	8.3403	8.7893
210.04	8.2260	8.6385	231.57	8.2870	8.7275	253.14	8.3436	8.7908
210.56	8.2302	8.6400	232.10	8.2840	8.7298	253.67	8.3488	8.7933
211.09	8.2329	8.6411	232.63	8.2826	8.7338	254.20	8.3552	8.7946
211.61	8.2332	8.6438	233.15	8.2823	8.7347	254.72	8.3557	8.7958
212.14	8.2334	8.6439	233.68	8.2813	8.7364	255.25	8.3538	8.8008
212.66	8.2328	8.6460	234.21	8.2777	8.7373	255.78	8.3481	8.8017
213.19	8.2335	8.6475	234.73	8.2752	8.7387	256.31	8.3466	8.8040
213.71	8.2326	8.6475	235.26	8.2761	8.7389	256.83	8.3405	8.8065
214.24	8.2338	8.6493	235.78	8.2764	8.7405	257.36	8.3342	8.8112
214.76	8.2360	8.6495	236.31	8.2785	8.7421	257.89	8.3310	8.8121
215.29	8.2390	8.6527	236.83	8.2763	8.7445	258.41	8.3363	8.8142
215.81	8.2386	8.6536	237.36	8.2776	8.7457	258.94	8.3348	8.8149
216.34	8.2376	8.6543	237.89	8.2796	8.7464	259.46	8.3364	8.8192
216.86	8.2421	8.6563	238.41	8.2830	8.7529	259.99	8.3400	8.8206
217.39	8.2456	8.6614	238.94	8.2850	8.7535	260.52	8.3418	8.8268
217.91	8.2487	8.6614	239.46	8.2915	8.7568	261.05	8.3423	8.8295
218.44	8.2501	8.6619	239.99	8.2953	8.7569	261.57	8.3440	8.8327
218.97	8.2525	8.6701	240.52	8.2986	8.7602	262.10	8.3464	8.8356
219.49	8.2496	8.6716	241.04	8.3016	8.7615	262.63	8.3494	8.8367
220.02	8.2464	8.6718	241.57	8.3060	8.7622	263.15	8.3526	8.8373
220.54	8.2419	8.6747	242.09	8.3055	8.7654	263.68	8.3540	8.8378
221.06	8.2462	8.6776	242.62	8.3060	8.7670	264.21	8.3611	8.8390

Appendix B: Continuous Rate Constant, log k (k in s^{-1})
Energy is energy over dissociation threshold. Rate is for CO(v=1) + $^1CH_2$.

Energy (cm^{-1})	Expt.	PST	Energy (cm^{-1})	Expt.	PST
264.73	8.3623	8.8398	286.34	8.3802	8.8971
265.26	8.3624	8.8420	286.87	8.3774	8.8991
265.78	8.3616	8.8421	287.40	8.3752	8.9011
266.31	8.3636	8.8447	287.93	8.3754	8.9022
266.84	8.3597	8.8454	288.46	8.3763	8.9029
267.37	8.3605	8.8502	288.98	8.3764	8.9030
267.89	8.3616	8.8511	289.51	8.3779	8.9042
268.42	8.3618	8.8524	290.04	8.3820	8.9056
268.95	8.3594	8.8554	290.56	8.3838	8.9066
269.47	8.3586	8.8555	291.09	8.3842	8.9075
270.00	8.3594	8.8556	291.62	8.3825	8.9085
270.53	8.3590	8.8566	292.15	8.3826	8.9105
271.06	8.3587	8.8591	292.68	8.3829	8.9106
271.58	8.3592	8.8598	293.20	8.3818	8.9121
272.11	8.3612	8.8607	293.73	8.3825	8.9132
272.64	8.3627	8.8609	294.26	8.3863	8.9166
273.16	8.3638	8.8647	294.79	8.3871	8.9167
273.69	8.3679	8.8648	295.31	8.3883	8.9201
274.22	8.3699	8.8691	295.84	8.3925	8.9226
274.74	8.3694	8.8704	296.37	8.3965	8.9263
275.27	8.3687	8.8713	296.90	8.3994	8.9312
275.80	8.3711	8.8740	297.43	8.4010	8.9348
276.33	8.3711	8.8757	297.95	8.4044	8.9355
276.85	8.3735	8.8757	298.48	8.4072	8.9394
277.38	8.3784	8.8797			
277.91	8.3811	8.8813			
278.44	8.3829	8.8823			
278.96	8.3853	8.8825			
279.49	8.3856	8.8854			
280.02	8.3862	8.8861			
280.54	8.3865	8.8883			
281.07	8.3832	8.8890			
281.60	8.3835	8.8895			
282.12	8.3824	8.8896			
282.65	8.3800	8.8900			
283.18	8.3790	8.8903			
283.71	8.3810	8.8915			
284.23	8.3817	8.8926			
284.76	8.3810	8.8927			
285.29	8.3810	8.8930			
285.81	8.3810	8.8950			

Appendix C: Constrained PST Program

```
program countW (input, output);
{This program calculates constrained PST}
{Written by Elisabeth Wade on July 25, 1995}

  type {this is a pascal program, so I set up the arrays in this section}
    EnergiesA = array[0..116, 0..1] of real;
    weights = array[0..116] of real;
    JA = array[0..116, 0..1] of integer;
    UnWeighted = array[0..30] of real;
    Weighted = array[0..30, 0..30] of real;
    Population = array[0..116, 0..40] of real;
    Distribution = array[0..40] of real;
  var
    temperature, a, vpop: real; {temperature is the beam temperature,
                                 a is alpha, which gives the ratio of ortho to para
                                 vpop is the population of the vibrationally excited state of CH2, if any}
                                   {vpop is entered by the user, who should be careful of normalization}
    count: integer;              {count is a dummy variable, for counting population}
    Experimental, ExperimentalV: weights; {These are the experimental populations of CH2, taken from
                                 Garcia-Moreno, Lovejoy, and Moore, JCP, 100 (1994) 8890-8901 and
                                 8902-8906, for CH2(0,0,0) and CH2(0,1,0)
    ErotCH2: EnergiesA;          {an array containing the term values of the 1CH2 states}
    CH2J: JA;                    {an array containing the J value of each possilbe 1CH2 state}
    Ketene: UnWeighted;          {the population of ground state ketene}
    HPop: Weighted;              {the population of excited state ketene before dissociation}
    Distrib: text;               {the output file}
    Energy: real;                {the desired energy over threshold for the calculation}
    Final: Distribution;         {the final distribution of CO(v=1)
    Ws: Population;              {the weights of CO associated with each rovibrational state of 1CH2}

  procedure Initialize (var total, vibration: real);
{This procedure allows the user to enter the energy for the calculation, and the population of the 0,1,0
state}
  begin
    vibration := 0;
    writeln('This program will calculate a CO by PST, then weight it by the experimental distribution
      of CH2');
    writeln('Since our experimental results are only for ortho (i=1), only ortho ketene and CH2
      will be considered');
    writeln;
    writeln('It assumes that alpha is .97 and beam temperature is 3.5 K.');
    writeln('What is the desired energy for this calculation?');
    readln(total);
    if total > 1352.0 then
      begin
        writeln('What is the population of (010) methylene?');
        readln(vibration);
      end;
  end;
```

```
  procedure SetMethylene (var meth: EnergiesA; var methJ: JA);
{This procedure sets up the energies and J states of the available methylene states, up to 2550 cm-1.}
  begin
{The first pair of columns holds values for the para case and the second pair of columns holds values for
the ortho case. The first of the pair gives the term values and the other gives the rotational quantum #}
{Term values were calculated by Inma, taken from her CH2ROT.DAT file}
    meth[0, 0] := 0;        methJ[0, 0] := 0;      meth[0, 1] := 18.269;    methJ[0, 1] := 1;
    meth[1, 0] := 27.173;   methJ[1, 0] := 1;      meth[1, 1] := 31.311;    methJ[1, 1] := 1;
    meth[2, 0] := 53.620;   methJ[2, 0] := 2;      meth[2, 1] := 59.561;    methJ[2, 1] := 2;
    meth[3, 0] := 71.944;   methJ[3, 0] := 2;      meth[3, 1] := 98.535;    methJ[3, 1] := 2;
    meth[4, 0] := 99.645;   methJ[4, 0] := 2;      meth[4, 1] := 104.327;   methJ[4, 1] := 3;
    meth[5, 0] := 107.504;  methJ[5, 0] := 3;      meth[5, 1] := 131.986;   methJ[5, 1] := 3;
    meth[6, 0] := 153.339;  methJ[6, 0] := 3;      meth[6, 1] := 158.357;   methJ[6, 1] := 3;
    meth[7, 0] := 168.963;  methJ[7, 0] := 4;      meth[7, 1] := 170.439;   methJ[7, 1] := 4;
    meth[8, 0] := 208.566;  methJ[8, 0] := 3;      meth[8, 1] := 208.765;   methJ[8, 1] := 3;
    meth[9, 0] := 210.122;  methJ[9, 0] := 4;      meth[9, 1] := 225.398;   methJ[9, 1] := 4;
    meth[10, 0] := 238.732; methJ[10, 0] := 4;     meth[10, 1] := 247.359;  methJ[10, 1] := 5;
    meth[11, 0] := 247.894; methJ[11, 0] := 5;     meth[11, 1] := 283.467;  methJ[11, 1] := 4;
    meth[12, 0] := 284.385; methJ[12, 0] := 4;     meth[12, 1] := 304.424;  methJ[12, 1] := 5;
    meth[13, 0] := 313.959; methJ[13, 0] := 5;     meth[13, 1] := 339.693;  methJ[13, 1] := 5;
    meth[14, 0] := 339.523; methJ[14, 0] := 6;     meth[14, 1] := 339.71;   methJ[14, 1] := 6;
    meth[15, 0] := 355.978; methJ[15, 0] := 4;     meth[15, 1] := 355.999;  methJ[15, 1] := 4;
    meth[16, 0] := 376.812; methJ[16, 0] := 5;     meth[16, 1] := 381.687;  methJ[16, 1] := 5;
    meth[17, 0] := 412.906; methJ[17, 0] := 6;     meth[17, 1] := 418.298;  methJ[17, 1] := 6;
    meth[18, 0] := 445.696; methJ[18, 0] := 7;     meth[18, 1] := 445.611;  methJ[18, 1] := 7;
    meth[19, 0] := 449.610; methJ[19, 0] := 5;     meth[19, 1] := 449.910;  methJ[19, 1] := 5;
    meth[20, 0] := 459.727; methJ[20, 0] := 6;     meth[20, 1] := 488.168;  methJ[20, 1] := 6;
    meth[21, 0] := 499.904; methJ[21, 0] := 6;     meth[21, 1] := 532.55;   methJ[21, 1] := 7;
    meth[22, 0] := 537.645; methJ[22, 0] := 7;     meth[22, 1] := 542.544;  methJ[22, 1] := 5;
    meth[23, 0] := 542.554; methJ[23, 0] := 5;     meth[23, 1] := 564.007;  methJ[23, 1] := 6;
    meth[24, 0] := 565.065; methJ[24, 0] := 6;     meth[24, 1] := 564.019;  methJ[24, 1] := 8;
    meth[25, 0] := 565.537; methJ[25, 0] := 8;     meth[25, 1] := 597.003;  methJ[25, 1] := 7;
    meth[26, 0] := 616.271; methJ[26, 0] := 7;     meth[26, 1] := 640.212;  methJ[26, 1] := 7;
    meth[27, 0] := 655.25;  methJ[27, 0] := 6;     meth[27, 1] := 655.201;  methJ[27, 1] := 6;
    meth[28, 0] := 671.176; methJ[28, 0] := 8;     meth[28, 1] := 671.561;  methJ[28, 1] := 8;
    meth[29, 0] := 694.733; methJ[29, 0] := 7;     meth[29, 1] := 698.7;    methJ[29, 1] := 7;
    meth[30, 0] := 699.434; methJ[30, 0] := 9;     meth[30, 1] := 699.421;  methJ[30, 1] := 9;
    meth[31, 0] := 749.34;  methJ[31, 0] := 8;     meth[31, 1] := 761.139;  methJ[31, 1] := 8;
    meth[32, 0] := 765.379; methJ[32, 0] := 6;     meth[32, 1] := 765.378;  methJ[32, 1] := 6;
    meth[33, 0] := 786.678; methJ[33, 0] := 7;     meth[33, 1] := 786.925;  methJ[33, 1] := 7;
    meth[34, 0] := 800.787; methJ[34, 0] := 8;     meth[34, 1] := 819.038;  methJ[34, 1] := 9;
    meth[35, 0] := 847.184; methJ[35, 0] := 10;    meth[35, 1] := 844.733;  methJ[35, 1] := 8;
    meth[36, 0] := 896.839; methJ[36, 0] := 7;     meth[36, 1] := 847.189;  methJ[36, 1] := 10;
    meth[37, 0] := 914.963; methJ[37, 0] := 9;     meth[37, 1] := 896.846;  methJ[37, 1] := 7;
    meth[38, 0] := 921.487; methJ[38, 0] := 9;     meth[38, 1] := 914.963;  methJ[38, 1] := 9;
    meth[39, 0] := 937.356; methJ[39, 0] := 8;     meth[39, 1] := 937.356;  methJ[39, 1] := 8;
    meth[40, 0] := 938.325; methJ[40, 0] := 8;     meth[40, 1] := 979.634;  methJ[40, 1] := 9;
    meth[41, 0] := 981.295; methJ[41, 0] := 10;    meth[41, 1] := 981.504;  methJ[41, 1] := 10;
    meth[42, 0] := 1012.433;  methJ[42, 0] := 9;   meth[42, 1] := 1024.317; methJ[42, 1] := 7;
    meth[43, 0] := 1024.317;  methJ[43, 0] := 7;   meth[43, 1] := 1032.638; methJ[43, 1] := 9;
    meth[44, 0] := 1047.213;  methJ[44, 0] := 8;   meth[44, 1] := 1047.168; methJ[44, 1] := 8;
    meth[45, 0] := 1174.647;  methJ[45, 0] := 8;   meth[45, 1] := 1174.646; methJ[45, 1] := 8;
```

```
meth[46, 0] := 1318.133;  methJ[46, 0] := 8;   meth[46, 1] := 1318.133;  methJ[46, 1] := 8;
meth[47, 0] := 1106.85;   methJ[47, 0] := 9;   meth[47, 1] := 1109.812;  methJ[47, 1] := 9;
meth[48, 0] := 1216.358;  methJ[48, 0] := 9;   meth[48, 1] := 1216.558;  methJ[48, 1] := 9;
meth[49, 0] := 1343.671;  methJ[49, 0] := 9;   meth[49, 1] := 1343.679;  methJ[49, 1] := 9;
meth[50, 0] := 1487.422;  methJ[50, 0] := 9;   meth[50, 1] := 1487.424;  methJ[50, 1] := 9;
meth[51, 0] := 1646.024;  methJ[51, 0] := 9;   meth[51, 1] := 1646.024;  methJ[51, 1] := 9;
meth[52, 0] := 1093.269;  methJ[52, 0] := 10;  meth[52, 1] := 1096.609;  methJ[52, 1] := 10;
meth[53, 0] := 1174.485;  methJ[53, 0] := 10;  meth[53, 1] := 1196.846;  methJ[53, 1] := 10;
meth[54, 0] := 1231.774;  methJ[54, 0] := 10;  meth[54, 1] := 1294.77;   methJ[54, 1] := 10;
meth[55, 0] := 1302.188;  methJ[55, 0] := 10;  meth[55, 1] := 1404.337;  methJ[55, 1] := 10;
meth[56, 0] := 1405.04;   methJ[56, 0] := 10;  meth[56, 1] := 1531.336;  methJ[56, 1] := 10;
meth[57, 0] := 1531.373;  methJ[57, 0] := 10;  meth[57, 1] := 1675.233;  methJ[57, 1] := 10;
meth[58, 0] := 1675.234;  methJ[58, 0] := 10;  meth[58, 1] := 1834.366;  methJ[58, 1] := 10;
meth[59, 0] := 1834.366;  methJ[59, 0] := 10;  meth[59, 1] := 2007.552;  methJ[59, 1] := 10;
meth[60, 0] := 2007.553;  methJ[60, 0] := 10;  meth[60, 1] := 2007.553;  methJ[60, 1] := 10;
meth[61, 0] := 2536.972;  methJ[61, 0] := 11;  meth[61, 1] := 2536.972;  methJ[61, 1] := 11;
meth[62, 0] := 2310.820;  methJ[62, 0] := 11;  meth[62, 1] := 2310.820;  methJ[62, 1] := 11;
meth[63, 0] := 2106.892;  methJ[63, 0] := 11;  meth[63, 1] := 2106.892;  methJ[63, 1] := 11;
meth[64, 0] := 1925.492;  methJ[64, 0] := 11;  meth[64, 1] := 1925.498;  methJ[64, 1] := 11;
meth[65, 0] := 1767.135;  methJ[65, 0] := 11;  meth[65, 1] := 1767.296;  methJ[65, 1] := 11;
meth[66, 0] := 1632.157;  methJ[66, 0] := 11;  meth[66, 1] := 1634.560;  methJ[66, 1] := 11;
meth[67, 0] := 1517.465;  methJ[67, 0] := 11;  meth[67, 1] := 1535.606;  methJ[67, 1] := 11;
meth[68, 0] := 1411.037;  methJ[68, 0] := 11;  meth[68, 1] := 1469.649;  methJ[68, 1] := 11;
meth[69, 0] := 1296.328;  methJ[69, 0] := 11;  meth[69, 1] := 11399.255; methJ[69, 1] := 11;
meth[70, 0] := 1164.094;  methJ[70, 0] := 11;  meth[70, 1] := 1295.149;  methJ[70, 1] := 11;
meth[71, 0] := 1013.216;  methJ[71, 0] := 11;  meth[71, 1] := 1164.041;  methJ[71, 1] := 11;
meth[72, 0] := 2535.714;  methJ[72, 0] := 12;  meth[72, 1] := 1013.215;  methJ[72, 1] := 11;
meth[73, 0] := 2332.61;   methJ[73, 0] := 12;  meth[73, 1] := 2761.266;  methJ[73, 1] := 12;
meth[74, 0] := 2152.412;  methJ[74, 0] := 12;  meth[74, 1] := 2535.714;  methJ[74, 1] := 12;
meth[75, 0] := 1996.237;  methJ[75, 0] := 12;  meth[75, 1] := 2332.609;  methJ[75, 1] := 12;
meth[76, 0] := 1868.465;  methJ[76, 0] := 12;  meth[76, 1] := 2152.382;  methJ[76, 0] := 12;
meth[77, 0] := 1778.989;  methJ[77, 0] := 12;  meth[77, 1] := 1995.665;  methJ[77, 1] := 12;
meth[78, 0] := 1712.196;  methJ[78, 0] := 12;  meth[78, 1] := 1862.135;  methJ[78, 1] := 12;
meth[79, 0] := 1624.737;  methJ[79, 0] := 12;  meth[79, 1] := 1745.591;  methJ[79, 1] := 12;
meth[80, 0] := 1502.286;  methJ[80, 0] := 12;  meth[80, 1] := 1630.806;  methJ[80, 1] := 12;
meth[81, 0] := 1355.817;  methJ[81, 0] := 12;  meth[81, 1] := 1502.773;  methJ[81, 1] := 12;
meth[82, 0] := 1190.236;  methJ[82, 0] := 12;  meth[82, 1] := 1355.836;  methJ[82, 1] := 12;
meth[83, 0] := 2577.954;  methJ[83, 0] := 13;  meth[83, 1] := 1190.236;  methJ[83, 1] := 12;
meth[84, 0] := 2399.228;  methJ[84, 0] := 13;  meth[84, 1] := 2577.959;  methJ[84, 1] := 13;
meth[85, 0] := 2244.431;  methJ[85, 0] := 13;  meth[85, 1] := 2399.347;  methJ[85, 1] := 13;
meth[86, 0] := 2111.736;  methJ[86, 0] := 13;  meth[86, 1] := 2246.173;  methJ[86, 1] := 13;
meth[87, 0] := 1991.127;  methJ[87, 0] := 13;  meth[87, 1] := 2126.023;  methJ[87, 1] := 13;
meth[88, 0] := 1865.693;  methJ[88, 0] := 13;  meth[88, 1] := 2044.798;  methJ[88, 1] := 13;
meth[89, 0] := 1723.451;  methJ[89, 0] := 13;  meth[89, 1] := 1970.188;  methJ[89, 1] := 13;
meth[90, 0] := 1561.714;  methJ[90, 0] := 13;  meth[90, 1] := 1862.824;  methJ[90, 1] := 13;
meth[91, 0] := 1381.395;  methJ[91, 0] := 13;  meth[91, 1] := 1723.258;  methJ[91, 1] := 13;
meth[92, 0] := 2666.682;  methJ[92, 0] := 14;  meth[92, 1] := 1561.707;  methJ[92, 1] := 13;
meth[93, 0] := 2518.104;  methJ[93, 0] := 14;  meth[93, 1] := 1381.395;  methJ[93, 1] := 13;
meth[94, 0] := 2408.106;  methJ[94, 0] := 14;  meth[94, 1] := 2666.272;  methJ[94, 1] := 14;
meth[95, 0] := 2330.609;  methJ[95, 0] := 14;  meth[95, 1] := 2513.474;  methJ[95, 1] := 14;
meth[96, 0] := 2241.371;  methJ[96, 0] := 14;  meth[96, 1] := 2380.438;  methJ[96, 1] := 14;
meth[97, 0] := 2113.9387; methJ[97, 0] := 14;  meth[97, 1] := 2253.133;  methJ[97, 1] := 14;
```

```
    meth[98, 0] := 1958.212;  methJ[98, 0] := 14;   meth[98, 1] := 2115.211;  methJ[98, 1] := 14;
    meth[99, 0] := 1781.722;  methJ[99, 0] := 14;   meth[99, 1] := 1958.286;  methJ[99, 1] := 14;
    meth[100, 0] := 1586.693; methJ[100, 0] := 14;  meth[100, 1] := 1781.724; methJ[100, 1] := 14;
    meth[101, 0] := 2667.121; methJ[101, 0] := 15;  meth[101, 1] := 1586.693; methJ[101, 1] := 14;
    meth[102, 0] := 2530.763; methJ[102, 0] := 15;  meth[102, 1] := 2714.153; methJ[102, 1] := 15;
    meth[103, 0] := 2379.068; methJ[103, 0] := 15;  meth[103, 1] := 2633.500; methJ[103, 1] := 15;
    meth[104, 0] := 2207.247; methJ[104, 0] := 15;  meth[104, 1] := 2524.755; methJ[104, 1] := 15;
    meth[105, 0] := 2015.868; methJ[105, 0] := 15;  meth[105, 1] := 2378.530; methJ[105, 1] := 15;
    meth[106, 0] := 1806.131; methJ[106, 0] := 15;  meth[106, 1] := 2207.219; methJ[106, 1] := 15;
    meth[107, 0] := 2656.890; methJ[107, 0] := 16;  meth[107, 1] := 2015.867; methJ[107, 1] := 15;
    meth[108, 0] := 2470.314; methJ[108, 0] := 16;  meth[108, 1] := 1806.131; methJ[108, 1] := 15;
    meth[109, 0] := 2264.146; methJ[109, 0] := 16;  meth[109, 1] := 2657.109; methJ[109, 1] := 16;
    meth[110, 0] := 2039.708; methJ[110, 0] := 16;  meth[110, 1] := 2470.325; methJ[110, 1] := 16;
    meth[111, 0] := 2747.520; methJ[111, 0] := 17;  meth[111, 1] := 2264.145; methJ[111, 1] := 16;
    meth[112, 0] := 2526.558; methJ[112, 0] := 17;  meth[112, 1] := 2039.708; methJ[112, 1] := 16;
    meth[113, 0] := 2287.425; methJ[113, 0] := 17;  meth[113, 1] := 2747.517; methJ[113, 1] := 17;
    meth[114, 0] := 2549.281; methJ[114, 0] := 18;  meth[114, 1] := 2526.558; methJ[114, 1] := 17;
    meth[115, 0] := 9999;     methJ[115, 0] := 99;  meth[115, 1] := 2287.425; methJ[115, 1] := 17;
    meth[116, 0] := 9999;     methJ[116, 0] := 99;  meth[116, 1] := 2549.281; methJ[116, 1] := 18;
end; {Set Methylene}

  procedure WeightMethylene (Available: real; CH2: EnergiesA; CH2rot: JA; var Weight000,
    Weight010: weights);
{This procedure assumes that the methylene distributions follow a Boltzman distribution of a temperature
determined by averaging the experimental temperatures for + and - parity. 000 and 010 temp dependances
are determined separately. See Garcia-Moreno, Lovejoy, and Moore, JCP, 100 (1994) 8890-8901 and
8902-8906}
    var
      E010: real;  {This is the energy of the (0,1,0) state, E-1352.5}
      kb: real;      {Boltzmann's constant}
      m: integer;    {a dummy variable}
      T000, T010: real; {The rotational temeperature for both vibrational states of 1CH2}
      sum000, sum010: real;  {The total population of each vibration state, used for normalization}
  begin
    sum000:=0;
    sum010:=0;
    kb := 0.6954;
    for m := 0 to 116 do
      begin
        Weight000[m] := 0;
        Weight010[m] := 0;
      end;
    T000 := 34.2 + (0.2933 * Available); {This relationship isn't good below about 200 cm-1, where}
    for m := 0 to 116 do                 {the experimental 1CH2 distribution is same as PST}
      Weight000[m] := (1 + 2 * CH2rot[m, 1]) * (exp(-CH2[m, 1] / (kb * T000)));
    for m := 0 to 116 do
      sum000 := sum000 + Weight000[m];
    for m := 0 to 116 do
      Weight000[m] := Weight000[m] / sum000;
    E010 := Available - 1352.0;
    if E010 > 0 then
      begin
```

```
        T010 := 40.2 + (0.2764 * E010);
        for m := 0 to 116 do
          Weight010[m] := (1 + 2 * CH2rot[m, 1]) * (exp(-CH2[m, 1] / (kb * T010)));
        for m := 0 to 116 do
          sum010 := sum010 + Weight010[m];
        for m := 0 to 116 do
          Weight010[m] := Weight010[m] / sum010;
      end;
  end;

  procedure Thermal (alpha, Temp: real; var Pop: UnWeighted);
{This calculates the thermal population distribution for ground state ketene}
    var
      I: integer; {nuclear spin, para ->0, ortho ->1: is only 1 here}
      JKet, Ka: integer; {J for symetric top, Ka taken to be 0,1}
      B, A: real; {Rotation constants for symetric top approximated Ketene}
      kbolt: real;{Boltzmann constant in wavenumbers}
      Erot, Evib: real; {Rotational Energy of Ketene}
      sum0, sum1, ratio: real; {Dummy variables to calculate KetPop}
  begin
    B := 0.3370525;
    A := 9.37;
    kbolt := 0.6954;
    sum0 := 0;    sum1 := 0;    ratio := 0;
    I := 1;  {For this program, since Inma only has data for ortho 1CH2, only ortho ketene is considered}
    Ka := 1;

    for JKet := 0 to 30 do
      begin
        Pop[Jket] := 0;
      end;
{This procedure simply calculates the Boltzmann distribution}

    for JKet := 0 to 30 do
      begin
        if (Ka = 1) and (JKet = 0) then
          JKet := JKet + 1;
        Erot := (B * JKet * (JKet + 1)) + (A - B) * Ka * Ka;
        Pop[JKet] := (1 + 2 * JKet) * exp(-Erot / (kbolt * Temp));
        Pop[JKet] := Pop[JKet] * 3 * exp(((A + B) * alpha) / (kbolt * Temp));
        sum1 := sum1 + Pop[JKet];
      end; {of JKet loop}

    for JKet := 0 to 30 do
      begin
        Pop[JKet] := Pop[JKet] / sum1;
      end; {for loop}
  end; {Thermal}

  procedure HonlLondon (input: UnWeighted; var output: Weighted);
{This procedure determines the final population before dissociation by acting on the initial population of
ketene with HL factors. Since the K quantum number of the upper state is not a good quantum number, the
```

```
total transition probability is given by the sum of the two HonlLondon factors for the two transitiitions}
    var
      i, j, ju: integer; {i,j, and ju are indexes.  i stands for the Ka values of ketene, }
            {j is the J states, and ju is for upper J states}
  begin {set output to zero}
{Note:consider only Ka=1 in this case -- ortho only}
    for j := 0 to 30 do
      for ju := 0 to 30 do
        output[ju, j] := 0;{set output to zero}

{Note, for Ka=1 there is no j=0}
    for j := 1 to 30 do
      begin {Determining Honl-London factors for Ka=1}
        if input[j] > 1.0e-5 then
          begin
            output[j + 1, j] := input[j] * (((j + 3) * (j + 2)) + ((j + 1) * j)) / ((j + 1) * (1 + 2 * j));
            output[j, j] := input[j] * ((j * (j + 1)) + ((j + 2) * (j - 1))) / (j * (j + 1));
            output[j - 1, j] := input[j] * (((j - 2) * (j - 1)) + (j * (j + 1))) / (j * (1 + 2 * j));
          end;
      end;{Determining Honl-London factors for Ka=1}
  end; {HonlLondon procedure}

  procedure PST (E, vibpercent: real; Weight: Weighted; ECH2: EnergiesA; JCH2: JA; Pop000,
    Pop010: weights; var out: Distribution);
{This program actually does the PST calculation, weighting the number of states by the population of the
ketene states}
    var
      Etot, Erot, Eexc, ECO: real;  {total energy w/ ketene rotation, ketene rotation, energy available
        for product rotation}
      Evib: real;{energy available for 010 methylene rotation}
      B1, D1: real;{CO rotational constants}
      jl, ju, i: integer;  {j for lower ketene, upper ketene, nuclear rotation}
      jj, l, cn: integer; {total internal rotation, orbital angular momentum, total state count}
      W: real;{total state count with weights}
      sum0, sum1: real;{various sums for averaging}
      JCO, kmeth, p: integer;  {CO rotation, count for methylene, counter}
      Dist000, Dist010: Distribution; {The distributions for 000 and 010, before combination}
      Wvib: Population;{the weights of CO associated with vibrationally excited methylene and
        ground state}
  begin
    for JCO := 0 to 40 do
      begin
        for kmeth := 0 to 116 do
          begin
            Ws[kmeth, JCO] := 0;
            Wvib[kmeth, JCO] := 0;
          end;
      end;
    B1 := 1.905014;     D1 := 5.1043e-6;{This is for CO(v=1)}
    i := 1;
{For ground state methylene}
    for kmeth := 0 to 116 do
```

```
      begin
        writeln('Ground state kmeth is ', kmeth : 4);
        for JCO := 0 to 40 do
          begin
            cn := 0;
            ECO := (B1 * JCO * (JCO + 1)) - (D1 * JCO * JCO * (JCO + 1) * (JCO + 1));
            for jl := 1 to 30 do
              begin
                for ju := 1 to 30 do
                  begin
                    if Weight[ju, jl] <> 0 then
                      begin
                        Erot := 0.3370525 * jl * (jl + 1) + ((9.37 - 0.3370525) * i * i);
                        Etot := Erot + E;
                        Eexc := Etot - ECO;
                        if Eexc >= ECH2[kmeth, i] then
                          begin
                            jj := abs(JCO - JCH2[kmeth, i]);
                            repeat
                              l := abs(ju - jj);
                              repeat
                                cn := cn + 1;
                                l := l + 1;
                              until l > (ju + jj);
                              jj := jj + 1;
                            until jj > (JCO + JCH2[kmeth, i]);
                          end;
                        Ws[kmeth, JCO] := Ws[kmeth, JCO] + cn * Weight[ju, jl];
                      end;
                  end;
              end;
          end;
      end;

{For 010 state methylene}
    Evib := E - 1352.0;
    if Evib > 0 then
      begin
        for kmeth := 0 to 116 do
          begin
            writeln('Vibrationally excited kmeth is ', kmeth : 4);
            for jl := 1 to 30 do
              begin
                for ju := 1 to 30 do
                  begin
                    if Weight[ju, jl] <> 0 then
                      begin
                        Erot := 0.3370525 * jl * (jl + 1) + ((9.37 - 0.3370525) * i * i);
                        Etot := Erot + Evib;
                        for JCO := 0 to 16 do
                          begin
                            cn := 0;
```

```
                                ECO := (B1 * JCO * (JCO + 1)) - (D1 * JCO * JCO * (JCO + 1)
                                  * (JCO + 1));
                                Eexc := Etot - ECO;
                                if Eexc >= ECH2[kmeth, i] then
                                  begin
                                    jj := abs(JCO - JCH2[kmeth, i]);
                                    repeat
                                      l := abs(ju - jj);
                                      repeat
                                        cn := cn + 1;
                                        l := l + 1;
                                      until l > (ju + jj);
                                      jj := jj + 1;
                                    until jj > (JCO + JCH2[kmeth, i]);
                                  end;
                                Wvib[kmeth, JCO] := Wvib[kmeth, JCO] + cn * Weight[ju, jl];
                              end;
                          end;
                      end;
                  end;
              end;
          end;

{normalize so that each methylene column sums to one}
      for kmeth := 0 to 116 do
        begin
          sum0 := 0; sum1 := 0;
          for p := 0 to 40 do
            begin
              sum0 := sum0 + Ws[kmeth, p];
              sum1 := sum1 + Wvib[kmeth, p];
            end;
          if sum0 > 0 then
            for p := 0 to 40 do
              Ws[kmeth, p] := Ws[kmeth, p] / sum0;
          if sum1 > 0 then
            begin
              for p := 0 to 40 do
                Wvib[kmeth, p] := Wvib[kmeth, p] / sum1;
            end;
        end;

{Weight each methylene channel by its experimental weight}
      for kmeth := 0 to 116 do
        begin
          for p := 0 to 40 do
            begin
              Ws[kmeth, p] := Ws[kmeth, p] * Pop000[kmeth];
              Wvib[kmeth, p] := Wvib[kmeth, p] * Pop010[kmeth];
            end;
        end;
{Combine methylene columns to give two distributions for v=0 and v=1}
```

```
    for p := 0 to 40 do
      begin
        Dist000[p] := 0;
        Dist010[p] := 0;
      end;
    for p := 0 to 40 do
      begin
        for kmeth := 0 to 116 do
          begin
            Dist000[p] := Dist000[p] + Ws[kmeth, p];
            Dist010[p] := Dist010[p] + Wvib[kmeth, p];
          end;
      end;
{Normalize distributions, then combine using vibpercent to give ratio}
    sum0 := 0; sum1 := 0;
    for p := 0 to 40 do
      begin
        sum0 := sum0 + Dist000[p];
        sum1 := sum1 + Dist010[p];
      end;
    if sum0 > 0 then
      for p := 0 to 40 do
        Dist000[p] := Dist000[p] / sum0;
    if sum1 > 0 then
      begin
        for p := 0 to 40 do
          Dist010[p] := Dist010[p] / sum1;
      end;
    for p := 0 to 40 do
      out[p] := (1 - vibpercent) * Dist000[p] + (vibpercent * Dist010[p]);
{Write output}
    rewrite(Distrib, 'Constrained Output');
    writeln(Distrib, 'This is the result for a Constrained PST distribution of CO.');
    writeln(Distrib, 'It is calculated ', E : 4 : 0, ' cm-1 over threshold.');
    if vibpercent > 0 then
      writeln(Distrib, vibpercent, ' is found in the vibrationally excited methylene
      state.');
    writeln;
    writeln(Distrib, 'JCO  Population');
    for p := 0 to 40 do
      writeln(Distrib, p : 4, '', out[p] : 10 : 8);
  end;{PST}

begin{main}
  vpop := 0; a := 0.97; temperature := 3.5
  Initialize(Energy, vpop);
  SetMethylene(ErotCH2, CH2J);
  WeightMethylene(Energy, ErotCH2, CH2J, Experimental, ExperimentalV);
  Thermal(a, temperature, Ketene);
  HonlLondon(Ketene, HPop);
  PST(Energy, vpop, HPop, ErotCH2, CH2J, Experimental, ExperimentalV, Final);
end.{main}
```

ERNEST ORLANDO LAWRENCE BERKELEY NATIONAL LABORATORY
ONE CYCLOTRON ROAD | BERKELEY, CALIFORNIA 94720

Prepared for the U.S. Department of Energy under Contract No. DE-AC03-76SF00098

AAE474
LBL Libraries